sciendo

Ceylon cinnamon and clove essential oils as promising free radical scavengers for skin care products

Silvia Martiniaková, Aneta Ácsová, Jarmila Hojerová, Zuzana Krepsová, František Kreps

Faculty of Chemical and Food Technology STU, Radlinského 9, 812 37 Bratislava, Slovak Republic
silvia.martiniakova@stuba.sk, jarmila.hojerova@stuba.sk

Abstract: Due to adverse effects of free radicals on human skin and increasing consumer demand for natural ingredients, essential oils from basil, Ceylon cinnamon bark, clove, juniper, lavender, oregano, rosemary, tea tree, thyme, and ylang-ylang were assessed for their antiradical activity. The oils were evaluated in the concentration range of 5—0.1 mg · mL^{-1}, in which the three reference synthetic antioxidants are most often added to mass-produced cosmetics. Among all examined samples, C. cinnamon oil at a concentration of 5 mg · mL^{-1} showed the strongest DPPH radical scavenging activity (0.41 mg · mL^{-1} IC50), followed by clove oil, BHA, α-tocopherol, and BHT (0.82, 0.84, 0.88 and 0.93 mg · mL^{-1} IC50), respectively. At the same concentration, the reduction power of C. cinnamon oil was higher (1.64 mg · mL^{-1} Trolox Eq.) than that of α-tocopherol and BHT (1.42 and 0.80 mmol · L^{-1} Trolox Eq., respectively) but lower than that of BHA (1.81 mmol · L^{-1} Trolox Eq.). Antiradical activity of the other eight essential oils was low or negligible. C. cinnamon oil and clove oil are promising antiradical agents for skin care but according to our GC-MS analysis, these oils contain 0.29 % of cinnamaldehyde, 0.03 % of linalool, 0.02 % of D-limonene, and 0.02 % of eugenol or 0.41 % of eugenol and 0.002 % of linalool, respectively, which are monitored contact allergens in cosmetics. Such a product is not be suitable for consumers allergic to these substances but for the vast majority of consumers it does not pose a risk in terms of allergic manifestations.

Key words: *Cinnamonum zeylanicum* bark oil, *Eugenia caryophyllus* oil, free radical scavengers, skin care products

Abbreviations: BHA: butylated hydroxyanisole; BHT: butylated hydroxytoluene; C. cinnamon: Ceylon cinnamon; DPPH: 1,1-Diphenyl-2-picrylhydrazyl; EC: European Commission; EO/EOs: Essential oil/ Essential oils; FRAP: Ferric reducing antioxidant power; GC-MS: Gas chromatography-Mass spectrometry; IC50: Median Inhibition Concentration; INCI: International Nomenclature of Cosmetic Ingredients; RSA: Radical scavenging activity; SCCS: Scientific Committee on Consumer Safety; TPTZ: 2,4,6-Tris(2-pyridyl)-*s*-triazine; Trolox: 6-Hydroxy-2,5,7,8-tetramethylchromane-2-carboxylic acid.

Introduction

Finding substances that are not only effective against excess free radicals but are acceptable to both — the environment and the demanding consumer, is one of the challenges in human health care. Free radicals are highly reactive and unstable compounds which, together with oxidants, can be both harmful and useful to the human body. They are endogenously produced as part of normal mitochondrial metabolism. At moderate or low levels, free radicals have beneficial effects and are involved in various physiological functions such as immune function (i.e. defense against pathogenic microorganisms), a number of cellular signaling pathways, mitogenic response and in redox regulation (Phaniendra et al., 2015; Marchi et al., 2022). However, at higher concentration, reactive free radicals can attack biomolecules (DNA, proteins, and lipids) and are also associated with various diseases such as cancer and atherosclerosis as well as degenerative processes of the central nervous system such as Alzheimer's disease and aging progression (Labat-Robert and Robert, 2014; Phaniendra et al. 2015; Marchi et al. 2022). In addition to endogenous sources, more and more free radicals come from exogenous sources (excessive exposure to UVA rays and other radiation, air pollution, cigarette smoke, etc.). The imbalance between production and accumulation of free radicals causes oxidative stress in human body, including the skin (Poljšak and Dahmane, 2012; Pizzino et al., 2017; Sudarikov et al., 2021). To either prevent these reactive species from formation or remove them before they can damage vital components of the skin cells, synthetic antioxidants such as α-tocopherol, butylated hydroxyanisole (BHA) and butylated hydroxytoluene (BHT) are commonly incorporated into skin care products (Hatwalne, 2012; Ácsová et al., 2021).

However, BHA and BHT are under investigation due to concerns regarding their side effects, e.g. endocrine disruption, and their toxicity to aquatic life and high bioaccumulation potential. While BHA use in cosmetics is gradually limited, BHT is still present in various product categories (Wang et al., 2017; Yang et al., 2018; Ribeiro et al., 2019;

Hojerová and Martiniaková, 2021). For this reason and the increasingly consumer interested in natural substances in skin care products, extensive investigation of natural sources of efficient radical scavenging compounds in health research has received high attention.

Essential oils (EOs) derived from medicinal plants are a complex of volatile substances as by-products of plant metabolism providing the plant with a characteristic odour. Chemical composition and the corresponding bioactive properties of EOs are influenced by many factors, such as species, vegetation stage at the time of harvest, geographical origin — cultivar, as well as climatic conditions of cultivation, method of isolation, part of the plant from which it was isolated, etc. In addition to the characteristic aroma, many EOs have antibacterial, antifungal, anti-inflammatory and insecticidal effects (Arantes et al., 2019; Behbahani et al., 2020; Abelan et al., 2021). At present, the antioxidant capacity of EOs is of great interest in the food and cosmetics industry (Ribeiro et al., 2019; Tepe and Ozaslan, 2020).

With regard to possible use in skin protection products, ten natural essential oils have been evaluated for their ability to scavenge free radicals and reduce metal ions compared to three synthetic antioxidants (BHT, BHA and α-tocopherol) commonly added to mass-produced cosmetics (Hojerová and Martiniaková, 2021).

Material and methods

Essential oils

Ten plant EOs (Tab. 1), antioxidant activity of which is currently discussed in literature (Olszowy1 and Dawidowicz, 2016; Wang et al., 2017; Mahomoodally et al., 2018; Behbahani et al., 2020), were selected for the study. All ten EOs were supplied by Calendula Inc. (Nová Ľubovňa, Slovak Republic) and used without any purification. Eight of these EOs were produced directly by Calendula company, while tea tree oil and ylang-ylang oil by Misitano & Stracuzzi SpA (Messina, Italy), all by steam distillation from parts of the plant or the whole plant as shown in Tab. 1.

Chemicals

Three synthetic antioxidants (α-tocopherol, purity ≥ 95.5 %, butylated hydroxyanisole, BHA ≥ 99 %, and butylated hydroxytoluene, BHT ≥ 99 %) supplied by Sigma-Aldrich (Darmstadt, Germany) were used as the reference compounds. 2,2-Diphenyl-1-picrylhydrazyl (‘DPPH ≥ 99 %), 6-Hydroxy-2,5,7,8-tetramethylchromane-2-carboxylic acid (Trolox 97 %), and 2,4,6-Tris(2-pyridyl)-*s*-triazine

Tab. 1. Evaluated plant essential oils.

Essential oil	International Nomenclature of Cosmetic Ingredients name	Volatile oil from	CAS number
Basil	*Ocimum Basilicum Oil*	basil leaves	84775-71-3
Ceylon cinnamon bark	*Cinnamomum Zeylanicum Bark Oil*	inner bark of Ceylon cinnamon	84649-98-9
Clove	*Eugenia Caryophyllus Bud Oil*	dried flower buds of clove	84961-50-2
Juniper	*Juniperus Communis Wood Oil*	wood and twigs of juniper	84603-69-0
Lavender	*Lavandula Angustifolia Flower Oil*	lavandula flowers	8000-28-0
Oregano	*Origanum Vulgare Oil*	whole plant of wild marjoram	84012-24-8
Rosemary	*Rosmarinus Officinalis Leaf Oil*	flowering tops and leaves of rosemary	84604-14-8
Tea Tree	*Melaleuca Alternifolia Leaf Oil*	tea tree leaves	85085-48-9
Thyme	*Thymus Vulgaris Oil*	whole plant of thyme	84837-14-9
Ylang-ylang	*Cananga Odorata Flower Oil*	cananga flowers	83863-30-3

(TPTZ ≥ 98 %) were also obtained from Sigma-Aldrich (Darmstadt, Germany). UV-grade ethanol and UV-grade methanol were purchased from Fisher Slovakia (Bratislava, Slovak Republic), ferric chloride, acetic acid glacial, and sodium acetate from Centralchem (Bratislava, Slovak Republic).

Methods

Antiradical activity of samples was estimated by two electron transfer assays (DPPH and FRAP) using an Epoch Microplate Reader (BioTek Instruments, Winooski, USA) in 96-well ELISA plates (Biotech, Bratislava, Slovak Republic). All tested contained 5 $mg \cdot mL^{-1}$ of the respective compound, also concentration range of 5 to 0.1 $mg \cdot mL^{-1}$ was tested as it is the common concentration range of the three synthetic antioxidants (α-tocopherol, BHA and BHT) selected as references (positive controls) in this study in cosmetic products (Fiume et al. 2018; CIR 2019; L'Oréal 2020; Hojerová and Martiniaková 2021). Each test was done in five replicates.

Free radical (DPPH•) scavenging assay

The DPPH free radical scavenging activity (RSA) assay is based on the measurement of the ability of an antioxidant substance to scavenge radical diphenylpicrylhydrazyl and to reduce it to diphenylpicrylhydrazine with simultaneous colour change from purple to yellow measured spectrophotometrically. The method described by Brand-Williams et al. (1995) was used in this study. Briefly, EO (0.5 mL at 5 $mg \cdot mL^{-1}$ in ethanol) was added to 2 mL of 0.07 $mmol \cdot L^{-1}$ methanolic DPPH. After a 60 min incubation at ambient temperature in the dark, the absorbance of the mixture at 518 nm against methanol as a blank was read. Free radical (DPPH•) scavenging activity was expressed as percentage effect and calculated using the following equation (1):

$$RSA\ (\%) = \frac{(A_{control} - A_{sample})}{A_{control}} \times 100 \qquad (1)$$

where $A_{control}$ and A_{sample} are the absorbance values of a mixture of ethanol + methanolic DPPH and a mixture of sample + ethanol + methanolic DPPH, respectively. IC50 value, the concentration of sample exhibiting 50 % free radicals scavenging activity, was also determined by non-linear regression analysis using the GraphPad Prism® version 7 software.

Then, for the three EOs (C. cinnamon, clove and thyme) with the highest RSA values, kinetic profiles of RSA were determined at reaction times of 0, 10, 20, 30, 40, 50, and 60 min and concentrations of 5, 2, 1, 0.5, 0.25, and 0.1 $mg \cdot mL^{-1}$.

Ferric reducing power assay

The ferric reducing antioxidant power (FRAP) assay uses antioxidants as reductants in a redox-linked colorimetric reaction, where Ferric (Fe^{3+}) to ferrous (Fe^{2+}) ion reduction at low pH causes the formation of a coloured ferrous-probe complex from a colourless ferric-probe complex. Such colour change is measured spectrophotometrically. The reducing power of all samples in this study was determined according to the procedure of Benzie and Strain (1996) with slight modifications. In the FRAP assay, EO (20 µL at 5 and 2 $mg \cdot mL^{-1}$ in ethanol) in a well of a 96-well plate was mixed with 180 µL of the FRAP reagent (25 mL of 300 $mmol \cdot L^{-1}$ acetate buffer at pH 3.6, 2.5 mL of 10 $mmol \cdot L^{-1}$ 2,4,6-tri(2-pyridyl)-1,3,5-triazine in 40 $mmol \cdot L^{-1}$ HCl (TPTZ solution) and 2.5 mL of 20 $mmol \cdot L^{-1}$ $FeCl_3.6H_2O$). After incubation for 30 min in the dark and at 37 °C, absorbance of the mixture at 593 nm against a blank (freshly prepared FRAP reagent without the sample) was read. Absorbance data of the samples were compared with the Trolox standard data from the calibration curves and then expressed as $mmol \cdot L^{-1}$ Trolox Equivalent (Trolox Eq.).

Gas chromatography-mass spectrometry assay

Major constituents of four EOs were analysed using an Agilent 7890 A gas chromatograph (GC) connected with an Agilent 5975C mass selective (MS) detector (Agilent Technologies, Santa Clara, CA, USA). Chromatographic separations were performed on a HP-5 ms capillary column (30 m × 0.25 mm; 0.25 µm film thickness; Agilent Technologies). Solution of EO (1 µL in hexane) was injected into the inlet (280 °C) operating in split mode 1 : 10. The GC was operated at a helium flow rate of 2 ml min^{-1} (pressure of 220 kPa) and programmed with an initial oven temperature of 80 °C (2 min hold), which was then increased from 10 °C min^{-1} up to 300 °C (8 min hold). The MS detector parameters were as follows: transfer line temperature of 250 °C, MS source temperature of 230 °C, quadrupole temperature of 150 °C, filament ionisation energy of 70 eV and *m/z* range of 28—600. Recording and evaluation of data was performed using the ChemStation software E 02/01/1177. Product identification was carried out by comparing mass spectra with a commercial database NIST (the National Institute of Standards and Technology), and Wiley Mass Spectral Library. Each sample was measured in triplicate.

Statistical analysis

Results were expressed as mean values ± standard deviation (SD), unless stated otherwise. Statistical comparison between sample means was determined by one-way analysis of variance (ANOVA) followed

by Bonferroni's test for comparison of EO with the reference of α-tocopherol. Differences were considered significant at $p < 0.05$(*) and $p < 0.01$(**).

Results and discussion

There are many different terms (antiradical activity, antioxidant activity, antioxidant capacity, antioxidant power, antioxidant ability) and numerous methods to assess the mechanisms of action of antioxidant compounds. However, none of these terms or of these, mostly non-specific, methods describe "total antioxidant activity" or cover all aspects of the antioxidant properties of a particular sample. The total antioxidant activity must reflect the capacity of both the lipophilic and the hydrophilic components and, at least for physiologically active compounds, hydrogen atoms transfer (radical quenching) and electron transfer (radical reduction) must be considered and distinguished (Alam et al., 2013; Ortuño et al., 2016; Brainina et al., 2019; Coy-Barrera, 2020; Echegaray et al., 2021).

Given the intended use of EOs in cosmetic products to protect human skin from free radicals generated in the external environment, the aim of this study was to determine their antiradical activity as one of the most important aspects of antioxidant activity.

DPPH radical scavenging activity of essential oils

A number of methods to evaluate the radical scavenging efficiency of antioxidants have been developed. The DPPH and ABTS methods are routinely used for this purpose as standard colorimetric methods easy to perform The DPPH assay was chosen in this study because the DPPH radical is more stable than the ABTS (2,2´-azino-bis (3-ethylbenzthiazoline-6-sulphonic acid) one. DPPH radical is stable since it is a nitrogen centred free radical that can accept an electron or hydrogen radical to become a stable diamagnetic molecule (Gulcin et al., 2012; Olszowy and Dawidowicz, 2016; Akar et al., 2017; Gotmare, 2018). According to Chen et al. (2013), the DPPH method is the most widespread test of antiradical activity of plant extracts.

Radical scavenging potential of the samples was determined by measuring the degree of discolouration of DPPH solution. Results for ten EOs and three synthetic antioxidants at 5 $mg \cdot mL^{-1}$ after 60 min of incubation are given in Fig. 1. C. cinnamon essential oil demonstrated the strongest DPPH radical inhibitory activity of all examined samples, reaching up to 81 % RSA and 0.41 $mg \cdot mL^{-1}$ IC50. The second and third most effective EOs were clove oil and thyme oil (63 % RSA, 0.82 $mg \cdot mL^{-1}$ IC50 and 57 % RSA, 0.99 $mg \cdot mL^{-1}$ IC50), respectively, with RSA and IC50 values comparable to those of BHA, α-tocopherol, and BHT (73, 62, and 61 % RSA and 0.85, 0.88, and 0.93 $mg \cdot mL^{-1}$ IC50), respectively. Ylang-ylang oil (55 % RSA, 1.03 $mg \cdot mL^{-1}$ IC50) showed moderate DPPH radical scavenging activity. RSA values for tea tree, oregano, lavender, juniper, basil and rosemary oil were lower or much lower

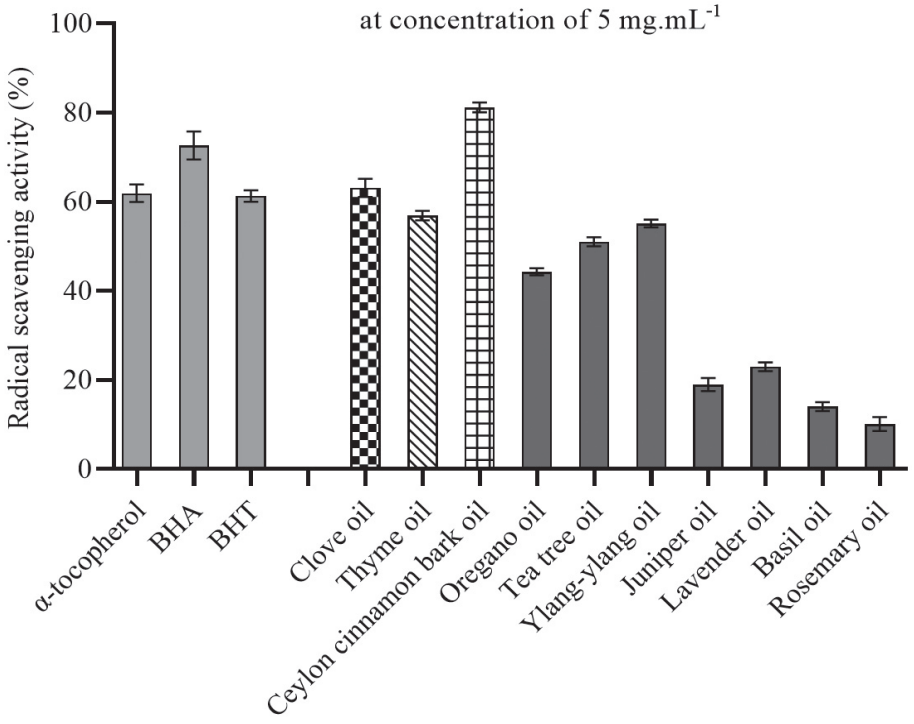

Fig. 1. DPPH free radical scavenging activity of ten EOs, α-tocopherol, BHA and BHT at 5 $mg \cdot mL^{-1}$ and 60 min. Data are given as the mean ± standard deviation (n = 5).

(51, 44, 19, 23, 14 and 10 %) than those of the three synthetic antioxidants. IC50 values for these EOs could not be calculated. In summary, the inhibition of DPPH radicals by EOs decreased in the order of C. cinnamon > clove > thyme > ylang-ylang > > tea tree > oregano > lavender > juniper > basil > > rosemary.

Kinetic profiles in the reaction time of 0, 10, 20, 30, 40, 50 and 60 min at six concentrations from 5 to 0.1 mg · mL^{-1} of C. cinnamon, clove and thyme, three EOs which proved to be the most effective of the evaluated ten oils in terms of RSA are illustrated in Fig. 2a–2c. For all three EOs, the most significant uptake of DPPH radicals was recorded during the first ten minutes of incubation at most concentrations evaluated. RSA values of C. cinnamon oil (Fig. 2a) at ≥ 2 mg · mL^{-1} began to stagnate after 20 min, which can be considered as the time when •DPPH was almost completely oxidised. Thyme oil showed increasing DPPH radical scavenging activity with increasing concentration throughout the incubation time (Fig. 2c) without stabilisation. In contrast, the kinetic dependence of clove oil (Fig. 2b) showed that with the increasing incubation time, the DPPH radical scavenging activity decreased, especially at the concentration ≥ 1 mg · mL^{-1}. Which might be due to the loss of the relationship between the degree of radical inhibition and the colour change of the evaluated solution at such high clove oil concentrations.

Free radical scavenging activity (expressed as inhibition percentage of DPPH radicals) of the three most effective EOs in the concentration range of 5–0.1 mg · mL^{-1} after 60 min of incubation compared to BHA, α-tocopherol, and BHT are presented in Fig. 3. Of all six examined samples, C. cinnamon oil showed the highest activity with statistical significance (Fig. 3) compared to α-tocopherol and BHT at concentrations of 5 mg · mL^{-1} and 2.5 mg · mL^{-1} and BHA at concentrations of

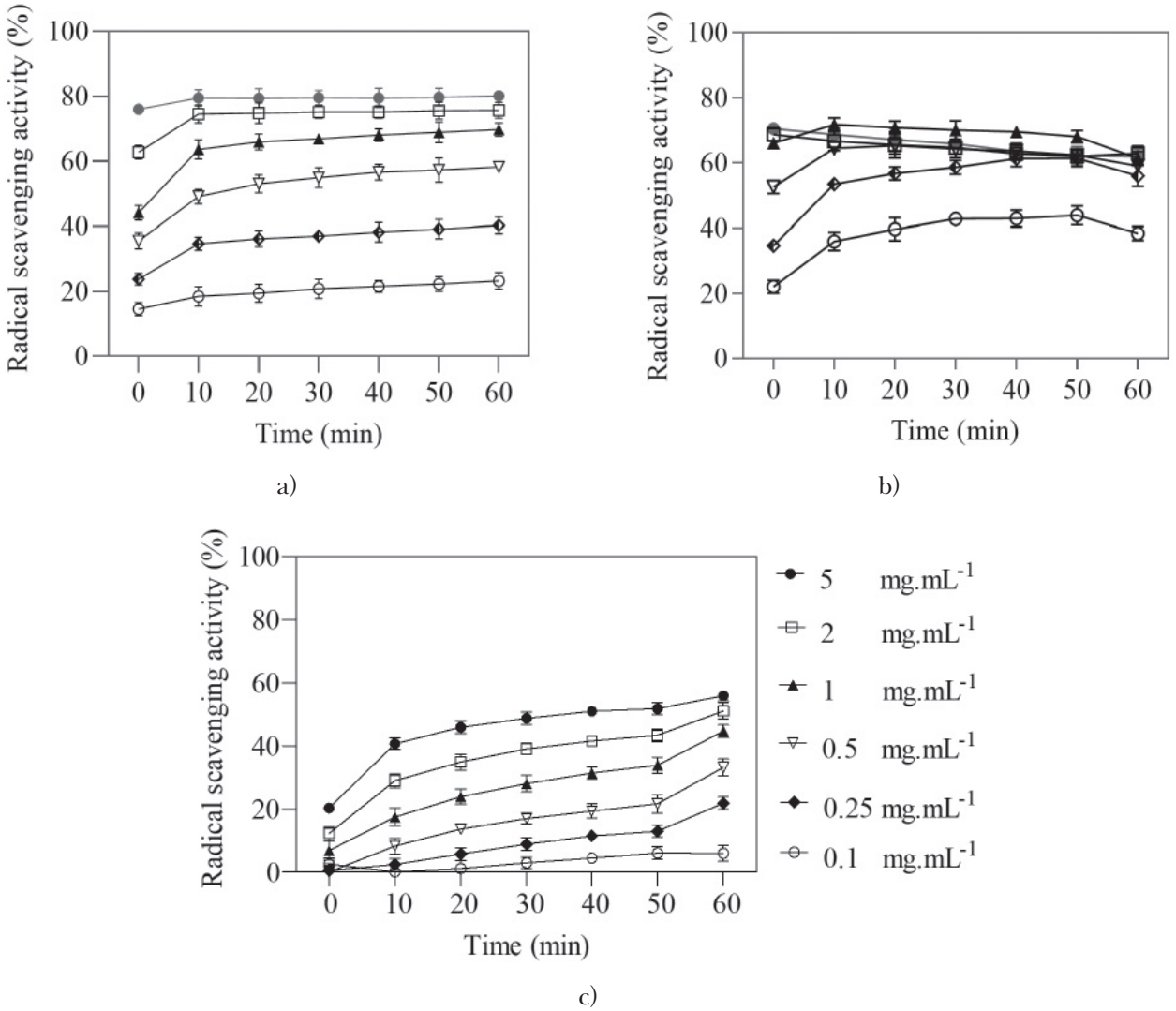

Fig. 2. Kinetic profile of DPPH radical scavenging by (a) Ceylon cinnamon bark oil, (b) clove oil and (c) thyme oil at 0.1–5 mg · mL^{-1}. Data are given as the mean ± standard deviation (n = 5).

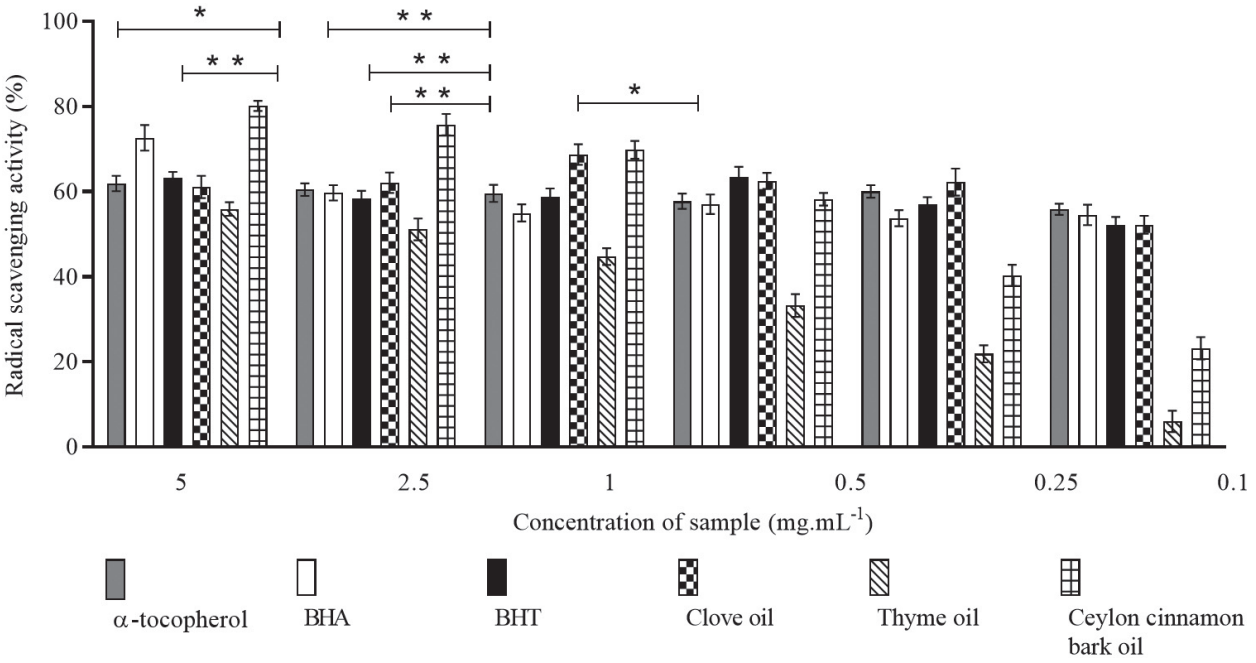

Fig. 3. Radical scavenging activity of α-tocopherol, BHA, BHT, Ceylon cinnamon bark oil, clove oil and thyme oil at 5—0.1 mg · mL^{-1} after 60 min of incubation. Data are given as the mean ± standard deviation (n = 5). Lines above the histograms indicate a statistically significant difference between the EO at a given concentration *vs.* α-tocopherol, BHA and BHT at $p < 0.05$(*), $p < 0.01$(**).

2.5 mg · mL^{-1} and 1.0 mg · mL^{-1}. Differences in RSA values of EOs and synthetic antioxidants at other concentrations evaluated were not statistically significant. Nanasombat and Wimuttigosol (2011) found that among the eight spice Eos in their study, C. cinnamon bark oil showed not only the highest antibacterial activity but also the strongest DPPH radical scavenging activity (61 % RSA) at 1 mg · mL^{-1}, which comparable to our result (63 % RSA) in Fig. 2a for the same concentration of C. cinnamon oil after 30 min of incubation. EI-Ghorab and EI-Massry (2013) studied cinnamon bark and clove bud oils obtained by supercritical fluid extraction and determined the DPPH radical scavenging activity of 47 % and 91 %, respectively, at the concentration of 500 ppm · mL^{-1} of these oils. In our study, RSA values of 58 % and 59 % were measured for C. cinnamon and clove oils, respectively, at the same concentration of 0.5 mg · mL^{-1}; however, it should be emphasised that these oils were obtained by steam distillation. Wang et al. (2017) determined the RSA value of 94 % and 69 % for clove and thyme oils, respectively, at 1 mg · mL^{-1} in the DPPH test, which are slightly higher values than our results (61 % and 45 % RSA) obtained at the same concentration.

Ferric reducing antioxidant power of essential oils

One possible way to counteract the action of free radicals is to reduce trace metal ions (especially from polluted environment), which are able to form reactive forms in the human body, especially on the skin surface. The FRAP method is an effective method for this assessment. Reducing power ability of test compounds exhibited a similar pattern as the radical scavenging assay.

From the FRAP values summarised in Tab. 2 it is clear that the reducing power (RP) of the test samples has a similar but not the same pattern as the radical scavenging assay. RP value of C. cinnamon oil at 5 mg · mL^{-1} is higher (1.64 mmol · L^{-1} of Trolox Eq.) than that of α-tocopherol and BHT (1.42 and 0.80 mmol · L^{-1} of Trolox Eq., respectively), but lower than that of BHA (1.86 mmol · L^{-1} of Trolox Eq.). At the same concentration, the RP values of oregano, tea tree, clove, thyme, and ylang-ylang oils were 1.22, 0.96, 0.76, 0.75, and 0.58 mmol · L^{-1} of Trolox Eq., respectively. Basil, juniper, lavender, and rosemary oils showed negligible RP values (Tab. 2). Olszowy and Dawidowicz (2016) determined the RP value of C. cinnamon bark oil at 0.5 mg · mL^{-1} to be twice that of thyme oil, which is comparable to our RP results for these oils at 5 mg · mL^{-1} (Table 2). Nanasombat and Wimuttigosol (2011) found by FRAP assay that C. cinnamon bark oil has the strongest reducing capacity of the eight spice essential oils studied.

Components of four most interesting essential oils

Essential oils are complex mixtures of volatile compounds with strong fragrance. To identify anti-

Tab. 2. Radical scavenging activity, IC50 and reducing power of ten natural essential oils and three synthetic reference antioxidant compounds.

Sample	Sample concentration [mg·mL^{-1}]			
	5	5	5	2
	DPPH assay after 60 min		FRAP assay after 30 min	
	RSA [%]	IC50 [mg·mL^{-1}]	TROLOX Equivalent [mmol·L^{-1}]	
α-tocopherol	61.90 ±2.79	0.88 ±0.01	1.42 ±0.04	1.36 ±0.03
BHA	72.65 ±1.84	0.84 ±0.02	1.86 ±0.02	1.81 ±0.02
BHT	61.30 ±1.84	0.93 ±0.05	0.80 ±0.03	0.72 ±0.03
Basil oil	14.05 ±1.34	‡	0.20 ±0.03	0.09 ±0.01
C. cinnamon oil	81.20 ±1.56	0.41 ±0.02	1.64 ±0.03	0.81 ±0.02
Clove oil	63.15 ±2.90	0.82 ±0.02	0.76 ±0.02	0.31 ±0.01
Juniper oil	19.00 ±2.12	‡	0.07 ±0.03	clouding/lack of colour
Lavender oil	23.00 ±1.41	‡	0.07 ±0.02	clouding/lack of colour
Oregano oil	44.30 ±1.13	‡	1.22 ±0.01	0.67 ±0.03
Rosemary oil	10.15 ±2.19	‡	0.02 ±0.01	clouding/lack of colour
Tea tree oil	51.05 ±1.48	‡	0.96 ±0.02	0.44 ±0.02
Thyme oil	56.95 ±1.48	0.99 ±0.02	0.75 ±0.01	0.73 ±0.02
Ylang-ylang oil	55.15 ±1.20	1.03 ±0.02	0.58 ±0.01	0.28 ±0.01

RSA: Radical Scavenging Activity.

IC50: Median Inhibition Concentration.

‡: IC50 cannot be calculated (RSA values are around or less than 50 %).

radical agents and potential skin allergens, the four essential oils (C. cinnamon, clove, thyme and ylang-ylang) that showed the highest antiradical activity in previous tests were analysed by GC-MS (Table 3). This study confirmed the major constituent of C. cinnamon (*Cinnamomum zeylanicum*) bark oil to be cinnamaldehyde (58.7 %), which gives cinnamon its flavour and aroma as well as its beneficial and harmful properties (will be discussed later). Cinnamon aldehyde is followed by linalool (5.8 %), eugenol (4.9 %), caryophyllene (3.8 %), D-limonene (3.6 %) and α-terpineol (1.1 %). These findings are comparable with the results of other authors (Wong et al., 2014; Nabavi et al., 2015; Weeratunga et al., 2015) for *Cinnamomum zeylanicum* bark oil, although small differences (depending on geographical origin, vegetative stage, growing season and processing) were recorded. It should be emphasised that the genus *Cinnamomum* (family *Lauraceae*) includes about 250—350 species worldwide and their composition varies considerably (Abdelwahab et al., 2017). To date, more than 300 volatile constituents of various cinnamon species essential oils have been identified (Wong et al 2014). For example, in a study by Abdelwahab et al. (2017), linalool (36.0 %), methyl eugenol (12.8 %), limonene (8.3 %), α-terpineol (7.8 %), terpinen-4-ol (6.4 %), γ-terpinene (3.5 %), α-terpinene (2.3 %) and 1,8-cineole (2.3 %) were identified in *Cinnamomum altissimum* Kosterm bark oil, which are marked differences compared to the composition of *Cinnamomum zeylanicum* bark oil. Kačániová et al. (2021) studied *Cinnamomum cassia* bark oil by GC–MS and identified cinnamaldehyde (61.6 %), trans-4-methoxycinnamaldehyde (13.8 %), cinnamyl acetate (5.4 %) and o-hydroxycinnamic acid (4.1 %) as the major constituents. In addition, it is necessary to distinguish cinnamon bark oil and more cost-effective cinnamon leaf oil which is also different in the composition (Yang et al., 2022). EO from C. cinnamon bark contains 65 to 80 % of cinnamaldehyde and 5 to 10 % of eugenol, while EO from C. cinnamon leaves contains only 1 to 5 % of cinnamaldehyde but up to 70 to 95 % of eugenol (Rao and Gan, 2014).

The major volatile constituent of clove oil is eugenol (82.4 %) which causes its specific odour as well as its beneficial and harmful properties (discussed later). The other three major constituents include caryophyllene (9.0 %), humulene (4.1 %) and eugenol acetate (1.6 %). These results are compatible with those obtained by other authors for this species, *E. caryophyllus,* (Chaieb et al., 2007; Amelia et al., 2017; Rodríguez et al., 2018). According to the DPPH assay of the selected essential oil components by Horvathova et al. (2014), eugenol showed the highest antioxidant activity compared to thymol.

Previous research by several authors (Nanasombat and Wimuttigosol, 2011; Sharma et al., 2016; Suryanti et al., 2018; Tanaka et al., 2019) has shown that the strong DPPH scavenging activity of C. cin-

namon oil and clove oil is mainly caused by cinnamaldehyde and eugenol, respectively, the primary components of these oils. Both cinnamaldehyde (3-phenyl-2-propanal) and eugenol (2-methoxy-4-(2-propenyl) phenol) belong to phenylpropanoid class of phytochemicals. Cinnamaldehyde bears an aldehyde group on the benzene ring linked via a three carbon chain, while eugenol has one hydroxy

Tab. 3. Main volatile constituents of four essential oils with the highest antiradical activity among the ten samples.

Class	Constituent	CAS number	C. cinnamon bark oil	Clove oil	Thyme oil	Ylang-ylang oil
			Constituent content (wt. %)			
Monoterpenes and their derivatives	α-Pinene	80-56-8	0.20	–	6.25	–
	β-Pinene	18172-67-3	0.27	–	0.94	–
	Tricyclene	508-32-7	–	–	2.03	–
	γ-Terpinene	99-85-4	0.68	–	0.15	–
	D-Limonene*	5989-27-5	3.63	–	–	–
	Cyclofenchene	488-97-1	–	–	1.48	–
	Pseudolimonene	499-97-8	–	–	0.69	–
	Carvestrene	38738-60-2	–	–	0.77	–
	Calarene	17334-55-3	–	–	–	0.24
Monoterpene alcohol and its derivatives	α-Terpineol	98-55-5	1.07	–	3.16	–
	Linalool*	78-70-6	5.79	0.31	5.49	9.97
	Geraniol*	106-24-1	–	–	–	7.54
	Cinnamyl alcohol*	4407-36-7	–	–	–	0.88
Sesquiterpenes and their derivatives	β-Caryophyllene	87-44-5	3.76	8.97	1.08	–
	α-Humulene	6753-98-6	–	4.05	0.13	3.31
	γ-Bisabolene	13062-00-5	–	0.28	–	–
	α-Amorphene	20085-19-2	–	–	–	9.40
	β-Cubebene	13744-15-5	–	–	–	1.96
	β-Copaene	18252-44-3	–	–	–	0.40
	α-Farnesene	502-61-4	–	–	–	10.33
	β-Cadinene	523-47-7	–	–	–	2.63
	Cedrol	77-53-2	–	–	–	0.33
	tau-Muurolol	19912-62-0	–	–	–	1.18
Phenol and its derivatives	Eugenyl acetate	93-28-7	–	1.58	–	–
	Eugenol*	97-53-0	4.88	82.43		0.66
Polycyclic sesquiterpene	Caryophyllene oxide	1139-30-6	0.31	0.29	0.52	
Diterpenes	Germacrene D	37839-63-7	–	–	–	6.53
	α-Cadinol	481-34-5	–	–	–	1.40
Aldehydes	Benzaldehyde	100-52-7	0.21	–	–	–
	Cinnamal*	104-55-2	58.72	–	–	–
	o-Methoxy cinnamal	1504-74-1	0.70	–	–	–
Terpenoidic phenols	Thymol	89-83-8	–	–	42.13	–
	Benzene, 1-methoxy-4-methyl	104-93-8	–	–	–	1.70
	Phenylethyl alcohol	60-12-8	–	–	–	
	Acetic acid, phenylmethyl ester	140-11-4	–	–	–	4.75
Other class	Other compounds		qs 100	qs 100	qs 100	qs 100

*Fragrance allergen according to the EU Cosmetics Regulation 1223/2009 (EC, 2020).

and one methoxy group directly attached to the ring. The effect of cinnamaldehyde and eugenol on DPPH is thought to be due to their hydrogen donating ability. Gulcin (2012) reported that eugenol exhibits higher radical scavenging activity compared to cinnamaldehyde because it easily donates a hydrogen atom to the hydroxyl (OH) moiety directly attached to the benzene ring. Although in our study, more eugenol was detected in clove oil (82.4 %) than in C. cinnamon oil (4.9 %), C. cinnamon oil showed slightly better antiradical activity. This can be explained by the fact that EOs are phytochemical complexes of aromatic components acting synergistically, the significant antioxidant activity being attributed mainly to the presence of phenolic and polyphenolic substances. Thus, eugenol, cinnamaldehyde (58.7 %), o-methoxy cinnamal (0.7 %) and other constituents of C. cinnamon oil are assumed to work together to quench the DPPH radical. According to a study by Suryanti et al. (2018), o-methoxy cinnamal in particular is capable of relatively high antiradical activity. Thymol (42.1 %) is a dominant substances of thyme (*Thymus vulgaris)* oil (Tab. 3), followed by α-pinene (6.3 %), linalool (5.5 %), α-terpineol (3.2 %), tricyclene (2.0 %), cyclofenchene (1.5 %), β-caryophyllene (1.1 %) and other compounds. Ahmad et al. (2014) determined up to 60.2 % of thymol in the *T. vulgaris* oil from a different geographical location, which confirms the variability of this EO composition. α-Farnesene (10.3 %) was determined as the main compound of ylang-ylang oil (Tab. 3) followed by linalool (10.0 %), α-amorphene (9.4 %), geraniol (7.5 %) and germacrene D (6.5 %).

Other beneficial properties of cinnamon and clove oils for cosmetic purposes are their antimicrobial activities, which have already been well established in many studies (Nanasombat and Wimuttigosol, 2011; Sharma et al., 2016; Kačániová et al., 2021). Tanaka et al. (2019) in a ten-week *in vivo* and *in vitro* study indicated that topical application of cinnamaldehyde restored UVB-mediated downregulation of cutaneous structural collagen, suggesting that cinnamon oil could protect the skin also from UVB-induced photoaging.

However, the use of EOs in dermal applications has also its downsides and is not without risk. The Scientific Committee on Consumer Safety (SCCS), a body of the European Commission (EC), has warned that contact allergy to fragrances is relatively common affecting 1 to 3 % of the general population (SCCS, 2011). The EC (2020) has therefore issued a list of the 25 most allergic compounds, among which are several components of essential oils. The most common symptoms of allergic contact dermatitis caused by an allergen present in EOs are itching, redness and flaking, which usually occur at the site of contact with the EO but may extend beyond this area (Weintraub et al., 2015; Sarkic and Stappen, 2018).

To ensure that an allergic consumer is adequately informed, these substances (regardless of whether they originate from a chemical synthesis or from nature) must appear on the label of the cosmetic product when present in the finished formula at certain concentrations (tresholds: 0.001 % in leave-on cosmetics, e.g. face cream, after shave-lotion, and 0.01 % in rinse-off cosmetics, e.g. shaving cream (EC, 2020)). This information makes it possible to avoid buying and using an allergen-containing product. Thus, if C. cinnamon oil or clove oil is used in a cosmetic product as an antiradical and flavour component at the concentration of 5 $mg \cdot mL^{-1}$ (0.5 % w/v), according to the results of our GC-MS analysis, the product will contain the following amounts of contact allergens: 0.29 % cinnamaldehyde, 0.03 % linalool, 0.02 % D-limonene and 0.02 % eugenol or 0.41 % eugenol and 0.002 % linalool, respectively (Table 3). In case of leave on products, all identified allergens have to be listed on the packaging in the list of ingredients according to the International Nomenclature of Cosmetic Ingredients (EC, 2020). This product would not be suitable for consumers allergic to these substances. It should be emphasised that the vast majority of mass-produced cosmetic products contain several allergens while not posing a risk of allergic manifestations in a significant part of the population (Hojerová and Martiniaková, 2021).

Conclusion

The present study indicates that C. cinnamon and clove essential oils could be applied as natural alternatives and effective substituents of synthetic antioxidants in cosmetic products due to their remarkable antiradical activity at 5 $mg \cdot mL^{-1}$ (DPPH scavenging activity of 81 % and 63 %, respectively, and Ferric reducing antioxidant power of 1.64 and 0.76 Trolox Eq. In $mmol \cdot L^{-1}$, respectively). However, if such concentration of C. cinnamon oil or clove oil is used in skin care products, their content of approx. 0.29 % of cinnamaldehyde or 0.41 % of eugenol must be indicated on the packaging of the final product as a warning to consumers with allergies.

Acknowledgement

The work was supported by the Scientific Grant Agency of the Slovak Republic (VEGA 2/0136/20), Slovak Research and Development Agency (APVV-16-0088) and by the Operational program Integrated Infrastructure within

the project: Demand-driven research for the sustainable and innovative food Drive4SIFood 313011V336 co-financed by the European Regional Development Fund.

References

Abdelwahab SI, Mariod AA, Taha MME, Zaman FQ, Abdelmageed AHA, Khamis S, Sivasothy Y, Awang (2017) Arab. J. Chem. 10(1): 131—135.

Abelan US, de Oliva AC, Cacoci ESP, Martinis TEA, Giacon VM, Velasco MVR, de Castro Lima CRR (2021) J. Cosmet. Dermatol. 00: 1—12.

Ácsová A, Hojerová J, Tobolková B, Martiniaková S (2021) Chem. Sel. 6: 4495—4505.

Ahmad A, Van Vuuren S, Viljoen A (2014) Molecules 19(3): 2896—2910.

Alam MN, Bristi NJ, Rafiquzzaman M (2013) Saudi Pharm. J. 21: 143—152.

Akar Z, Küçük M, Doğan H (2017) J. Enzyme Inhib. Med. Chem. 32(1): 640—647.

Amelia B, Saepudin E, Cahyana AH, Rahayu DU, Sulistyoningrum AS, Haib J (2017) AIP Conference Proceedings. 1862,030082.

Arantes SM, Picarra A, Guerreiro M, Salvador C, Candeias F, Calderia AT, Martins MR (2019) Food Chem. Toxicol. 133: 110747.

Behbahani BA, Falah F, Arab FL, Vasiee M, Yazdi FT (2020) Evid Based Complement Alternat. Med. 2: 1—8.

Benzie IFF, Strain JJ (1996) Anal. Biochem. 239: 7—76.

Brainina K, Stozhko N, Vidrevich M (2019) Antioxidants (Basel). 8(8): 297.

Brand-Williams W, Cuvelier ME, Berset C (1995) Food Sci. Technol. 1: 25—30.

Chaieb K, Hajlaoui H, Zmantar T, Kahla-Nakbi AB, Rouabhia M, Mahdouani K, Bakhrouf A (2007) Phytother. Res. 24(6): 501—506.

Chen Z, Bertin R, Froldi G (2013) Food Chem. 138(1): 414—420.

CIR (2019) Expert Panel for Cosmetic Ingredient Safety. Safety Assessment of BHT as Used in Cosmetics, 1—92. https://www.cir-safety.org/sites/default/files/BHT.pdf

Coy-Barrera E (2020) Analysis of betalains (betacyanins and betaxanthins) In Recent Advances in Natural Products Analysis, Chapter 17.4.1 Antiradical and antioxidant activity, 593—619.

Echegaray N, Pateiro M, Munekata PES, Lorenzo JM, Chabani Z, Farag MA, Domínguez R (2021) Molecules. 26: 3880—3900.

EI-Ghorab AH, EI-Massry KF (2013) J. Ess. Oil Bear Plants. 6(1): 9—20.

EC (2020) European Parliament and the Council. Regulation (EC) No 1223/2009 on Cosmetic Products (recast). Off. J. EU, L 342/59; consolidated version 01/05/2020.

Fiume MM, Bergfeld WF, Belsito DV (2018) Int. J. Toxicol. 37(2): 61S—94S.

Gotmare S (2018) JETIR 5(6): 21—25.

Gulcin I, Elmastas M, Aboul-Enein HY (2012) Arab. J. Chem. 5: 489—499.

Hatwalne MS (2012) Indian J. Anaesth. 56(3): 227—233.

Hojerová J, Martiniaková S (2021) Cosmetic Chemistry and Technology (in Slovak). Book. Spectrum STU, Bratislava, 235 pgs.

Horvathova E, Navarova J, Galova E, Sevcovicova A, Chodakova L, Snahnicanova Z, Melusova M, Kozics K, Slamenova D (2014) J. Agric. Food Chem. 62(28): 6632—6639.

Kačániová M, Galovičová L, Valková V, Tvrdá E, Terentjeva M, Žiarovská J, Kunová S, Savitskaya T, Grinshpan D, Štefániková J, Felsöciová S, Vukovic N, Kowalczewski PL (2021) Open Chemistry. 19: 214—227.

Labat-Robert J, Robert L (2014). Pathol. Biol. 62(2): 61—66.

L'Oréal Group Website (2020) BHT. https://inside-ourproducts.loreal.com/ingredients/bht

Mahomoodally F, Aumeeruddy-Elalfi Z, Venugopala KN, Hosenally M (2019) Saudi J. Biol. Sci. 26: 1779—1788.

Marchi, RC, Campos IAS, Santana VT, Carlos RM (2022) Coord. Chem. Rev. 451(1): 214275.

Nabavi SF, Di Lorenzo A, Izadi M, Sobarzo-Sánchez E, Daglia M, Nabavi SM (2015) Nutrients. 7(9): 7729—7748.

Nanasombat S, Wimuttigosol P (2011) Food Sci. Technol. 20: 45—53.

Olszowy M, Dawidowicz A (2016) Monatsh Chem. 147: 2083—2091.

Ortuño J, Serrano R, Jordán MJ, Bañón S (2016) Food Chem. 190: 1056—1063.

Phaniendra A, Jestadi DB, Periyasamy L (2015) Indian J. Clin. Biochem. 30(1): 11—26.

Pizzino G, Irrera N, Cucinotta M, Pallio G, Mannino F, Arcoraci V, Squadrito F, Altavilla D, Bitto A (2017) Oxid. Med. Cell. Longev. 8416763.

Poljšak B, Dahmane R (2012) Dermatol. Res. Pract. 135206, 4 pgs.

Rao PV, Gan SH (2014) Evid. Based Compl. Alternat. Med. 642942.

Ribeiro JS, Santos MJMC, Silva LKR, Pereira LCL, Santos IAS, da Silva Lannes SC, da Silva MV (2019) Meat Sci. 148: 181—188.

Rodríguez JDW, Peyron S, Rigou, P, Chalier P (2018) PLoS One. 13(11): e0207401.

Sarkic A, Stappen (2018) Cosmetics. 5(1): 11.

SCCS (2011) Scientific Committee on Consumer Safety. Opinion on Fragrance allergens in cosmetic products. SCCS/1459/11. European Commission Health & Consumers. 1—136.

Sharma UK, Sharma AK, Pandey AK (2016) BMC Compl. Alter. Med. 16: 156.

Sudarikov DV, Krymskaya YV, Melekhin AK, Shevchenk OG, Rubtsova SA (2021) Chem. Pap. 75: 2957—2963.

Suryanti V, Wibowo FR, Khotijah S, Andaluck N (2018) IOP Conf. Ser. Mater. Sci. Eng. 333 012077.

Tanaka Y, Uchi H, Furue M (2019) J. Dermatol. Sci. 96 (3): 151—158.

Tepe AS, Ozaslan M (2020) Ind. Crops. Prod. 145: 112069.

Wang HF, Yih KH, Yang CHS, Huang FF (2017) J. Food Drug. Anal. 25: 881—889.

Weeratunga HD, Ganegamage SK, Premakumara S (2015) Conference: The 35th Annual Sessions of the Institute of Biology at Sri Lanka.

Weintraub GS, Lai IN, Kim CN (2015) World J. Dermatol. 4: 95–102.
Wong YC, Ahmad-Mudzaqqir MY, Wan-Nurdiyana WA (2014) Orient J. Chem. 30(1): 37–47.
Yang Y-L, Al-Mahdy DA, Wu M-L, Zheng X-T, Piao X-H, Chen A-L, Wang S-M, Yang Q, Ge Y-W (2022) Food Chem. 366(1): 130576.
Yang X, Sun Z, Wang W, Zhou Q, Shi G, We F, Jiang G (2018) Sci. Total Environ. 643: 559–568.

sciendo

On the energetics of radical adduct formation of OH• with phenol analogs and aniline

Dagmar Štellerová, Vladimír Lukeš

Institute of Physical Chemistry and Chemical Physics, Slovak University of Technology in Bratislava, Radlinského 9, SK-812 37 Bratislava, Slovakia
dagmar.stellerova@stuba.sk

Abstract: Theoretical studies on aniline, phenol, benzenethiol, benzeneselenol, and their corresponding adducts with hydroxyl radical in possible positions on a hydrocarbon ring are presented. Bond dissociation enthalpies, related to radical scavenging of primary antioxidants, were calculated using the M06–2X/6–311+G** method. Calculated data were compared with available experimental data. Preferable homolytic bond dissociation of the presented molecules with OH• through functional groups X—OH followed by the *m*–OH ones has been confirmed. The highest antioxidant activity among the investigated positions is predicted for benzeneselenol. Also, the formation of non-covalent van der Waals structures has been shown as important in radical scavenging.

Keywords: Bond Dissociation Enthalpy; DFT; hydroxyl radical; thermodynamics

Introduction

Free oxygen radicals are reactive species capable of independent existence while containing at least one unpaired electron in its atomic or molecular orbitals. Generally, radicals such as hydroxyl (OH•), hydroperoxyl (HO_2•), or superoxide radicals (O_2•) are generated by cellular metabolism providing a number of physiological benefits. For instance, they are involved in the immune response of neutrophils and macrophages to pathogens, in cellular signalling pathways, enzymatic reactions or in the activation of nuclear transcription and gene expression (Bayir, 2005).

If the production of free radicals in a cell exceeds its antioxidant capacity, breakage of biological molecules such as lipids, proteins, or DNA can occur. These molecular defects often involve excessive generation of the hydroxyl radical (OH•), which is highly reactive and unselective and serves as both a primary toxicant and a source of secondary toxicants (Borg et al., 1981). DNA strand damage caused by hydroxyl radicals can contribute to serious defect conditions such as cytotoxicity, mutagenesis, or carcinogenesis (Husain et al., 1987).

Generally, antioxidants are organic compounds inhibiting chemical reactions that produce free radicals as they tend to bind with these reactive intermediates during the oxidative process. Phenols together with secondary aromatic amines belong to important primary antioxidants (Wolf and Kaul, 1992). Phenols and polyphenolic compounds represent natural antioxidants produced by bacteria, fungi, or plants (Hättenschwiler and Vitousek, 2000). Moreover, they are synthesized in many specialized reactions in chemical and pharmaceutical industry. Amines are synthetic compounds which have essential use in dye production (Lukeš and Hartmann, 2021), as stabilizers or therapeutics (Lawrence, 2005). Recently, antioxidant activity in reactions with glutathione peroxidase was observed for sulfur and selene analogs of phenol (Tanini et al., 2019). These experiments support the hypothesis that antioxidant activity of benzeneselenol derivates is useful in anti–inflammatory and anticarcinogenic therapy (Jacob et al., 1999).

The ability of antioxidants to react with free radicals can be studied theoretically as well as experimentally combining thermodynamic and kinetic measurements with electrochemistry, spectroscopic or EPR techniques (Blanksby and Ellison, 2003; Luo, 2007). From the thermodynamic point of view, the bond dissociation enthalpy seems to be the most useful parameter for antioxidant activity description. However, if it is the principal quantity characterizing efficiency of a molecule as an antioxidant, experimental methods are often insufficient to interpret the acquired data accurately (errors are in tens of $kJ \cdot mol^{-1}$) (Luo, 2007).

Significant development in theoretical methods has occurred allowing to find trends in calculations of physical quantities and to specify experimental values. One of such quantum mechanical methods is Density Functional Theory (DFT), which is extensively used and able to give precise predictions of a wide range of structures. Up to this date, there have been numerous DFT works focused on radicals and their scavengers (see e.g. Klein and Lukeš, 2006; Poliak et al., 2018) utilizing different methods, higher order functionals or basis sets. However, systematic study of thermodynamically preferred hydroxyl radical adducts with aniline, phenol, benzenethiol and benzeneselenol using identical theoretical treatment has not been published. Therefore, partial aims of this study are to: (1) carry out optimal geometries of

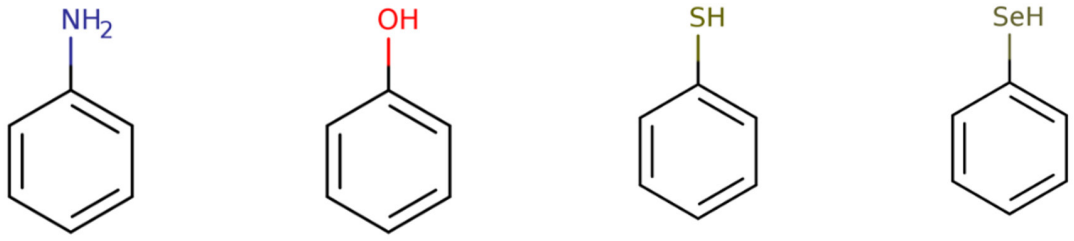

Fig. 1. Schematic structures and notations of studied molecules: aniline **(N),** phenol **(O),** benzenethiol **(S),** and benzeneselenol **(Se)**.

presented molecules (see Fig. 1) in gas phase; (2) find intermediate products associated with radical binding; (3) calculate dissociation enthalpies of provided reactions, and (4) compare obtained data with available experimental values.

Computational Details

All calculations were performed by employing Gaussian 16 software package (Frisch et al., 2016). Optimizations of parent molecules, their corresponding radicals and radical adducts were carried out by quantum chemical calculations based on density functional theory (DFT). Since the M06–2X (Lee et al., 1988; Becke, 1988) method has been proven to effectively expresses short-range and medium-range electrostatic interactions (<500 pm) (Zhao and Truhlar, 2008), this hybrid functional was applied in combination with the 6–311+G** basis set (Binkley et al., 1980). M06–2X is suggested for thermodynamic examination of organic compounds with free radicals (Walker et al., 2013). All the structures, including the radicals, were used to obtain gas-phase enthalpies at room temperature (298.15 K). All species under study are neutral. Radicals are in doublet ground spin states whereas the remaining molecules are in singlet ground spin states. Stability of the optimized geometries was confirmed by vibrational analysis (no imaginary vibrations). With respect to the fact that radical formation is independent of the presence of a solvent (difference < 5 kJ · mol^{-1}), gas-phase optimization was applied.

Radical scavenging by primary aromatic antioxidants (Gugumus, 1990), the hydrogen atom transfer (HAT) is described as:

$$\mathrm{ArH{-}XH} \rightarrow \mathrm{ArH{-}X^{\bullet}\ or\ Ar^{\bullet}{-}XH} + \mathrm{H^{\bullet}} \quad (1)$$

Homolytic bond dissociation enthalpy (*BDE*) for this reaction is calculated from the difference:

$$BDE = H(\mathrm{ArH{-}X^{\bullet}\ or\ Ar^{\bullet}{-}XH}) + H(\mathrm{H^{\bullet}}) - H(\mathrm{ArH{-}XH}) \quad (2)$$

where $H(\mathrm{ArH{-}X^{\bullet}\ or\ Ar^{\bullet}{-}XH})$ is total enthalpy of the formed radical, and $H(\mathrm{H^{\bullet}})$ is total enthalpy of the hydrogen atom. Total gas-phase enthalpy of the hydrogen atom is –1306 kJ · mol^{-1} (Rimarčík et al., 2010).

Reaction enthalpy, $\Delta H°$, of the hydroxyl radical adducts formation:

$$\mathrm{Ar{-}XH} + \mathrm{OH^{\bullet}} \rightarrow \mathrm{Ar{-}XH{-}OH^{\bullet}} \quad (3)$$

can be calculated as follows:

$$\Delta H° = H(\mathrm{Ar{-}XH{-}OH^{\bullet}}) - H(\mathrm{OH^{\bullet}}) - H(\mathrm{Ar{-}XH}) \quad (4)$$

where $H(\mathrm{OH^{\bullet}})$ is total enthalpy of the hydroxyl radical (–75.714589 Hartree), H(Ar—XH) is total enthalpy of the parent molecule and $H(\mathrm{Ar{-}XH{-}OH^{\bullet}})$ is total enthalpy of the radical adduct or the van der Waals complex.

Results and Discussion

Optimal geometries of the studied molecules show planar aromatic rings. Optimal geometry of aniline (Fig. 2) is represented by a tilted amino group bonded to a planar phenol ring with the dihedral H—N—C—C angle of 25.3 °. As for phenol analogs, all three functional groups are coplanar in the molecules with respect to the phenyl ring and their H—O—C—C, H—S—C—C and H—Se—C—C dihedral angles are 180.0 °.

Calculated *BDE* values for homolytic dissociation of **X—H** or **C—H** bonds according to Eq. 2 are shown in Table 1. For radicals containing the X—H group, two slightly different BDEs (depending on *syn-* or *anti*-orientations to **X—H**) were obtained for *ortho-* as well as for *meta-* positions. Gas-phase *BDE*s for aniline **(N)** radicals are in range of 383 kJ · mol^{-1} to 465 kJ · mol^{-1}. According to the experimental value of 386 kJ · mol^{-1} (Luo, 2007), hydrogen atom transfer on the N—H functional group is the most probable. For phenol and its analogs, *BDE* values for phenol **(O)** changed from 366 kJ · mol^{-1} to 471 kJ · mol^{-1}, for benzenethiol **(S)** they are between 326 kJ · mol^{-1} and

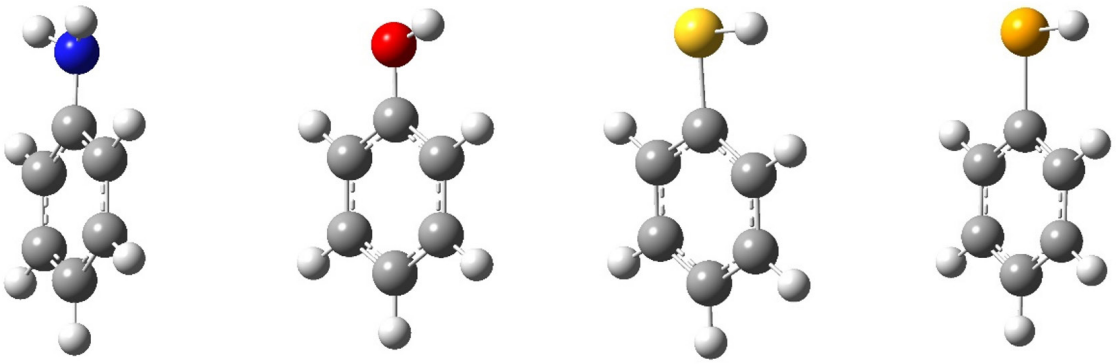

N –287.553474 Hartree | **O** –307.423022 Hartree | **S** –630.382802 Hartree | **Se** –2633.745843 Hartree

Fig. 2. Optimal gas-phase geometries and electronic DFT energies of studied molecules.

464 kJ · mol^{-1} and for benzeneselenol **(Se)** they range from 308 to 463 kJ · mol^{-1}. *BDE* values of functional groups **(X—H)** in phenol analogs are in best agreement with the experiment. On the contrary, the least preferable homolytic hydrogen atom splitting is from aromatic carbon atoms. In case of hydrogen atom abstraction from *ortho-* and *meta-* positions, hydrogen atom of the functional **X—H** group in the energetically preferred radical is oriented toward the naked carbon atom. For the alternative orientation of the **X—H** group in these radicals, the corresponding BDE values are presented in parentheses in Tab. 1. Regarding the phenyl ring, the most favorable radical formation in all four studied molecules is at the *meta-* position (*m*-H), resulting from mesomeric effect of functional groups on the conjugated phenyl system.

For each of four parent molecules, three stable OH$^{\bullet}$ radical adducts have been found. Each adduct can have various mutual spatial orientations of **O—H** and **X—H** groups. The energetically most preferred geometries are depicted in Fig. 3. If OH$^{\bullet}$ was aimed at the functional groups of parent molecules, only stable van der Waals complexes were identified. In case of aniline (**N**) and phenol (**O**), geometries of the functional groups were not affected, creating hydrogen bonds of 2.01 Å (N···H—O) for **N** and 1.91 Å (O···H—O) for the **O** structure with the OH$^{\bullet}$ radical. As for benzenethiol (**S**) and benzeneselenol (**Se**), the van der Waals interaction not only turned the functional groups out-of-plane, but also had inverse orientation with H···O distances of 2.48 Å (S—H···O—H) for **S** and 2.46 Å (Se—H···O—H) for **Se** candidates. Shortening of these distances might lead directly to the formation of an unstable transition-state complex.

Subsequently, *ortho-*, *meta-* and *para-* positions of parent molecules were attacked by OH$^{\bullet}$ (2nd to 4th column in Fig. 3). In all cases, the OH$^{\bullet}$ radical binds the respective phenol position more or less perpendicularly to the ring plane, creating bonds with lengths in the range of 1.42 Å to 1.44 Å. Similarly, geometries of **N** and **O** parent molecules were not significantly altered in any of the studied structures. On the contrary, S—H and Se—H bonds of the **S-*o*-OH, S-*m*-OH, Se-*o*-OH, Se-*m*-OH** structures (see Fig. 3) were tilted out of the ring plane. Functional groups in **S-*p*-OH** and **Se-*p*-OH** remained coplanar with the phenyl ring.

Calculated enthalpies of OH$^{\bullet}$ adducts formation (3) are collected in Table 2; negative values indicate exothermic character of the studied reactions. Although the OH$^{\bullet}$ radical is considered as an unselective and extremely reactive species, the highest exothermicity is indicated for *ortho*-positions while the lowest reaction enthalpies were found for *meta*-positions. Interestingly, minimal energy differences between radical adducts were found for benzenethiol and benzeneselenol. Formation of a van der Waals complex showed a small energetical effect (see 1st line in Tab. 2). For the sake of comparison, dissociation enthalpies of strong hydrogen

Tab. 1. Calculated M06–2X/6–311+G** gas-phase bond dissociation enthalpies (*BDE*) at 298.15 K of the studied molecules (kJ · mol^{-1}). Values in parentheses are for energetically less preferred radical structures.

	N	O	S	Se
X—H	383	366	326	308
Experiment	386[a]	363[a]	331[b]	301[a]
***o*-H**	463	464 (464)	463 (621)	459 (625)
***m*-H**	458	460 (460)	460 (463)	457 (457)
***p*-H**	465	465	464	463

[a]Luo, 2007.

[b]Bordwell.

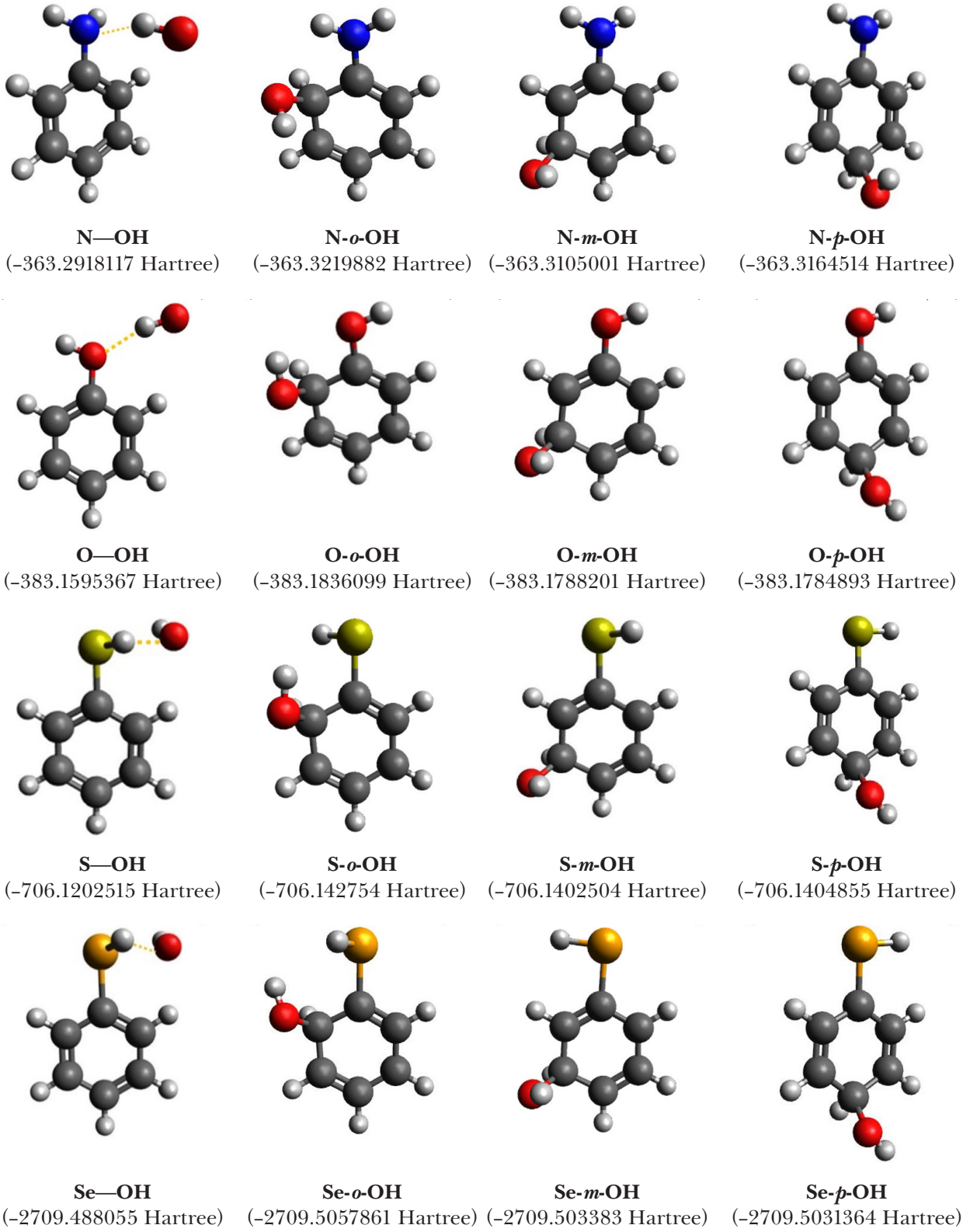

Fig. 3. Optimal gas-phase M06–2X/6–311+G** geometries of studied van der Waals structures (**X—OH**) and energetically preferred model radical adducts. Values in parentheses represent the corresponding DFT energies in Hartree.

bonds are above 20 kJ · mol^{-1} (Zheng et al, 2007). Reaction enthalpies for aniline and phenol are four times lower compared to **o-H** adducts.

If Ar—XH(—OH)$^{\bullet}$ radicals are considered as chemically unstable, elimination of water can lead to geometrically simpler radical structures

Tab. 2. Calculated M06–2X/6–311+G** gas-phase reaction enthalpies ($\Delta H°$) of van der Waals (for X—H) and radical adducts formation at 298.15 K ($kJ \cdot mol^{-1}$). Values in parentheses are calculated for energetically less preferred radical adduct structures.

	N	O	S	Se
X—H	–25	–21	–20	–33
***o*–H**	–99	–79 (–93)	–76 (–79)	–79 (–80)
***m*–H**	–71	–68 (–73)	–69(–69)	–73 (–74)
***p*–H**	–85	–66	–70	–72

Tab. 3. Calculated M06–2X/6–311+G** gas-phase reaction enthalpies (*RE*) at 298.15 K of water molecule elimination from van der Waals and radical adducts ($kJ \cdot mol^{-1}$). Values in parenthesis are calculated for energetically less preferred radical adduct structures.

	N	O	S	Se
X—H	–74	–95	–136	–140
***o*–H**	80	61 (75)	60 (215)	56 (224)
***m*–H**	48	47 (52)	48 (50)	48 (50)
***p*–H**	68	50	52	53

$$Ar—XH(—OH)^{\bullet} \rightarrow Ar—X^{\bullet} \text{ or } Ar^{\bullet}—XH + H_2O \quad (5)$$

Following reaction (5), reaction enthalpy (*RE*) of final products can be calculated:

$$RE = H(Ar—X^{\bullet}) + H(H_2O) - H(Ar—XH—OH^{\bullet}) \quad (6)$$

where $H(H_2O)$ is total enthalpy of the water molecule (–76.395438 Hartree at 298.15 K).

Reaction enthalpies for possible radical adducts or van der Waals complexes (see reaction 5) are presented in Table 3. Elimination of the water molecule from the X—H group is an exothermic process and the RE values changed in the range from –140 $kJ \cdot mol^{-1}$ for benzeneselenol to –74 $kJ \cdot mol^{-1}$ for aniline. The remaining enthalpies revealed the endothermic character of the suggested reaction mechanism. Regarding the phenyl ring, *RE* values changed with the location of the hydroxyl group, leaving *meta*-position as the most preferable for $OH^{\bullet}$ attack. According to steric effects, *o*-OH homolytic dissociation is the least probable. Interestingly, the highest reaction enthalpies were obtained for water abstraction for energetically less preferred adducts of **S** and **Se** in *ortho*-positions (see values in parentheses in Tab. 3).

Conclusion

In this study, thermodynamics of hydrogen atom abstraction from four possible positions for aniline, phenol, benzenethiol and benzeneselenol molecules were theoretically estimated and energetically preferred radical adducts with hydroxyl radical ($OH^{\bullet}$) were discussed. Optimal geometries and enthalpies were calculated using the M06–2X functional method. Comparison of homolytic bond dissociation enthalpies showed that hydrogen atom abstraction from the X—H groups is always energetically preferred while the C—H bond break on the aromatic ring in the *ortho*-position is thermodynamically less probable. Theoretical calculations indicate that the addition of a hydroxyl radical to the aromatic ring leads to stable Ar—XH—$OH^{\bullet}$ radical adducts. Moreover, interaction of $OH^{\bullet}$ and functional groups of the parent molecules generates relatively stable van der Waals complexes. It seems that these non-covalent structures are important in the radical scavenging effect. Finally, the lowest energy differences among the evaluated thermodynamic quantities were found for benzenethiol and benzeneselenol molecules.

Acknowledgement

The work has been supported by the Slovak Research and Development Agency (APVV-15-0053) and VEGA 1/0504/20. We are grateful to the HPC Centre at the Slovak University of Technology in Bratislava, which is a part of the Slovak Infrastructure of High Performance Computing (SIVVP project, ITMS code 26230120002, funded by the European Region Development Funds, ERDF) for the computational time and resources made available.

References

Bayir H (2005) Crit. Care. Med. 33: 498–501.

Becke AD (1988) Phys. Rev. A 38: 3098–3100.

Binkley JS, Pople JA, Hehre WJ (1980) J. Am. Chem. Soc. 102: 939–947.

Blanksby SJ, Ellison GB (2003) Acc. Chem. Res. 36: 255.

Bordwell FG, Zhang X-M, Satish AV, Cheng J-P (1994) J. Am. Chem. Soc. 116: 6605–6610.

Borg DC, Schaich KM, Elmore JJ (1981), Academic Press, New York: 177–186.

Frisch MJ, Trucks GW, Schlegel HB, Scuseria GE, Robb MA, Cheeseman JR, Scalmani G, Barone V, Petersson GA, Nakatsuji H, Li X, Caricato M, Marenich AV, Bloino J, Janesko BG, Gomperts R, Mennucci B, Hratchian HP, Ortiz JV, Izmaylov AF, Sonnenberg JL, Williams-Young D, Ding F, Lipparini F, Egidi F, Goings J, Peng B, Petrone A, Henderson T, Ranasinghe D, Zakrzewski VG, Gao J, Rega N, Zheng G, Liang W, Hada M, Ehara M, Toyota K, Fukuda R, Hasegawa J, Ishida M, Nakajima T, Honda Y, Kitao O, Nakai H, Vreven T, Throssell K, Montgomery JA Jr., Peralta JE, Ogliaro F, Bearpark MJ, Heyd JJ, Brothers EN, Kudin KN, Staroverov VN, Keith TA, Kobayashi R, Normand J, Raghavachari K, Rendell AP, Burant JC, Iyengar SS, Tomasi J, Cossi M, Millam JM, Klene M, Adamo

C, Cammi R, Ochterski JW, Martin RL, Morokuma K, Farkas O, Foresman JB, Fox DJ (2016) Gaussian 16, Revision B.01, Gaussian, Inc., Wallingford CT.
Gugumus F (1990) Oxidation inhibition in organic materials, 1, CRC Press, Boca Raton.
Hättenschwiler S, Vitousek PM (2000) Trends in Ecology & Evolution 15: 238–243.
Husain SR, Cilurd J, Cillard P (1987) Phytochemistry 26: 2489–2491.
Jacob C, Maret W, Vallee BL (1999) Proc. Natl. Acad. Sci. USA 96: 1910–1914.
Klein E, Lukeš V (2006) J. Phys. Chem. 110: 12312–12320.
Lawrence SA (2005) Amines: Synthesis, Properties and Applications, Cambridge University Press, Cambridge.
Lee C, Yang W, Parr RG (1988) Phys. Rev. B 37: 785–789.
Lukeš V, Hartmann H (2021) Color. Tech. 137: 389–398.
Luo YR (2007) Comprehensive Handbook of Chemical Bond Energies, CRC Press, Boca Raton, New York.
Poliak P, Škorňa P, Lukeš V, Klein E (2018) Food. Chem. 268: 542–549.
Rimarčík J, Lukeš V, Klein E, Ilcin M (2010) J. Mol. Struct. 952: 25–30.
Tanini D, Bonardi C, Viglianisi C, Capperucci A, Menichetti S (2019) Catalysts 9, 333.
Walker M, Harvey AJ, Sen A, Dessent CE (2013) J. Phys. Chem. A. 117: 12590–12600.
Wolf R, Kaul BL (1992) Plastics, Additives, Ullmann's encyclopedia of industrial chemistry: VCH.
Zhao Y, Truhlar DG (2008) Theor. Chem. Acc. 120: 215–241.
Zheng J, Fayer MD (2007) J. Am. Chem. Soc. 129: 4328–4335.

sciendo

Binary mixtures containing imidazolium ionic liquids: properties measurement

Pavol Steltenpohl, Elena Graczová

Department of Chemical and Environmental Engineering, Faculty of Chemical and Food Technology, Slovak University of Technology in Bratislava, Radlinského 9, 812 37 Bratislava, Slovak Republic
pavol.steltenpohl@stuba.sk

Abstract: Densities and transport properties (dynamic viscosity) of pure imidazolium ionic liquids 1-butyl-3-methylimidazolium acetate and 1-butyl-3-methylimidazolium dicyanamide and their binary mixtures with water and ethanol were measured within the temperature range of 293.15–333.15 K. Obtained experimental data were used to calculate excess molar volume and viscosity deviation. For the chosen binary mixtures, variations of excess molar volume, partial molar volumes of mixture components and of the viscosity deviation with the binary mixture composition were correlated using the Redlich-Kister equation. In addition, variation of viscosity with the binary mixture composition and temperature was fitted using the Jouyban-Acree model.

Keywords: Imidazolium ionic liquids, density, dynamic viscosity, excess molar volume, viscosity deviation, Redlich-Kister equation, Jouyban-Acree equation

Introduction

Ionic liquids (ILs) are characterized as salts in the liquid state (molten salts) that present several interesting properties (Welton, 1999). Especially, their negligible saturated vapor pressure over a large temperature range makes ILs different compared to commercially used 'traditional' solvents. Although, ILs are considered novel solvents in chemical technology, they already have found application or have been indicated as interesting medium for numerous processes, e.g. in carbon capture (Galán Sánchez et al., 2007), absorption of sour gases (Zeng et al., 2014), construction of fuel cells (Armand et al., 2009), separations of interesting metabolites from aqueous media (Perreiro et al., 2012; Graczová & Steltenpohl, 2015), as extraction solvents in petroleum and hydrocarbon industries (Meindersma et al., 2010) or as a solvent and, at the same time, a catalyst for organic syntheses (Greaves & Drummond, 2008), etc.

The success of ILs application dwells in their unique thermophysical and phase-equilibria properties. It is further busted by the versatility of ILs synthesis that allows preparing tailor-made ionic liquids for each application (Nieto de Castro et al., 2010). Among others, volumetric and transport properties of ILs are important in the analysis of fluid flow as well as in chemical-engineering correlations and heat-transfer calculations (Bajić et al., 2014).

Although several computer-based contribution procedures for the prediction of the properties of ILs and their mixtures have recently been developed, experimental estimation of these properties is applied as an approval of computed properties as well as a new input for the calculation procedure database (Jacquemin et al., 2008).

Here, density and viscosity of two ionic liquids, 1-butyl-3-methylimidazolium acetate ([bmim]Ac) and 1-butyl-3-methylimidazolium dicyanamide ([bmim]DCA) and their binary mixtures with water and with ethanol at temperatures of 20 °C, 40 °C and 60 °C are presented. Experimental data were correlated in terms of excess molar volume and the density difference was determined by the Redlich-Kister equation (Redlich & Kister, 1948). Viscosity data were also correlated using the Jouyban-Acree model (Acree, 1992).

Theoretical

Volumetric properties of the binary mixtures of chosen ionic liquids with water and ethanol were expressed as excess molar volumes and component partial molar volumes. Variation of the excess molar volumes of binary mixtures and that of component partial molar volumes with the mixture composition were correlated using the Redlich-Kister equation (Redlich & Kister, 1948).

Excess properties represent deviation of the binary liquid mixture behavior from that of the ideal mixture. Excess molar volume, V^{E}, is defined by the following equation:

$$V^{\mathrm{E}} = V_{\mathrm{m}} - \sum_i x_i V_i^* \qquad (1)$$

where V_{m} represents the mixture molar volume, x_i is the mole fraction of i-th component of the binary mixture and V_i^* is the i-th component's molar volume.

Molar volumes of binary mixtures and that of pure

component i (x_i = 1) were computed using experimental density values (Eq. (2)).

$$V_{\mathrm{m}} = \frac{\sum_i x_i M_i}{\rho} \tag{2}$$

The excess molar volume values are frequently correlated using the Redlich-Kister equation that adopts the following form:

$$V^{\mathrm{E}} = x_1 x_2 \sum_n C_n \left(x_1 - x_2\right)^{n-1} \tag{3}$$

C_n being the model parameters and n the polynomial order.

Partial molar volumes of mixture components, $\overline{V}_i$, were expressed in the following form (see e.g. Wood & Battino, 1990).

$$\overline{V}_i = V^{\mathrm{E}} + V_i^* + \left(1 - x_i\right)\left(\frac{\partial V^{\mathrm{E}}}{\partial x_i}\right)_{p,T} \qquad i = 1, 2 \tag{4}$$

The term representing the variation of excess molar volume with mixture composition was derived by differentiating Eq. (3).

Viscosity of the studied binary mixtures was fitted either in terms of density differences variation with mixture composition using the Redlich-Kister equation or directly applying the Jouyban-Acree model equation.

Viscosity deviation, $\Delta\eta$, expresses the difference between the measured binary mixture viscosity and the value computed as linear combination of pure components' viscosities (Eq. (5)).

$$\Delta\eta = \eta_{\mathrm{m}} - \sum_i x_i \eta_i \tag{5}$$

where η_{m} is the measured mixture viscosity and η_i is the i-th component viscosity.

The Redlich-Kister equation used to correlate the viscosity difference is given as:

$$\Delta\eta = x_1 x_2 \sum_n C_n \left(x_1 - x_2\right)^{n-1} \tag{6}$$

Viscosity variation with the mixture composition and temperature was also correlated using the Jouyban-Acree equation in the following form:

$$\ln \eta_{\mathrm{m},T} = \sum_i x_i \ln \eta_{i,T} + x_1 x_2 \sum_n J_n \frac{\left(x_1 - x_2\right)^{n-1}}{T} \tag{7}$$

where J_n represents the model parameters, n is the polynomial order and T stands for thermodynamic temperature.

The values of model parameters given in Eqs. (3), (6) and (7) were obtained by minimizing objective function, OF, as follows:

$$OF = \sum_N \left(Y_{\mathrm{exp},j} - Y_{\mathrm{calc},j}\right)^2 = \min \tag{8}$$

$Y_{\mathrm{exp,j}}$ and $Y_{\mathrm{calc,j}}$ are experimental and computed values of the excess molar volume, viscosity difference and viscosity, respectively, and N is the number of experimental points.

Standard residual deviations of experimental data, σ_Y, were calculated as follows:

$$\sigma_Y = \left(\sum_N \frac{\left(Y_{\mathrm{exp},j} - Y_{\mathrm{calc},j}\right)^2}{N - n}\right)^{1/2} \tag{9}$$

Experimental

Both ionic liquids used in this study were purchased from Iolitec, USA. De-ionized water was used for the aqueous solutions preparation. Absolute ethanol (purity above 99.9 %) was supplied by Slavus, Slovakia. Basic data of these chemicals are collected in Table 1.

Samples of supplied ionic liquids were purified using a laboratory film evaporator MO 15 (Agrokombinát Lehnice, Slovakia). After purification at the pressure of 1.4—1.8 kPa and temperature of 150—170 °C, the content of water in [bmim]Ac and [bmim]DCA ILs decreased to 0.1835 mass % and 0.0595 mass %, respectively (Graczová et al., 2020). Water content in purified IL samples was estimated using a Karl Fischer titrator (Mettler Toledo DL53).

Binary mixtures were prepared by precisely weighing individual mixture components using a Mettler AE 200 analytical balance. Accuracy of the mass reading was $\pm 1 \times 10^{-4}$ g.

Tab. 1. Basic data of studied chemicals.

Component	CAS	M/(kg·mol^{-1})	Declared purity
[bmim]Ac	284049-75-8	0.19826	> 98 mass %
[bmim]DCA	448245-52-1	0.20526	> 99 mass %
water	7732-18-5	0.01802	de-ionized
ethanol	64-17-5	0.04607	> 99.9 mass %

Density of samples containing selected ionic liquids at ambient pressure was measured using an Anton Paar Densimeter DMA 5000. Declared standard uncertainty of density measurements using this equipment was $\pm 2 \times 10^{-2}$ kg·m^{-3}. Densities of the prepared binary mixtures were determined at 20 °C, 40 °C and 60 °C. Accuracy of the temperature reading was $\pm 1 \times 10^{-3}$ °C.

Estimation of transport properties of the samples was carried out using a Malvern Kinexus parallel plate rheometer. Viscosities of the prepared binary mixtures were determined at 20 °C, 40 °C and 60 °C. Accuracy of the temperature reading was $\pm 1 \times 10^{-2}$ °C.

Results and Discussion

Measured densities and viscosities of pure components at chosen temperatures are summarized in Tables 2 and 3, respectively. For comparison literature data are also included.

Results of the excess molar volume and partial molar volume calculation for the four binary systems [bmim]Ac (1)—water (2), [bmim]DCA (1)—water (2), [bmim]Ac (1)—ethanol (2) and [bmim]DCA (1)—ethanol (2) are given in Tables 4—7, respectively.

Optimum values of the Redlich-Kister equation parameters used for the experimental excess molar

Tab. 2. Experimental and literature densities of components at chosen temperatures.

Component	Density, ρ/(kg·m^{-3})						Source
	experimental			literature			
	20 °C	40 °C	60 °C	20 °C	40 °C	60 °C	
[bmim]Ac	1054.48	1042.26	1030.49	1054.3	1042.0	1029.9	Harris, 2020
[bmim]DCA	1063.30	1050.60	1038.16	1063.4	1050.6	1038.2	Almeida et al., 2016
water	998.22	–	–	998.22	991.29	973.05	NIST database
ethanol	789.59	772.22	754.14	789.45	772.44	754.30	NIST database

Tab. 3. Experimental and literature viscosities of components at chosen temperatures.

Component	Dynamic viscosity, η/(mPa·s)						Source
	experimental			literature			
	20 °C	40 °C	60 °C	20 °C	40 °C	60 °C	
[bmim]Ac	418.09	110.45	42.19	562.4	136.6	48.77	Harris, 2020
[bmim]DCA	35.04	16.83	9.65	36.83	17.86	10.38	Almeida et al., 2016
water	1.001	–	–	1.002	0.653	0.466	NIST database
ethanol	1.139	–	–	1.144	0.794	0.570	NIST database

Tab. 4. Excess molar volume of the binary system [bmim]Ac (1)—water (2) and component partial molar volumes at 20 °C, 40 °C and 60 °C.

Sample	Composition		V^E/(cm^3·mol^{-1})			$\bar{V}_1$/(cm^3·mol^{-1})			$\bar{V}_2$/(cm^3·mol^{-1})		
	x_1	x_2	20 °C	40 °C	60 °C	20 °C	40 °C	60 °C	20 °C	40 °C	60 °C
1	0.0808	0.9192	–0.9117	–0.7800	–0.6743	181.30	184.10	186.82	16.58	17.23	17.86
2	0.2044	0.7956	–1.3560	–1.2376	–1.1359	184.39	186.53	188.71	15.92	16.66	17.35
3	0.2864	0.7136	–1.5083	–1.4274	–1.3562	186.20	188.16	190.21	15.69	16.31	16.88
4	0.3662	0.6338	–1.5038	–1.4526	–1.4046	187.00	188.98	191.03	15.66	16.13	16.59
5	0.4230	0.5770	–1.4204	–1.3967	–1.3720	187.53	189.57	191.67	15.66	16.00	16.36
6	0.5255	0.4745	–1.2379	–1.2457	–1.2451	187.91	190.03	192.16	15.69	15.90	16.18
7	0.5970	0.4030	–0.9493	–0.9666	–1.0088	188.13	190.31	192.46	15.73	15.85	16.07
8	0.6733	0.3267	–0.7279	–0.7642	–0.8062	188.20	190.41	192.57	15.80	15.88	16.04
9	0.7439	0.2561	–0.5015	–0.5251	–0.5674	188.20	190.41	192.58	15.91	15.98	16.07

Tab. 5. Excess molar volume of the binary system [bmim]DCA (1)—water (2) and component partial molar volumes at 20 °C, 40 °C and 60 °C.

Sample	Composition		V^E/(cm³·mol⁻¹)			$\bar{V}_1$/(cm³·mol⁻¹)			$\bar{V}_2$/(cm³·mol⁻¹)		
	x_1	x_2	20 °C	40 °C	60 °C	20 °C	40 °C	60 °C	20 °C	40 °C	60 °C
1	0.0962	0.9038	0.0336	0.1536	0.2584	193.34	196.40	199.36	17.99	18.47	18.98
2	0.1968	0.8032	0.0723	0.2210	0.3521	193.34	195.87	198.37	17.98	18.50	19.10
3	0.2977	0.7023	0.1079	0.2517	0.3796	193.29	195.65	198.00	18.02	18.40	18.98
4	0.3774	0.6226	0.1296	0.2608	0.3777	193.25	195.58	197.91	18.06	18.30	18.87
5	0.4598	0.5402	0.1484	0.2633	0.3668	193.19	195.54	197.87	18.11	18.22	18.80
6	0.5387	0.4613	0.1546	0.2540	0.3445	193.15	195.49	197.82	18.18	18.17	18.80
7	0.6158	0.3842	0.1577	0.2414	0.3181	193.11	195.44	197.76	18.25	18.15	18.87
8	0.6976	0.3024	0.1499	0.2174	0.2811	193.07	195.38	197.69	18.35	18.15	18.99

Tab. 6. Excess molar volume of the binary system [bmim]Ac (1)—ethanol (2) and component partial molar volumes at 20 °C, 40 °C and 60 °C.

Sample	Composition		V^E/(cm³·mol⁻¹)			$\bar{V}_1$/(cm³·mol⁻¹)			$\bar{V}_2$/(cm³·mol⁻¹)		
	x_1	x_2	20 °C	40 °C	60 °C	20 °C	40 °C	60 °C	20 °C	40 °C	60 °C
1	0.0999	0.9001	−0.6905	−0.8106	−1.0047	184.23	185.69	186.77	56.07	57.05	57.94
2	0.2002	0.7998	−0.8131	−0.9677	−1.2045	186.98	188.90	190.74	55.88	56.80	57.59
3	0.2991	0.7009	−0.7933	−0.9523	−1.1917	187.72	189.83	191.94	56.46	57.41	58.30
4	0.3787	0.6213	−0.7620	−0.9173	−1.1462	187.81	189.95	192.11	56.93	57.94	58.95
5	0.4598	0.5402	−0.6860	−0.8311	−1.0415	187.83	189.98	192.14	57.20	58.27	59.37
6	0.5300	0.4700	−0.6089	−0.7438	−0.9357	187.93	190.07	192.22	57.25	58.34	59.48
7	0.6105	0.3895	−0.4905	−0.6126	−0.7799	188.12	190.26	192.42	57.16	58.25	59.38
8	0.6893	0.3107	−0.3780	−0.4901	−0.6338	188.31	190.46	192.65	57.10	58.15	59.24
9	0.7580	0.2420	−0.2202	−0.3271	−0.4568	188.41	190.58	192.79	57.25	58.23	59.26

Tab. 7. Excess molar volume of the binary system [bmim]DCA (1)—ethanol (2) and component partial molar volumes at 20 °C, 40 °C and 60 °C.

Sample	Composition		V^E/(cm³·mol⁻¹)			$\bar{V}_1$/(cm³·mol⁻¹)			$\bar{V}_2$/(cm³·mol⁻¹)		
	x_1	x_2	20 °C	40 °C	60 °C	20 °C	40 °C	60 °C	20 °C	40 °C	60 °C
1	0.0999	0.9001	−0.7147	−0.8060	−0.9690	188.44	190.12	191.43	56.59	57.70	58.73
2	0.1999	0.8001	−0.9297	−1.0623	−1.2737	191.17	193.17	195.09	56.18	57.22	58.16
3	0.2999	0.7001	−0.9919	−1.1379	−1.3609	192.30	194.47	196.64	56.38	57.43	58.42
4	0.3799	0.6201	−0.9351	−1.0778	−1.2919	192.63	194.87	197.11	56.67	57.73	58.79
5	0.4599	0.5401	−0.8643	−0.9983	−1.1967	192.75	195.03	197.30	56.91	57.98	59.09
6	0.5399	0.4601	−0.7660	−0.8863	−1.0628	192.81	195.11	197.40	57.03	58.11	59.24
7	0.6199	0.3801	−0.6531	−0.7564	−0.9068	192.88	195.19	197.50	57.02	58.09	59.21
8	0.6999	0.3001	−0.5618	−0.6465	−0.7695	192.96	195.28	197.62	56.91	57.97	59.07
9	0.7699	0.2301	−0.4342	−0.5002	−0.5953	193.02	195.35	197.71	56.79	57.84	58.92

volume data correlation are collected in Table 8. For all binaries, the polynomial order $n = 4$ was chosen when fitting the experimental excess molar volume data. In Table 8, also the values of standard residual deviations are included for each temperature considered.

In Figs. 1—4, variation of excess molar volume and excess partial molar volume of individual components vs. mixture composition is presented for the four chosen binary systems [bmim]Ac (1)—water (2), [bmim]DCA (1)—water (2), [bmim]Ac (1)—ethanol (2) and [bmim]DCA (1)—ethanol (2), respectively.

Tab. 8. Summary of excess molar volume correlation: optimum values of the 4th order Redlich-Kister model parameters and computed standard residual deviations.

Parameter	t/°C	Binary system			
		[bmim]Ac–H_2O	[bmim]DCA–H_2O	[bmim]Ac–EtOH	[bmim]DCA–EtOH
C_1	20	–5.1965	0.5873	–2.5619	–3.2508
	40	–5.1764	1.0128	–3.1109	–3.7604
	60	–5.1341	1.3966	–3.8984	–4.5076
C_2	20	4.2619	0.1953	1.8712	2.2216
	40	3.7574	–0.1648	2.1168	2.5610
	60	3.2671	–0.4707	2.5707	3.0560
C_3	20	–1.2705	–0.0082	–1.1302	–2.5380
	40	–0.3172	0.4307	–1.7937	–2.7773
	60	0.1388	0.8361	–2.6434	–3.2685
C_4	20	1.1405	0.0925	5.2082	2.1527
	40	0.4904	–0.5811	5.4482	2.3043
	60	–0.3272	–1.1345	6.1911	2.9074
σ_{V^E}/(cm^3 · mol^{-1})	20	0.0237	0.0010	0.0196	0.0163
	40	0.0213	0.0023	0.0226	0.0166
	60	0.0162	0.0039	0.0285	0.0195

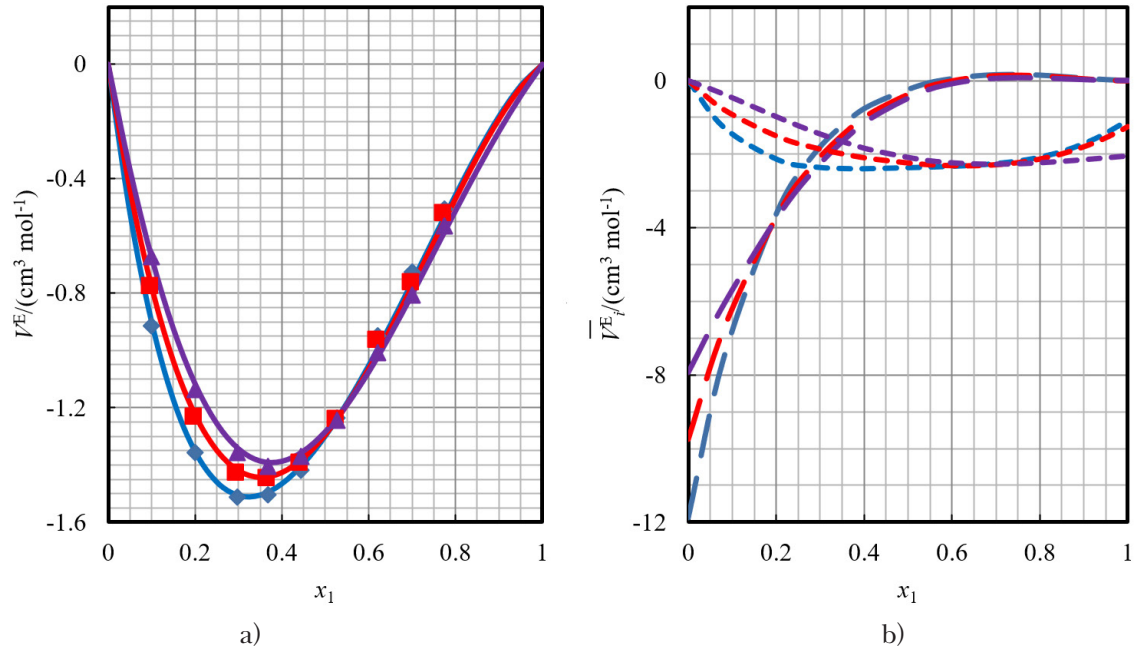

Fig. 1. Variation of a) excess molar volume of binary mixture [bmim]Ac (1)–water (2) and b) components excess partial molar volumes with mixture composition at 20 °C (blue color), 40 °C (red color) and 60 °C (violet color). Experimental (symbols) and calculated (curves) values; values for IL (dashed line) and water (dotted line).

Excess partial molar volumes of the respective components are defined as follows.

$$\overline{V}_i^{\mathrm{E}} = \overline{V}_i - V_i^* \tag{10}$$

Results of the viscosity difference calculation according to Eq. (5) are presented in Tables 9–12 for binaries [bmim]Ac (1)–water (2), [bmim]DCA (1)–water (2), [bmim]Ac (1)–ethanol (2) and [bmim] DCA (1)–ethanol (2), respectively.

Optimum values of the Redlich-Kister equation parameters used for the experimental viscosity difference data correlation are collected in Table 13. For all binary systems considered, the polynomial order n = 4 was chosen when fitting the experimental viscosity difference data. In Table 13, also the values of standard residual deviations are included separately for each temperature.

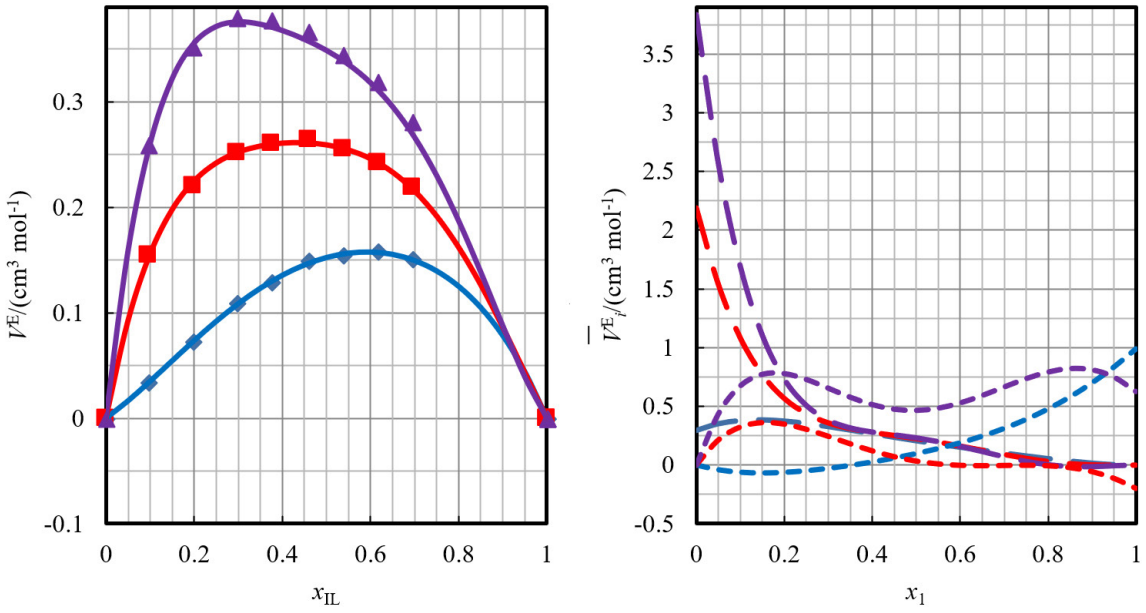

Fig. 2. Variation of a) excess molar volume of binary mixture [bmim]DCA (1)—water (2) and b) components excess partial molar volumes with mixture composition at 20 °C (blue color), 40 °C (red color) and 60 °C (violet color). Experimental (symbols) and calculated (curves) values; values for IL (dashed line) and water (dotted line).

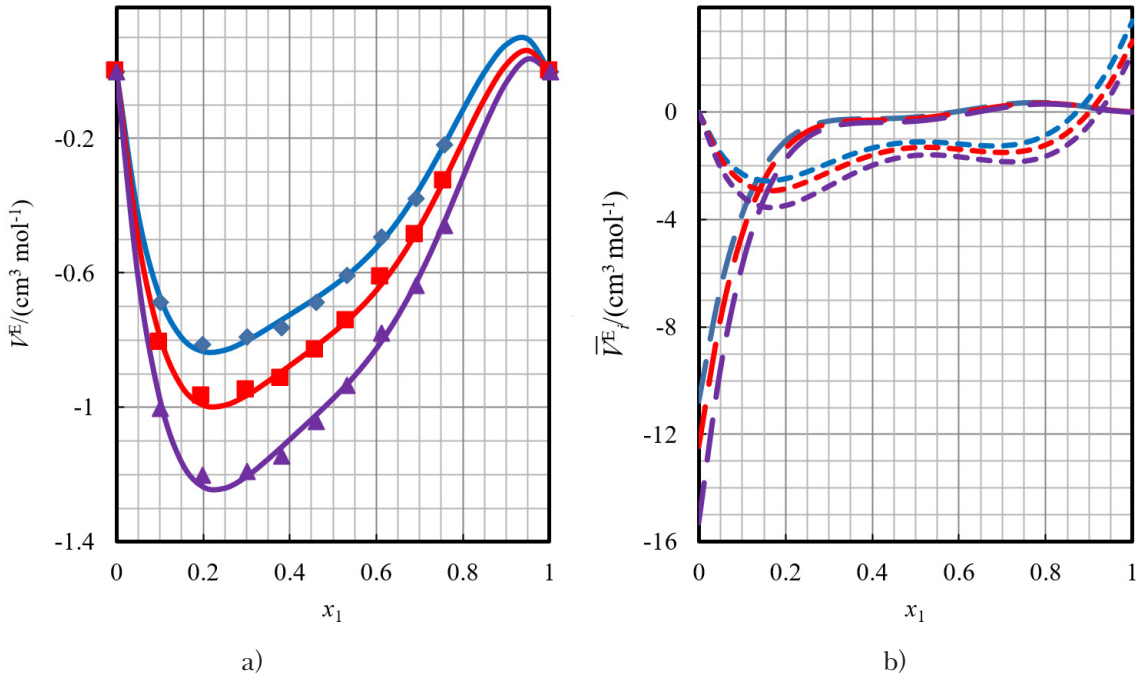

Fig. 3. Variation of a) excess molar volume of binary mixture [bmim]Ac (1)—ethanol (2) and b) components excess partial molar volumes with mixture composition at 20 °C (blue color), 40 °C (red color) and 60 °C (violet color). Experimental (symbols) and calculated (curves) values; values for IL (dashed line) and water (dotted line).

In Figs. 5—8, variation of viscosity difference with binary mixture composition is presented for the four chosen binary systems [bmim]Ac (1)—water (2), [bmim]DCA (1)—water (2), [bmim]Ac (1)—ethanol (2) and [bmim]DCA (1)—ethanol (2), respectively. In these figures, also experimental viscosity values and their fit according to the Jouyban-Acree model (Eq. (7)) are included.

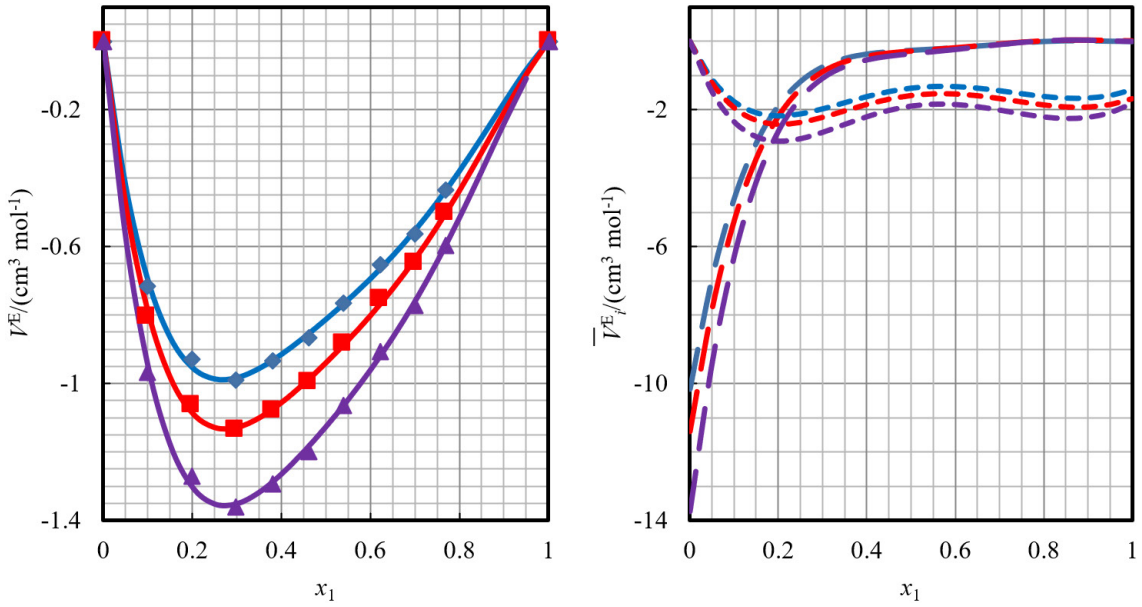

a) b)

Fig. 4. Variation of a) excess molar volume of binary mixture [bmim]DCA (1)—ethanol (2) and b) components excess partial molar volumes with mixture composition at 20 °C (blue color), 40 °C (red color) and 60 °C (violet color). Experimental (symbols) and calculated (curves) values; values for IL (dashed line) and water (dotted line).

Tab. 9. Calculated viscosity difference of binary system [bmim]Ac (1)—water (2) at 20 °C, 40 °C and 60 °C.

Sample	Composition		$\Delta\eta$/(Pa·s)		
	x_1	x_2	20 °C	40 °C	60 °C
1	0.0996	0.9004	–0.04642	–0.00922	–0.00242
2	0.1981	0.8019	–0.08070	–0.01508	–0.00370
3	0.2969	0.7031	–0.10687	–0.01861	–0.00418
4	0.3680	0.6320	–0.11233	–0.01779	–0.00341
5	0.4410	0.5590	–0.11855	–0.01787	–0.00330
6	0.5255	0.4745	–0.12014	–0.01732	–0.00307
7	0.6198	0.3802	–0.07136	–0.00551	0.00102
8	0.7007	0.2993	–0.08512	–0.00909	–0.00054
9	0.7755	0.2245	–0.01842	0.00255	0.00228

Tab. 10. Calculated viscosity difference of binary system [bmim]DCA (1)—water (2) at 20 °C, 40 °C and 60 °C.

Sample	Composition		$\Delta\eta$/(Pa·s)		
	x_1	x_2	20 °C	40 °C	60 °C
1	0.0962	0.9038	–0.0007	–0.0001	0.0000
2	0.1968	0.8032	–0.0008	–0.0001	0.0001
3	0.2977	0.7023	0.0005	0.0008	0.0003
4	0.3774	0.6226	–0.0007	0.0004	0.0003
5	0.4598	0.5402	–0.0012	–0.0001	0.0004
6	0.5387	0.4613	–0.0022	–0.0005	0.0001
7	0.6158	0.3842	–0.0028	–0.0005	0.0001
8	0.6976	0.3024	–0.0040	–0.0011	–0.0003

Tab. 11. Calculated viscosity difference of binary system [bmim]Ac (1)—ethanol (2) at 20 °C, 40 °C and 60 °C.

Sample	Composition		$\Delta\eta$/(Pa·s)		
	x_1	x_2	20 °C	40 °C	60 °C
1	0.0999	0.9001	–0.0541	–0.0122	–0.0038
2	0.2002	0.7998	–0.1071	–0.0238	–0.0073
3	0.2991	0.7009	–0.1567	–0.0342	–0.0102
4	0.3787	0.6213	–0.1927	–0.0409	–0.0118
5	0.4598	0.5402	–0.2237	–0.0463	–0.0131
6	0.5300	0.4700	–0.2430	–0.0487	–0.0133
7	0.6105	0.3895	–0.2545	–0.0490	–0.0130
8	0.6893	0.3107	–0.2490	–0.0458	–0.0117
9	0.7580	0.2420	–0.2273	–0.0401	–0.0098

Tab. 12. Calculated viscosity difference of binary system [bmim]DCA (1)—ethanol (2) at 20 °C, 40 °C and 60 °C.

Sample	Composition		$\Delta\eta$/(Pa·s)		
	x_1	x_2	20 °C	40 °C	60 °C
1	0.0999	0.9001	–0.0025	–0.0009	–0.0004
2	0.1999	0.8001	–0.0047	–0.0017	–0.0007
3	0.2999	0.7001	–0.0062	–0.0021	–0.0007
4	0.3799	0.6201	–0.0072	–0.0024	–0.0007
5	0.4599	0.5401	–0.0080	–0.0027	–0.0009
6	0.5399	0.4601	–0.0083	–0.0027	–0.0009
7	0.6199	0.3801	–0.0082	–0.0026	–0.0009
8	0.6999	0.3001	–0.0077	–0.0024	–0.0008
9	0.7699	0.2301	–0.0066	–0.0021	–0.0007

Tab. 13. Summary of viscosity difference correlation: optimum values of the 4th order Redlich-Kister model parameters and computed standard residual deviations.

Parameter	t/°C	Binary system			
		[bmim]Ac—H_2O	[bmim]DCA—H_2O	[bmim]Ac—EtOH	[bmim]DCA—EtOH
C_1	20	–0.4657	–0.0069	–0.9444	–0.0331
	40	–0.0650	–0.0008	–0.1918	–0.0110
	60	–0.0101	0.0010	–0.0533	–0.0037
C_2	20	0.1948	–0.0279	–0.5430	–0.0088
	40	0.0722	–0.0121	–0.0687	0.0002
	60	0.0272	–0.0019	–0.0088	0.0002
C_3	20	0.4380	–0.0117	–0.0965	0.0028
	40	0.0697	–0.0015	0.0198	0.0015
	60	0.0143	–0.0046	0.0116	0.0002
C_4	20	0.3769	0.0355	0.0645	0.0045
	40	0.0524	0.0209	0.0237	0.0038
	60	0.0086	–0.0020	0.0071	0.0003
$\sigma_{\Delta\eta}$/(Pa · s)	20	0.0151	0.0005	0.0005	0.0002
	40	0.0032	0.0003	0.0001	0.0002
	60	0.0011	0.0001	0.0001	0.0001

Optimum values of the Jouyban-Acree model parameters used for experimental viscosity data correlation are collected in Table 14. For all binary systems considered, the polynomial order $n = 4$ was chosen when fitting the experimental viscosity data. In Table 14, also the values of standard residual deviations are included.

Conclusions

Volumetric and transport properties of four binary mixtures containing [bmim]Ac and [bmim]DCA were measured at temperatures of 20 °C, 40 °C and 60 °C, and within the entire concentration range. Based on the experimental density values, excess

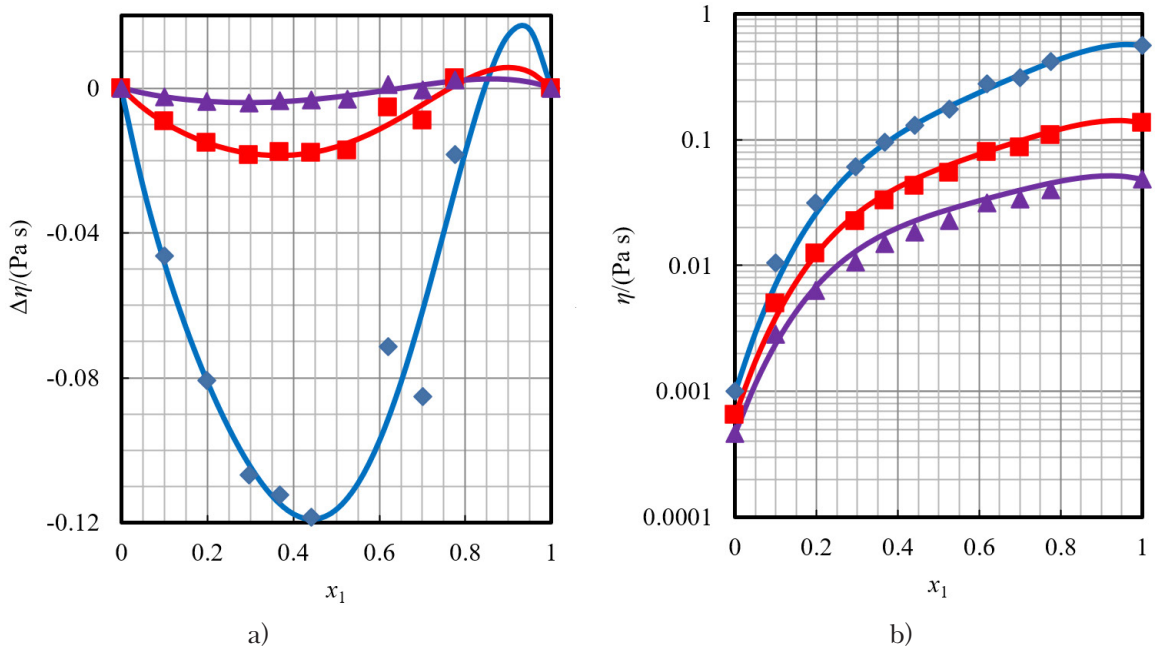

Fig. 5. Variation of a) viscosity difference of binary mixture [bmim]Ac (1)—water (2) and b) viscosity change with mixture composition at 20 °C (blue color), 40 °C (red color) and 60 °C (violet color). Experimental (symbols) and calculated (curves) values.

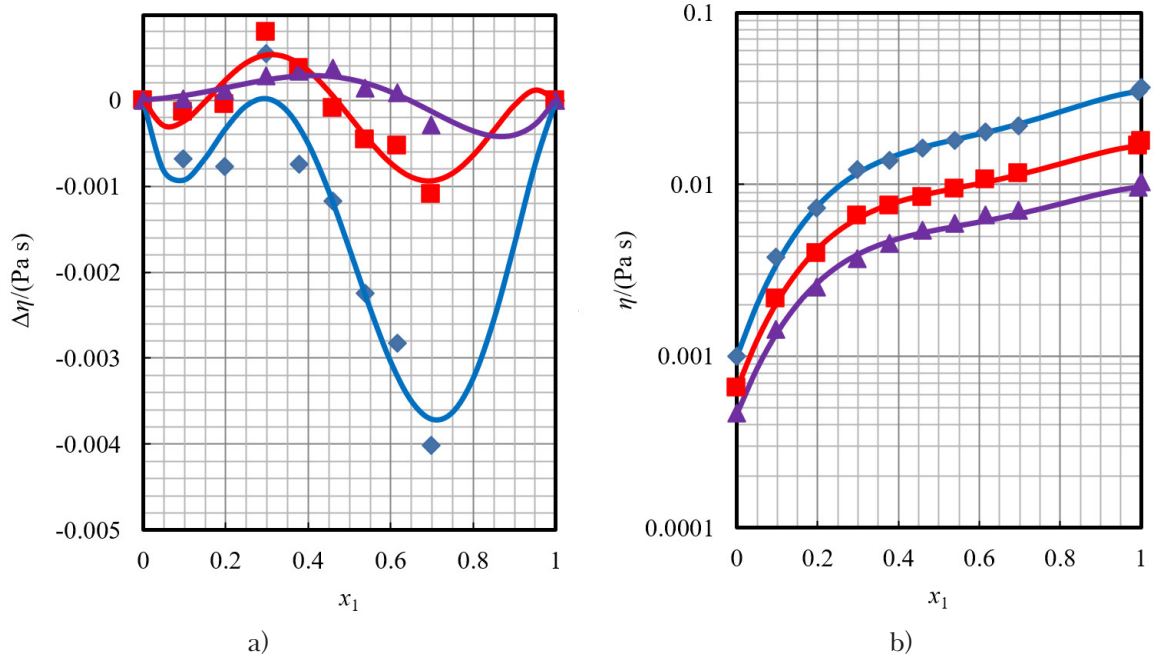

Fig. 6. Variation of a) viscosity difference of binary mixture [bmim]DCA (1)—water (2) and b) viscosity change with mixture composition at 20 °C (blue color), 40 °C (red color) and 60 °C (violet color). Experimental (symbols) and calculated (curves) values.

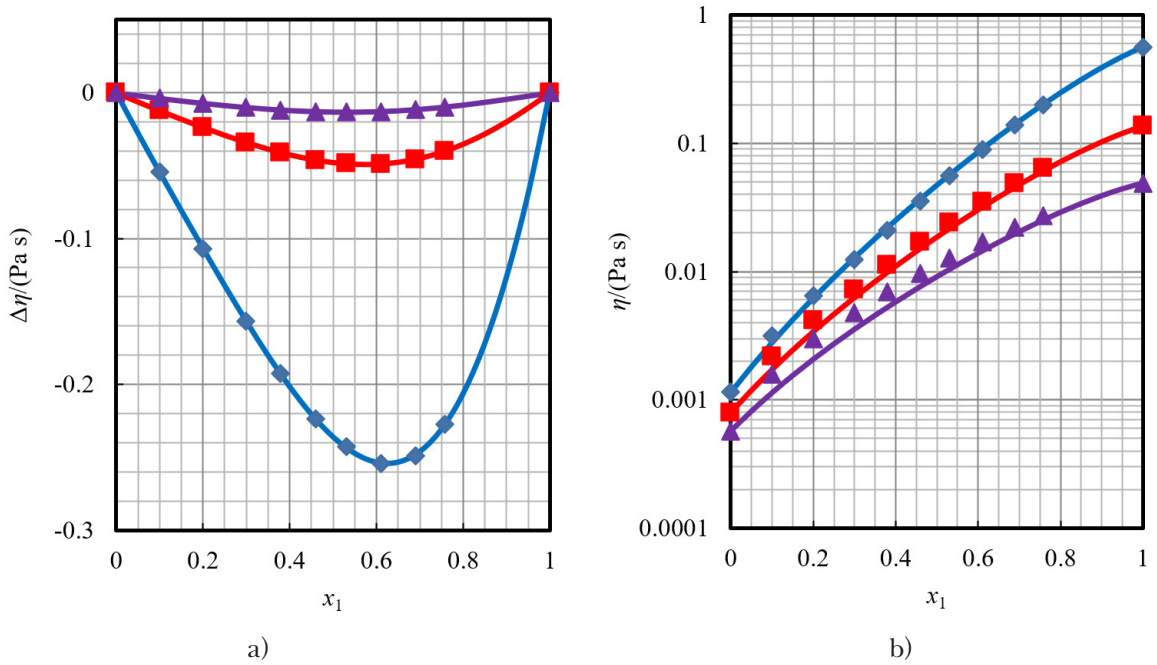

Fig. 7. Variation of a) viscosity difference of binary mixture [bmim]Ac (1)—ethanol (2) and b) viscosity change with mixture composition at 20 °C (blue color), 40 °C (red color) and 60 °C (violet color). Experimental (symbols) and calculated (curves) values.

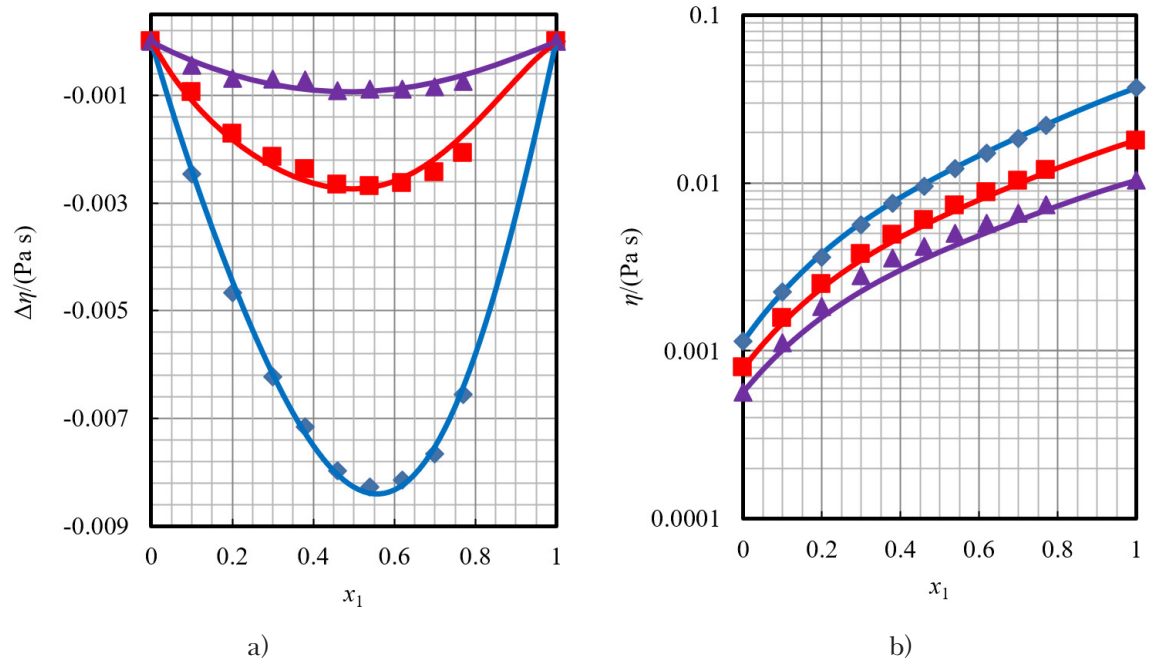

Fig. 8. Variation of a) viscosity difference of binary mixture [bmim]DCA (1)—ethanol (2) and b) viscosity change with mixture composition at 20 °C (blue color), 40 °C (red color) and 60 °C (violet color). Experimental (symbols) and calculated (curves) values.

molar volume and component partial molar volume data were computed. Their variation with mixture composition was correlated using the fourth-order Redlich-Kister equation. Compared to the behavior of other binary systems studied, positive values of excess molar volume were observed in case of [bmim]DCA—water. Also, the variation of viscosity difference with mixture composition showed quite complex behavior.

Slightly worse goodness of fit of excess molar volume correlation was observed in case of binaries comprising [bmim]Ac ionic liquid. Average stand-

Tab. 14. Summary of viscosity difference correlation: optimum values of the three-parameters Jouyban-Acree model and computed standard residual deviations

Parameter	Binary system			
	[bmim]Ac–H_2O	[bmim]DCA–H_2O	[bmim]Ac–EtOH	[bmim]DCA–EtOH
J_1	2281.70	1260.10	723.70	626.53
J_2	–1509.04	–1332.52	–53.81	–370.80
J_3	1345.03	907.18	188.57	202.55
σ_η/(Pa·s)	0.0112	0.0003	0.0038	0.0010

ard deviation of the excess molar volume oscillated around the value of 0.02 $cm^3 \cdot mol^{-1}$. The same trend was observed when fitting the viscosity difference with an average standard deviation of around 0.3 mPa·s. Only in case of the binary [bmim]Ac–water, the standard deviation value was by one order of magnitude higher. Better fit of experimental viscosity data using the Jouyban-Acree model were achieved for binaries containing [bmim]DCA ionic liquid.

This study was presented at the 47th International Conference of the Slovak Society of Chemical Engineering (May 18–19, 2021, Online, Bratislava, Slovakia).

Acknowledgement
This work was supported by the Slovak Research and Development Agency under the contract No. APVV-0232-18.

References

Acree WE Jr. (1992) Thermochim. Acta 198: 71–79.
Almeida HFD, Canongia Lopes JN, Rebelo LPN, Coutinho JAP, Freire MG, Marrucho IM (2016) J. Chem. Eng. Data 61: 2828–2843.
Armand M, Endres F, MacFarlane DR, Ohno H, Scrosati B (2009) Nat. Mater. 8: 621–629.
Bajić DM, Šerbanović SP, Živković EM, Jovanović J, Kijevčanin ML (2014) J. Mol. Liq. 197: 1–6.
Galán Sánchez LM, Meindersma GW, de Haan AB (2007) Chem. Eng. Res. Des. 85: 31–39.
Graczová E, Steltenpohl P (2015) Chem. Eng. Trans. 45: 1957–1962.
Graczová E, Šulgan B, Steltenpohl P (2020) Sep. Purif. Technol. 251: 116968.
Greaves TL, Drummond CJ (2008) Chem. Rev. 108: 206–237.
Harris KR (2020) J. Chem. Eng. Data 65: 804–813.
Jacquemin J, Ge R, Nancarrow P, Rooney DW, Costa Gomes MF, Pádua AAH, Hardacre C (2008) J. Chem. Eng. Data 53: 716–726.
Meindersma GW, Hansmeier AR, de Haan AB (2010) Ind. Eng. Chem. Res. 49: 7530–7540.
Nieto de Castro CA, Langa E, Morais AL, Matos Lopes ML, Lourenço MJV, Santos FJV, Santos MSCS, Canongia Lopes JN, Veiga HIM, Macatrão M, Esperança JMSS, Marques CS, Rebelo LPN, Afonso CAM (2010) Fluid Phase Equilib. 294: 157–179.
Perreiro AB, Araújo JMM, Esperança JMMS, Marrucho IM, Rebelo LPN (2012) J. Chem. Thermodyn. 46: 2–28.
Redlich O, Kister AT (1948) Ind. Eng. Chem. 40: 345–348.
Welton T (1999) Chem. Rev. 99: 2071–2084.
Wood SE, Battino R (1990) Thermodynamics of Chemical Systems. Cambridge University Press, Cambridge, UK.
Zeng SJ, Gao HS, Zhang XC, Dong HF, Zhang XP, Zhang SJ (2014) Chem. Eng. J. 251: 248–256.

sciendo

Thermochemistry of antioxidant action of isoflavones and their deprotonated forms in aqueous solution: hydrogen or electron transfer?

Monika Biela, Andrea Kleinová, Erik Klein

Institute of Physical Chemistry and Chemical Physics, Slovak University of Technology in Bratislava, Radlinského 9, SK-812 37 Bratislava, Slovakia
monika.biela@stuba.sk

Abstract: Isoflavones possessing several weak acidic hydroxyl groups can undergo successive deprotonations in aqueous solutions. Therefore, their antioxidant properties cannot be ascribed only to the neutral forms but also to corresponding phenoxide anions. It was already confirmed that isoflavones prefer the formation of dianions in aqueous solution. For eight isoflavones and their preferred (poly)deprotonated forms, thermochemistry of hydrogen atom transfer and electron abstraction was studied in terms of corresponding reaction enthalpies, i.e., O—H bond dissociation enthalpies and ionization potentials. Our results clearly indicate that the increase in negative charge causes significant drop in ionization potential and bond dissociation enthalpy. On the other hand, proton affinities show the opposite trend. Thus, it is unfeasible to find a generally valid trend for dianions – corresponding reaction enthalpies strongly depend on the structure of isoflavone, especially on the number/positions of OH groups.

Keywords: Bond dissociation enthalpy, Consecutive deprotonations, Electron transfer, Phenoxide anion

Introduction

Isoflavonoids represent a sub-group of approximately 2000 flavonoids present almost exclusively in plants from the *Leguminosae* family (Veitch, 2007). Among various biological effects, these polyphenols also show antioxidant activity (Alseekh et al., 2020; Procházková et al., 2011). Flavonoids in narrow sense have B ring connected to C2 carbon atom at ring C. In contrast to flavonoids, π-conjugation in isoflavonoids is disrupted over the entire skeleton, because B ring attached to C3 atom is considerably twisted out of plane of rings A and C (Caicedo et al., 2014; Han et al., 2009). Isoflavonoids possessing C4=O keto group at C ring, Fig. 1, are called isoflavones.

In aqueous solutions, two mechanisms of the primary antioxidant, i.e., radical scavenging, effect of polyphenolic compounds, are of importance: Hydrogen Atom Transfer (HAT) and Sequential Proton-Loss Electron-Transfer (SPLET), where deprotonation of the OH group precedes the electron transfer from the formed phenoxide anion (Caicedo et al., 2014; Lengyel et al., 2013; Zheng et al., 2019). In general, antioxidant effect of polyphenols is increasing with pH (Amorati et al., 2018; Altunkaya et al., 2016). Due to weak acidities of phenolic OH groups, higher relative abundance of deprotonated species with increasing pH is directly responsible for the observed enhanced radical scavenging activity. Therefore, in this work, O—H bond dissociation enthalpies (BDE) and ionization potentials (IP) were investigated, representing the reaction enthalpies of HAT and electron transfer from eight isoflavones depicted in Fig. 1 and their anions.

The main aim was to find the trends in reaction enthalpies upon the consecutive deprotonations of isoflavones in aqueous solutions, see reaction scheme in Fig. 2. Also the selection of isoflavones enables to elucidate the effect of studied isoflavones structure on the thermodynamics of HAT and electron transfer.

Computational details

Gaussian 09 program package (Frisch et al., 2013) was employed for computations. Geometries of molecules, radicals, and ions were optimized using B3LYP (Becke, 1993; Lee et al., 1988) functional without any constraints (energy cut-off of 10^{-5} kJ·mol^{-1}, final RMS energy gradient under 0.01 kJ·mol^{-1}·Å^{-1}). Calculations were performed using the 6-311++G(d,p)* basis set (Hariharan and Pople, 1973; Rassolov et al., 1998). Optimized structures were confirmed by vibration analysis to be real minima. Solvent effect on the total enthalpies was described by the integral equation formalism polarized continuum model IEF-PCM method (Cances et al., 1997; Cances and Mennucci, 1998). The same computational approach was used in our previous works on naturally occurring (poly)phenolic compounds (Biela et al., 2020 and 2022; Lengyel et al., 2013; Škorňa et al., 2016a, 2016b; Vagánek et al.,

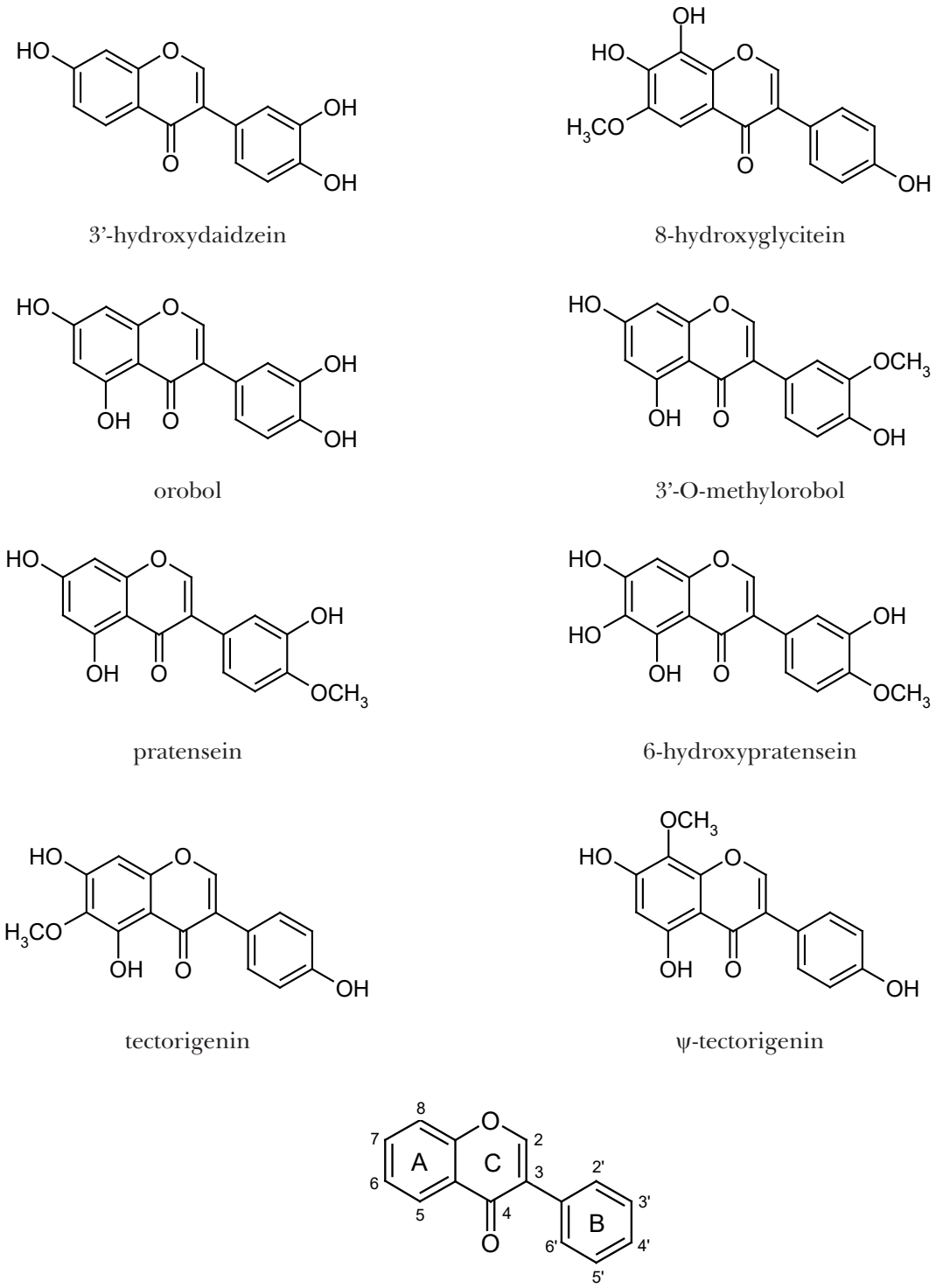

Fig. 1. Studied isoflavones and carbon atoms numbering scheme of isoflavones.

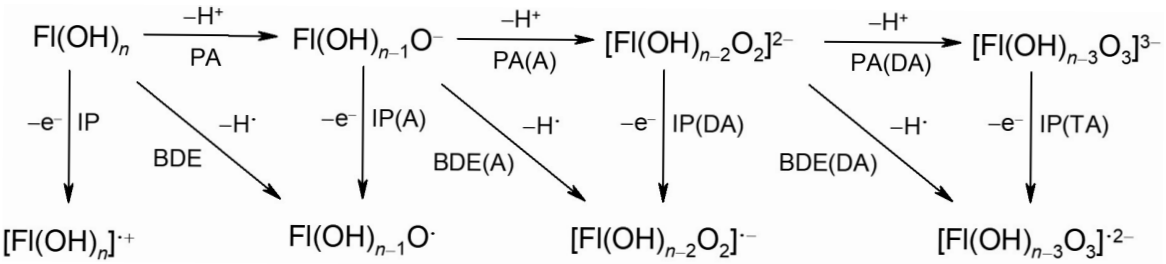

Fig. 2. Studied processes and denotation used for individual reaction enthalpies.

2014). In these papers, applicability and reliability of the chosen methodology has been proved.

From the calculated total enthalpies at 298.15 K, O—H bond dissociation enthalpies, BDE, and ionization potentials, IP, were determined for parent, non-dissociated isoflavones, $Fl(OH)_n$, monoanions, $Fl(OH)_{n-1}O^-$, dianions, $[Fl(OH)_{n-2}O_2]^{2-}$, and trianions, $[Fl(OH)_{n-3}O_3]^{3-}$

$$BDE = H(Fl(OH)_{n-1}O^{\bullet}) + H(H^{\bullet}) - H(Fl(OH)_n) \quad (1)$$

$$BDE(A) = H([Fl(OH)_{n-2}O_2]^{\bullet -}) + H(H^{\bullet}) - H(Fl(OH)_{n-1}O^-) \quad (2)$$

$$BDE(DA) = H([Fl(OH)_{n-3}O_3]^{\bullet 2-}) + H(H^{\bullet}) - H([Fl(OH)_{n-2}O_2]^{2-}) \quad (3)$$

$$BDE(TA) = H([Fl(OH)_{n-4}O_4]^{\bullet 3-}) + H(H^{\bullet}) - H([Fl(OH)_{n-3}O_3]^{3-}) \quad (4)$$

$$IP = H([Fl(OH)_nO]^{\bullet +}) + H(e^-) - H(Fl(OH)_n) \quad (5)$$

$$IP(A) = H(Fl(OH)_{n-1}O^{\bullet}) + H(e^-) - H(Fl(OH)_{n-1}O^-) \quad (6)$$

$$IP(DA) = H([Fl(OH)_{n-2}O_2]^{\bullet -}) + H(e^-) - H([Fl(OH)_{n-2}O_2]^{2-}) \quad (7)$$

$$IP(TA) = H([Fl(OH)_{n-3}O_3]^{\bullet 2-}) + H(e^-) - H([Fl(OH)_{n-3}O_3]^{3-}) \quad (8)$$

Calculated total enthalpies of hydrogen atom, $H(H^{\bullet})$ = –1313.065 kJ · mol^{-1}, and electron, $H(e^-)$ = –101.855 kJ · mol^{-1}, in aqueous solutions were taken from Rimarčík et al. (2010).

Results and discussion

Hydrogen atom transfer

Our previous works (Biela et al. 2020 and 2022) were focused on the second proton loss from flavonoids, i.e., the formation of dianion (DA), and the consecutive electron transfer producing a radical anion. These processes represent two steps of the Sequential Proton-Loss Electron-Transfer (SPLET) mechanism for mono-deprotonated flavonoids. Considering the SPLET mechanism, enthalpy of electron transfer from phenoxide monoanion (see eq. 6) is usually denoted as Electron Transfer Enthalpy, ETE. On the other hand, the term ionization potential (IP) is exclusively used for the enthalpy of electron transfer from a parent molecule. To avoid the application of two different denotations for the same kind of process, only IP is employed throughout this report. In case of anionic species, the type of (poly)anion is specified in parentheses (Fig. 2). Bond dissociation enthalpies are distinguished in the same manner, i.e., BDE is used for the isoflavone molecule, BDE(A) for monoanion, BDE(DA) for dianion. As orobol and 6-hydroxypratensein possess four OH groups, also BDE(TA) values were calculated for the preferred trianions.

For the studied isoflavones, thermodynamically preferred anions for each successive deprotonation were identified. For non-dissociated isoflavones and mono-deprotonated species of 3'-hydroxydaidzein, orobol, 3'-O-methylorobol, pratensein, 6-hydroxypratensein, tectorigenin, and ψ-tectorigenin, proton affinities of OH groups of the parent molecule, PA, and possible monoanions, PA(A), from Biela et al. (2022), were applied. For orobol and 6-hydroxypratensein, PA(DA) values of the two remaining OH groups were calculated. Found values of 3'-OH PA(DA) = 284 kJ · mol^{-1} and 5-OH PA(DA) = 273 kJ · mol^{-1} for preferred 4',7-DA indicate that orobol favors the formation of 4',5,7-trianion. In case of 6-hydroxypratensein, 5-OH PA(DA) = 274 kJ · mol^{-1} and 6-OH PA(DA) = 269 kJ · mol^{-1} reveal slight preference of the 3',6,7-trianion formation. However, for the two isoflavones, differences between PA(DA) values are relatively small. For 8-hydroxyglycitein, we have found that first H^+ loss occurs from 7-OH, followed by the deprotonation of 4'-OH. Obtained 7-OH PA = 164 kJ · mol^{-1} and 4'-OH PA(A) = 208 kJ · mol^{-1} are in accordance with values calculated for other isoflavones in Biela et al. (2022) and Lengyel et al. (2013).

Calculated O—H bond dissociation enthalpies are compiled in Table 1. First column shows preferred (poly)anions for consecutively deprotonated molecules. Data in Table 1 show that BDE(A) values of deprotonated isoflavones are lower than BDEs of non-dissociated molecules. This trend is in accordance with Klein et al. (2016), where a decrease in O—H bond dissociation enthalpies for phenoxide anions of various flavonoids, including several isoflavones, was also observed. Caicedo et al. (2014) theoretically investigated five isoflavones in terms of reaction Gibbs free energies of HAT to $^{\bullet}OOH$ and $^{\bullet}OOCH_3$ radicals. For 6-hydroxydaidzein and 8-hydroxyglycitein, the authors found that the relative Gibbs free energies of HAT reactions involving dianions are slightly more exergonic than those of monoanions, and the latter are much more exergonic than those involving neutral species. This observation is in line with trends in Table 1, indicating the decrease in O—H bond dissociation enthalpies upon successive deprotonations of OH groups of isoflavones.

Lower BDEs were obtained for OH groups located at B ring. The lowest values were found for isoflavones possessing two OH groups, forming *ortho*-dihydroxy (catechol) structure of B ring (see data for orobol and 3'-hydroxydaidzein in Table 1). These groups participate in intramolecular hydrogen bond (IHB). Although the abstraction of $H^{\bullet}$ atom

Tab. 1. (IEF-PCM) B3LYP/6-311++G(d,p) O—H bond dissociation enthalpies, BDE, in kJ · mol^{-1} of studied isoflavones, and preferred anions (A), dianions (DA) and trianions (TA).

Isoflavone/Anion	3'-OH	4'-OH	5-OH	6-OH	7-OH	8-OH
3'-Hydroxydaidzein	310	304			357	
7-A	307	297				
4',7-DA	285					
8-Hydroxyglycitein		331			314	315
7-A		321				283
4',7-DA						280
Orobol	311	305	384		362	
7-A	308	298	372			
4',7-DA	286		363			
4',5,7-TA	281					
3'-O-Methylorobol		334	383		361	
7-A		328	372			
4',7-DA			362			
Pratensein	339		384		362	
7-A	336		373			
3',7-DA			372			
6-Hydroxypratensein	339		345	302	334	
7-A	336		332	297		
3',7-DA			333	295		
3',6,7-TA			259			
Tectorigenin		333	359		349	
7-A		324	343			
4',7-DA			344			
ψ-Tectorigenin		333	366		333	
7-A		322	351			
4',7-DA			348			

involved in IHB requires additional energy for its disruption, the emerging phenoxy radical is immediately stabilized by new IHB as the second OH group undergoes a rotation towards the reaction site. Two tectorigenins and 8-hydroxyglycitein with a single hydroxy group in B ring show 4'-OH BDEs higher by almost 30 kJ · mol^{-1}. Three isoflavones have guaiacol structure of B ring, i.e., OH and OCH_3 groups are attached to neighboring carbon atoms. Comparing pratensein and 3'-O-methylorobol, lower BDE was identified for 4'-OH group of 3'-O-methylorobol. Found 3'-OH BDEs of pratensein and 6-hydroxypratensein are higher by 5 kJ · mol^{-1}. BDEs of OH groups neighboring with OCH_3 in B ring are affected by IHB between the hydrogen atom of phenolic OH group and the oxygen atom of OCH_3, as well as by the electron-donating effect of the methoxy group placed in *ortho* position to the OH group. These two effects are partly compensated. Compared to the catechol structure of B ring, a roughly 30 kJ · mol^{-1} increase in O—H BDE was observed for the guaiacol moiety. Among the investigated isoflavones, the lowest BDE was found for 6-OH group of 6-hydroxypratensein with three OH groups at A ring. The presence of such pyrogallol structural motif leads to a large decrease in 5-OH and 7-OH BDEs in comparison to orobol and 3'-O-methylorobol lacking the 6-OH group. In general, highest BDEs were found for the 5-OH group forming IHB with C4=O group located at C ring. The decrease in 5-OH, as well as in 7-OH BDE of 6-hydroxypratensein and two tectorigenins, is caused by the presence of additional OCH_3 or OH substituent at A ring. For example, 5-OH BDE of pratensein is higher by ca 40 kJ · mol^{-1} in comparison to 6-hydroxypratensein and by 25 kJ · mol^{-1} in comparison to tectorigenin with 6-OCH_3 group. With exception of 8-hydroxyglycitein and 6-hydroxypratensein, the studied isoflavones prefer HAT from B ring. Due to the *ortho*-dihydroxy or pyrogallol structure of A ring, these two molecules prefer HAT from A ring.

Deprotonation of the 7-OH group has only a minute effect on the 3'-OH group. BDE(A) is lower

by 3 kJ · mol^{-1} than in isoflavones possessing this group in *meta* position to the B ring connection point, confirming the negligible effect of different structures of A ring on HAT from the 3'-OH group. On the other hand, impact of 7-OH deprotonation on 4'-OH is slightly higher, BDE(A) values are lower by 6—11 kJ · mol^{-1} than 4'-OH BDEs. As assumed, the largest (11—16 kJ · mol^{-1}) changes were identified in 5-OH BDE(A) *vs* BDE values.

For the preferred 4',7- or 3',7-dianions, a further decrease in bond dissociation enthalpies is observed. Only in case of 6-hydroxypratensein, pratensein, and tectorigenin, 5-OH BDE(DA) can be considered practically identical with 5-OH BDE(A). For isoflavones with catechol structure of B ring, the drop in 3'-OH BDE(DA) exceeds 20 kJ · mol^{-1} (see results for 3'-hydroxydaidzein and orobol). For other OH groups present in the studied dianions, differences between BDE(DA) and BDE(A) are within 10 kJ · mol^{-1} and the second deprotonation does not induce significant decrease in bond dissociation enthalpies.

Since two isoflavones possess four OH groups in their molecules, the effect of the third deprotonation on 3'-OH BDE(TA) of orobol and 5-OH BDE(TA) of 6-hydroxypratensein can be estimated. Results in Table 1 indicate significant, 74 kJ · mol^{-1}, drop in 5-OH BDE(TA) for thermodynamically favored 3',6,7-trianion of 6-hydroxypratensein in comparison to 5-OH BDE(DA), i.e., the second deprotonation in ring A leads to significant decrease in the enthalpy of the O—H bond dissociation. For the 3'-OH group of orobol, 5 kJ · mol^{-1} drop was found for the preferred 4',5,7-trianion. Thus, deprotonations of the two OH groups at A ring have only small effect on the O—H bond homolytic cleavage in B ring. Found BDE(TA) values indicate high tendency of the pyrogallol moiety to HAT at high pH values when two of three OH groups are already deprotonated.

Electron transfer

Reaction enthalpies of electron transfer from isoflavones and preferred anions are summarized in Table 2. At first glance, the increasing negative charge upon successive deprotonations induces significant drops in ionization potential. In aqueous solutions, electron transfer from non-dissociated flavonoids is usually not operative mechanism of the radical scavenging activity (Caicedo et al., 2014; DiMeo et al., 2013; Vagánek et al., 2014; Xue et al., 2018, Zheng et al., 2019).

Ionization potentials of the investigated isoflavones lie in the range from 449 kJ · mol^{-1} to 467 kJ · mol^{-1}. IPs of other eight isoflavones (daidzein, formononetin, genistein, biochanin A, prunetin, 6-hydroxydaidzein, glycitein, and santal), were found in a similar range, from 455 kJ · mol^{-1} to 468 kJ · mol^{-1} (Lengyel et al., 2013). This indicates that structural distinctions among various isoflavones do not play a considerable role in the electron transfer thermodynamics. An interesting fact is that tectorigenin possessing a methoxy group at the C6 carbon atom shows the highest IP, while ψ-tectorigenin with methoxy group at the C8 atom belongs to isoflavones with the lowest IPs. Reaction enthalpies of electron transfer from all possible monoanions, i.e., IP(A), are summarized in Biela et al. (2022) without further discussion. All IP(A) values for thermodynamically preferred 7-O$^-$ anions are considerably lower than IPs found for parent molecules. The IPs range of 40 kJ · mol^{-1} implies that electron transfer from preferred anions is more susceptible to structural changes than in non-dissociated molecules.

Tab. 2. (IEF-PCM) B3LYP/6-311++G(d,p) ionization potentials, IP, in kJ · mol^{-1}, of studied isoflavones and preferred 7-O$^-$ anions (A), dianions (DA), and trianions (TA).

Isoflavone	IP	IP(A)[a]	IP(DA)[a]	IP(TA)
3'-Hydroxydaidzein	458	383	311[b]	
8-Hydroxyglycitein	462	350	313[b]	
Orobol	459	390	313[b]	289[d]
3'-O-Methylorobol	449	389	310[b]	
Pratensein	451	390	314[c]	
6-Hydroxypratensein	449	375	314[c]	226[e]
Tectorigenin	467	370	317[b]	
ψ-Tectorigenin	449	357	316[b]	

[a]With exception of 8-hydroxyglycitein, data taken from Biela et al. (2022).

[b]Value for preferred 4',7-dianion.

[c]Value for preferred 3',7-dianion.

[d]Value for preferred 4',5,7-trianion.

[e]Value for preferred 3',6,7-trianion.

Lowest IP(A) values were identified for isoflavones possessing OCH_3 group in *ortho*-position to deprotonated 7-OH group, i.e., for 8-hydroxyglycitein and both tectorigenins. The range of IP(A) values of the remaining isoflavones is narrow (15 kJ · mol^{-1}). IP(DA) values of the favored 4',7- or 3',7-dianions, taken from Biela et al. (2022), lie again in a very narrow interval (7 kJ · mol^{-1}) and only a minute effect of the isoflavone structure on the thermodynamics of electron transfer from dianions can be observed. Very similar IP(DA) values of all isoflavones are due to one deprotonation occurring in A ring and one in B ring. Data in Table 2 also show that larger differences between IP and IP(A) are accompanied with lower differences in IP(A) and IP(DA). For example, IP(A) of 8-hydroxyglycitein is by 112 kJ · mol^{-1} lower than its IP, however, IP(A) is only by 37 kJ · mol^{-1} higher than IP(DA). On the other hand, 3'-O-methylorobol shows the lowest IP *vs* IP(A) difference but the highest IP(A) *vs* IP(DA) difference.

For favored trianions of orobol and 6-hydroxypratensein, further drop in the enthalpy of electron transfer was observed. In case of 3',6,7-trianion of 6-hydroxypratensein, the difference between IP(DA) and IP(TA) is exceptionally large (88 kJ · mol^{-1}) and indicates that electron transfer from this trianion is an important reaction pathway compared to HAT or deprotonation of the last OH group of 6-hydroxypratensein.

Thermodynamically preferred process

In the previous work (Biela et al., 2022), unambiguous thermodynamic preference of dianion formation in aqueous solutions was confirmed in isoflavones. This holds also for 8-hydroxyglycitein that was not included in the preceding report. However, in case of the studied dianions, thermodynamics of HAT, electron transfer or successive deprotonation do not indicate a general trend, see reaction enthalpies in Table 3.

Pratensein, 3'-O-methylorobol, tectorigenin, and ψ-tectorigenin prefer third (last) proton loss, because BDE(DA) and IP(DA) are significantly higher than PA(DA). Differences between IP(DA) and PA(DA) values identified for the four isoflavones exceed 35 kJ · mol^{-1}. Corresponding reaction enthalpies increase in the order: PA(DA) < IP(DA) < BDE(DA). For 6-hydroxypratensein, due to pyrogallol structure of A ring, the order is PA(DA) < BDE(DA) < IP(DA). BDE(DA) for 6-OH group is by 26 kJ · mol^{-1} higher than the corresponding PA(DA). For 3'-hydroxydaidzein, orobol, and 8-hydroxyglycitein, following the same order of the reaction enthalpies, PA(DA) and BDE(DA) reached similar values with differences from 0 (3'-hydroxydaidzein) to 13 kJ · mol^{-1} (8-hydroxyglycitein and orobol). Therefore, from the thermodynamics point of view, dianions of these molecules may undergo both processes: HAT and deprotonation. Favored process can also depend on the type of scavenged radical and the reaction kinetics of the processes (Caicedo et al., 2014; Mathew et al., 2015). Among the studied isoflavones, orobol and 6-hydroxypratensein have four OH groups in the molecule; therefore, reaction enthalpies of HAT, electron transfer, and deprotonation can be computed also for the preferred trianion. For orobol with catechol structure of B ring, and 5-OH and 7-OH groups at A ring, all three reaction enthalpies obtained for 4',5,7-trianion in Table 3 are within 10 kJ · mol^{-1}, i.e., there is no clear susceptibility to a certain process. On the contrary, 3',6,7-trianion of 6-hydroxypratensein favors electron transfer, because its IP(TA) is by 33 kJ · mol^{-1} lower than 5-OH BDE(TA) and

Tab. 3. (IEF-PCM) B3LYP/6-311++G(d,p) proton affinities, PA, bond dissociation enthalpies, BDE, and ionization potentials, IP, in kJ · mol^{-1}, of preferred dianions (DA), and trianions (TA).

Dianion	**PA(DA)**	**BDE(DA)**	**IP(DA)**
3'-Hydroxydaidzein	*285*	*285*	311
8-Hydroxyglycitein	*267*	280	313
Orobol	*273* (5-OH)	286 (3'-OH)	313
3'-O-Methylorobol	*273*	362	310
Pratensein	*272*	372	314
6-Hydroxypratensein	*269* (6-OH)	295 (6-OH)	314
Tectorigenin	*273*	344	317
ψ-Tectorigenin	*275*	348	316
Trianion	PA(TA)	BDE(TA)	IP(TA)
Orobol	291	*281*	289
6-Hydroxypratensein	335	259	*226*

by 109 kJ · mol^{-1} lower than 5-OH PA(TA), which indicates that three deprotonations in one ring are very improbable. These results are in accordance with the observations for consecutive deprotonations of OH groups of gallic acid (Škorňa et al., 2016b) and other polyphenolic compounds (Marković et al., 2013; Zheng et al., 2021).

Conclusions

For eight isoflavones, thermochemistry of the preferred (poly)anions in an aqueous solution was theoretically studied in terms of O—H bond dissociation enthalpies and ionization potentials. With the increasing negative charge, BDEs decrease. In general, low values were found for OH groups located at B ring with *ortho*-dihydroxy (catechol) structure. The lowest BDE was observed for 6-hydroxypratensein with three OH groups at A ring, forming pyrogallol structure. This implies that OH groups attached to neighboring carbon atoms play substantial role in primary antioxidant action.

The drop in ionization potentials with increasing negative charge after successive deprotonations of OH groups in isoflavones is even more significant. Average difference between IP and IP(A) is ca 80 kJ · mol^{-1}. Lowest IP(A) values were identified for isoflavones possessing OCH_3 group in *ortho*-position to the deprotonated 7-OH group. Differences between IP(A) *vs* IP(DA) and IP(DA) *vs* IP(TA) are not so significant with average differences of 62 kJ · mol^{-1} and 56 kJ · mol^{-1}, respectively.

While isoflavones in aqueous solutions show unambiguous thermodynamic preference of dianion formation, reaction enthalpies for consecutive processes do not show a general trend. Dianions of the investigated isoflavones prefer HAT or deprotonation. In some cases, the two reaction enthalpies show similar values and the two processes may occur simultaneously. Only thermodynamically favored 3',6,7-trianion of 6-hydroxypratensein showed preference of electron transfer. The dominant process can be also affected by the type of scavenged radical or the reaction kinetics of a particular process.

Acknowledgement

This work has been supported by the Slovak Grant Agency, projects 1/0504/20 and 1/0461/21. E.K. thanks the Ministry of Education, Science, Research and Sport of the Slovak Republic for funding within the scheme "Excellent Research Teams".

References

Alseekh S, de Souza LP, Benina M, Fernie AR (2020) Phytochemistry 174: 112347.

Altunkaya A, Gökmen V, Skibsted LH (2016) Food Chem. 190: 25—32.

Amorati R, Valgimigli L (2018) J. Agric. Food Chem. 66: 3324—3329.

Becke A (1993) J. Chem. Phys. 98: 5648—5652.

Biela M, Rimarčík J, Senajová E, Kleinová A, Klein E (2020) Phytochemistry 180: 112528.

Biela M, Kleinová A, Klein E (2022) J. Mol. Liq. 345: 117861.

Caicedo C, Iuga C, Castañeda-Arriaga R, Alvarez-Idaboy JR (2014) RSC Adv. 4: 38918—38930.

Cances E, Mennucci B, Tomasi J (1997) J. Chem. Phys. 107: 3032—3041.

Cances E, Mennucci B (1998) J. Math. Chem. 23: 309—326.

Di Meo F, Lemaur V, Cornil J, Lazzaroni R, Duroux J-L, Olivier Y, Trouillas P (2013) J. Phys. Chem. A 117: 2082—2092.

Frisch MJ, Trucks GW, Schlegel HB, Scuseria GE, Robb MA, Cheeseman JR et al. (2013) Gaussian 09. Revision D.01. Gaussian Inc., Wallingford, CT.

Han R-M, Tian Y-X, Liu Y, Chen C-H, Ai X-C, Zhang J-P, Skibsted LH (2009) J. Agric. Food Chem. 57: 3780—3785.

Hariharan PC, People JA (1973) Theor. Chim. Acta 28: 213—222.

Klein E, Rimarčík J, Senajová E, Vagánek A, Lengyel J (2016) Comput. Theor. Chem. 1085: 7—17.

Lee C, Yang W, Parr RG (1988) Phys. Rev. B 37: 785—789.

Lengyel J, Rimarčík J, Vagánek A, Klein E (2013) Phys. Chem. Chem. Phys. 15: 10895—10903.

Marković Z, Milenković D, Đorović J, Dimitrić Marković J, Lučić B, Amić D (2013) Monatsh. Chem. 144: 803—812.

Mathew S, Abraham TE, Zakaria ZA (2015) J. Food Sci. Technol. 52: 5790—5798.

Procházková D, Boušová I, Wilhelmová N (2011) Fitoterapia 82: 513—523.

Rassolov V, Pople JA, Ratner M, Windus TL (1998) J. Chem. Phys. 109: 1223—1229.

Rimarčík J, Lukeš V, Klein E, Ilčin M (2010) J. Mol. Struc. THEOCHEM 952: 25—30.

Škorňa P, Rimarčík J, Poliak P, Lukeš V, Klein E (2016a) Comput. Theor. Chem. 1077: 32—38.

Škorňa P, Michalík M, Klein E (2016b) Acta Chimica Slovaca 9: 114—123.

Vagánek A, Rimarčík J, Dropková K, Lengyel J, Klein E (2014) Comput. Theor. Chem. 1050: 31—38.

Veitch Nigel C (2007) Nat. Prod. Rep. 24: 417—464.

Xue Y, Liu Y, Luo Q, Wang H, Chen R, Liu Y, Li Y (2018) J. Phys. Chem. A 122: 8520—8529.

Zheng Y-Z, Deng G, Guo R, Fu Z-M, Chen D-F (2019) Phytochemistry 166: 112075.

Zheng Y-Z, Deng G, Zhang Y-C (2021) Phytochemistry 190: 112853.

sciendo

Pre-treatment of lignocellulosic materials by enzymatic mixture to enhance biogas production

Barbora Jankovičová, Miroslav Hutňan, Marianna Czölderová, Jana Barbušová

Slovak University of Technology, Faculty of Chemical and Food Technology, Department of Environmental Engineering, Radlinského 9, 812 37 Bratislava, Slovakia
barbora.jankovicova@stuba.sk

Abstract: The aim of this study was to evaluate the effect of an enzymatic mixture on the increase of biogas production from lignocellulosic materials as rapeseed straw, maize waste, and wheat straw. For efficient application of the enzymatic mixture, conditions of its use were optimized regarding 50 °C, pH 7 and an enzyme dose of 0.25 % w/v. Biogas potential test confirmed positive effect of the enzymatic mixture on anaerobic digestion of already thermally and alkali pre-treated lignocellulosic materials, as significantly higher biogas production was observed after the enzymatic mixture addition for all monitored substrates. Addition of the enzymatic mixture to the most used substrate at biogas plants — maize silage, had also positive effect on biogas production during the biogas potential test. This fact was not proven during long-term operations of the reactors as the values of total cumulative biogas productions for the whole monitored period from reactors for anaerobic digestion of maize silage with and without addition of enzymatic mixture did not differ significantly.

Abbreviations: COD — chemical oxygen demand, FM — fresh material, FPU — filter paper units, OLR — organic loading rate, RS — reducing sugars, TOC — total organic compounds, TS — total solids, U — amount of enzyme catalysing the reaction of 1 μmol of substrate per minute, VFA — volatile fatty acids, VS — volatile solids

Keywords: anaerobic digestion, biomass, long-term operation, maize silage, methane

Introduction

Anaerobic digestion of biodegradable materials yields a rich source of energy — biogas. Such materials include lignocellulosic biomass, which is a substrate with great potential for biogas production in terms of large production in agriculture, forestry, or industry. However, it is difficult to degrade due to the complexity of lignocellulosic biomass structure (Sawatdeenarunat et al., 2015). The goal of lignocellulosic biomass pre-treatment is to eliminate the reasons causing its resistance to the action of anaerobic microorganisms, i.e. lignin and hemicellulose content, cellulose crystallinity, accessible surface area and degree of cellulose polymerization (Zheng et al., 2014). Several pre-treatment methods including chemical (Pelera and Gidarakos, 2018), thermal (Pagliaccia et al., 2019) and physical methods (Kaur and Puthela, 2016; Menardo et al., 2012) have been studied to improve biogas yield from lignocellulosic biomass.

Biological pre-treatment methods including the application of fungi (Wan and Li, 2012), microorganism (Xu et al., 2018) and enzymes have recently been the subject of various studies. They represent potentially more energy-efficient, economical- and environment friendly alternatives to other types of pre-treatments as they do not require the addition of chemicals or high-energy inputs (Koupaie et al., 2019). The topic of our work was to study the effect of enzymatic pre-treatment on biogas production from lignocellulosic biomass, which has received less attention in literature.

Though, several papers have confirmed the positive effect of enzymatic pre-treatment of various lignocellulosic materials. The effect of enzymatic pre-treatment of switchgrass by cellobiase and cellulase was studied by El-Mashad (2015). Anaerobic digestion tests have shown positive effect of such pre-treatment on biogas production resp. methane production when the methane yield from pre-treated switchgrass (274.28 mL/g VS) was by 39 % higher compared to that from untreated material (197.39 mL/g VS).

Schroyen (2015) proved that enzymatic pre-treatment can help to degrade the matrix of lignocellulosic biomass as significant increase of phenolics leaking out of the matrix was observed. Laccase (2 U/g substrate) and versatile peroxidase (1.5 U/g substrate) were used to pre-treat materials such as wheat straw, corn stover, and others, with some additives and incubation at 30 °C for 6 h to increase enzyme activity. When the pre-treated materials were used as substrates in the biomethane potential test, an increase of 24 % and 12 % in methane production from corn stover and wheat straw (compared to the untreated sample) were observed respectively.

In another work, fungal hydrolytic enzyme mixture was used to improve hydrolysis and finally biogas production of selected lignocellulosic materials as these mixtures are increasingly available in the market. First, optimal conditions for enzymatic hydrolysis were determined: temperature of 40 °C, pH 5.4, and enzyme concentration 0.04 g enzyme/g VS of substrate. Application of fungal hydrolytic enzyme mixture is beneficial in large scale processes, as this pre-treatment positively affects the anaerobic digestion of selected materials (Quiñones et al., 2009).

In this paper, selected lignocellulosic materials were pre-treated using a commercial enzymatic mixture. Positive effect of this cheap alternative of enzymatic pre-treatment would lead to considerable savings as using separate enzymes is currently one of the most expensive pre-treatment methods. Optimization of the enzymatic mixture application, i.e. optimal temperature, pH value, and dose of enzymatic mixture, had to be done. Under optimized conditions, this pre-treatment method was further assessed by the biogas potential test using various already thermally or alkali pre-treated lignocellulosic materials such as wheat straw, maize waste, and rapeseed straw. The enzymatic mixture was also applied to the substrate most commonly used at biogas plants — maize silage. The effect of the enzymatic mixture was verified by the biogas potential test as well as by long-term operation of the reactors for anaerobic digestion of maize silage.

Materials and Methods

Substrates and inoculum

Lignocellulosic substrates used in this study to test the biogas potential were maize waste, rapeseed straw, and wheat straw, which are very common agriculture wastes. The commercial enzymatic mixture was also used to increase biogas production of maize silage, which is the most used substrate at biogas plants. The main physicochemical characteristics of the substrates are reported in Table 1.

As inoculum for the biogas potential test, anaerobically stabilized sludge from the wastewater treatment plant in Devínska Nová Ves was used. For long-term reactor operations for anaerobic digestion of maize silage, anaerobic sludge from biogas plant in Hurbanovo was used as inoculum; its characteristics are reported in Table 2.

Enzymatic mixture

The enzymatic mixture Everstar Culturpur, biologically active and ecologically harmless, used to accelerate the decomposition of organic matter in garden compost was used. It contains a mixture of enzymes, bacterial cultures, and nutrients beneficial for the microorganisms' action; cellulase content is < 1 % and it is in form of white to yellowish powder. Since the cellulase content was particularly interesting, the cellulase activity of this mixture was determined.

The use of such an enzymatic mixture for the pre-treatment of studied substrates is a cheaper and more environmentally friendly alternative to the other enzymatic pre-treatment methods, as it is a commercially available mixture.

Determination of enzymatic activity

Specific activity of the enzymatic mixture was determined according to Mandels et al. (1976). As a model cellulose raw material, filter paper (cellulose content 90—95 %) was used. To achieve

Tab. 1. Characteristics of substrates.

	maize waste	wheat straw	rapeseed straw	maize silage
TS (g/g)	0.9485	0.9405	0.9190	0.3565
VS (g/g)	0.9205	0.9225	0.8503	0.3340
COD (g/g)	1.31	1.20	1.24	–
Cellulose (%)	45.15	28.75	22.00	–
TOC (mg/g)	428.09	455.77	496.35	–

Tab. 2. Characteristics of inoculum.

	Inoculum for biogas potential tests	Inoculum for long-term reactor operations
TS (g/L)	25.6	13.1
VS (g/L)	14.1	10.8
VFA (mg/L)	432	3770
COD (mg/L)	3012	14500
N-NH_4 (mg/L)	420	864
P-PO_4 (mg/L)	26	23.4

the required pH value, 20 mL of buffers (0.1 M acetate buffers for pH 4 and pH 5, 0.1 M phosphate buffers for pH 6, pH 7 and pH 8) were added to flasks with weighed dry and ground model material of 1.6 ±0.01 g. Subsequently, the substrates were tempered at the temperatures of 30, 40, 50, 60 and 70 °C for 10 minutes. Hydrolysis mixture was prepared in the ratio of 50 mg of enzyme per 10 mL of water. Enzymatic mixture was dosed to the prepared flasks in the amount of 0.1 g, representing 0.5 % w/v. Samples were taken at various time intervals after the enzymatic mixture dose (2, 4, 6 and 8 h) to determine reducing sugars (RS) according to Somogyi (1952). The determined reducing sugars were used to calculate the enzyme activity and the specific enzyme activity**.** The amount of protein in the commercial enzymatic mixture was 69 mg/g of enzymatic mixture.

Test of biogas potential

Pre-treated materials were used as substrates for biogas potential tests to assess the effect of enzymatic mixture addition for the lignocellulosic materials' pre-treatment on biogas production. Lignocellulosic materials (rapeseed straw, wheat straw, and maize waste) were pre-treated using water or NaOH solutions (0.1 %, 0.25 % or 0.5 %) for 1 hour at 90—100 °C. Enzymatic mixture was added to pre-treated materials under optimized conditions (T = 50 °C, pH = 7, enzyme dose of 0.25 % w/v). The use of the enzymatic mixture to increase biogas production was also assessed for maize silage, where it was added in the amount of 0.2 g or 0.5 g to 5 g of maize silage.

The test of biogas potential was performed according to the method of Angelidaki et al. (2009). Substrates and inoculum (Table 2) were loaded to gas-tight flasks in triplicate. Flasks containing only inoculum and controls with pre-treated materials without enzymatic mixture addition were also tested. Before hermetically sealing the flasks with rubber septum, the sludge mixture was bubbled through with nitrogen for 1 minute. Biogas production was measured daily at given time intervals by volumetric method.

During the test, biogas was also collected in gas sampling bags and a gas analyser GA 2000 Plus (Geotechnical Instruments, UK) was used to determinate the biogas composition.

Long-term reactor operation

Long-term monitoring of anaerobic reactors for anaerobic digestion of maize silage without and with addition of the enzymatic mixture were performed under mesophilic conditions (37 °C) in semi-continuous reactors with a useful volume of 6.76 L. Anaerobic sludge from biogas plant Hurbanovo, which processes maize silage, was used as inoculum for the reactors' start-up (Table 2). Initial OLR (organic loading rate) of the reactors was 0.5 kg VS/($m^3 \cdot d$), which corresponds to a dose of maize silage of 10 g FM (fresh material). After 8 days of operation, OLR increased to 1 kg VS/($m^3 \cdot d$). When the sludge water parameters of both reactors were approximately the same, on the 36th day of operation, maize silage with the enzymatic mixture were added to one of the reactors. The enzyme dose was 0.04 g of enzyme/g FM of maize silage.

During the long-term operation of the reactors, parameters such as pH, total solids (TS), volatile solids (VS), chemical oxygen demand (COD), ammonia nitrogen (N-NH_4), phosphate phosphorus (P-PO_4), and volatile fatty acids (VFA) of sludge water were monitored. Biogas production was monitored daily and the biogas composition was determined by a gas analyser GA 2000 Plus (Geotechnical Instruments, UK) on the 29th and 52nd day of operation.

Analytic methods

Determination of COD, TS, VS, N-NH_4 and P-PO_4 concentrations was performed according to APHA (2017) and pH values during the experiments were determined using an ION-type ACTIVITY METER MS 20 pH meter. To determine VFA, three-point titration method according to Kapp (1984) was used. The Biuret method was used to determine the total protein concentration (Zheng et al., 2017).

Results and Discussion

Optimization of conditions for the use of a commercial enzymatic mixture

The most suitable enzymatic hydrolysis conditions for efficient use of the commercial enzymatic mixture were determined. Influence of temperature, pH, and concentration of enzymes resp. the ratio of the enzymes mass to the solution volume were studied to obtain the highest possible yield of fermentable sugars. The amounts of reducing sugars in mg released during enzymatic hydrolysis from 1.6 g of filter paper at different pH and temperatures are shown in Figure 1. Calculated specific enzymatic activities at the specified hydrolysis conditions are recorded in Table 3.

The largest amount of reducing sugars from 1.6 g of filter paper was released at 50 °C and pH 7; pH 7 seems to be the most suitable for enzyme activity at all examined temperatures. At 60 °C, the same amount of reducing sugars was released at pH 7 and pH 8 but the amount of sugars is by 50 % lower than that released at 50 °C and pH 7. At each

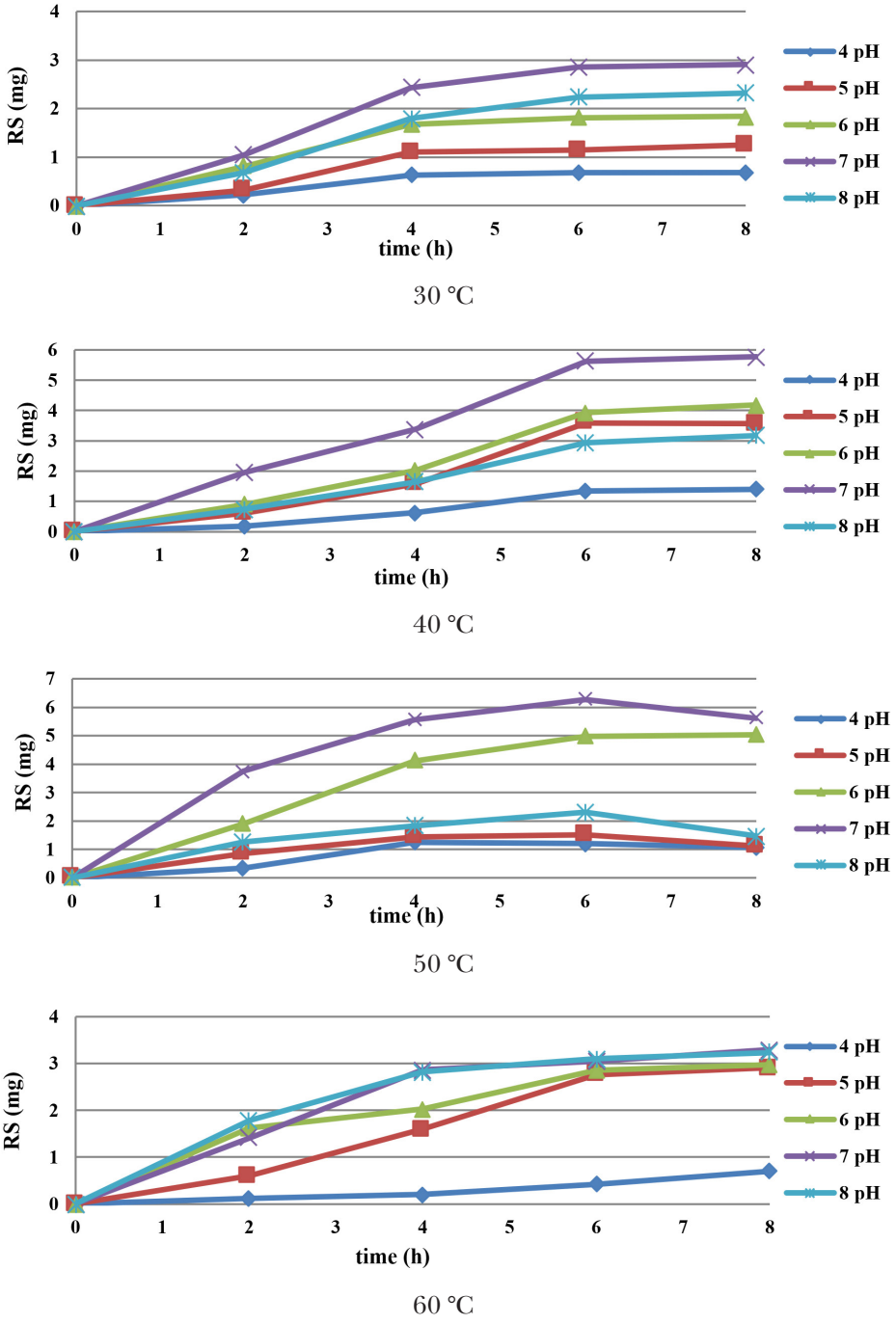

Fig. 1. Amount of reducing sugars released during enzymatic hydrolysis of filter paper.

Tab. 3. Specific enzyme activity at different conditions (temperature and pH).

specific activities (pkat/mg)	pH 4	pH 5	pH 6	pH 7	pH 8
30 °C	25.71	35.81	91.80	118.40	76.63
40 °C	19.75	69.87	100.97	223.00	85.01
50 °C	38.99	96.74	216.11	426.74	143.05
60 °C	13.79	68.03	184.69	159.69	203.13

studied temperature, the lowest amount of released reducing sugar was at pH 4.

After determining the optimal temperature and pH (50 °C, pH 7) of enzymatic hydrolysis, optimal dose of enzymes (ratio of enzymes to solution based on released reducing sugars during enzymatic hydrolysis) was determined. Results of the specific activities reported in Table 4 show that the highest specific activity was achieved at 0.25 % w/v and the lowest at 2.5 % w/v, which indicates lower required amount of the enzymatic mixture to be applied. This result is also consistent with the research of Ziemiński et al. (2012), where only slight increase of reducing sugars concentration in sugar beet pulp hydrolysates was observed with increasing dose of enzymes from 0.15 FPU/g TS to 0.75 FPU/g TS. Similarly, in Thulluri et al. (2014), the release of sugars increased with the increase in the enzyme dose from 5 to 25 U/g of substrate, but reached maximum concentration of released sugar at the enzyme loading of 20 U/g and no significant difference in sugar release was found between the enzyme loadings of 20 U/g and 25 U/g. A decrease in the total reducing sugar yield caused by increased enzyme concentration may be due to the lower amount of substrate available for enzyme attack (Thani et al., 2019).

Test of biogas potential of pre-treated lignocellulosic materials with addition of enzymatic mixture

To determine whether the dosing of enzymes into the mixture of anaerobic microorganisms influences substrate degradation or anaerobic microorganisms' activity and thus the result biogas production, biogas potential tests was performed. The enzymatic mixture was applied to lignocellulosic materials already pre-treated by environment friendly methods, water and NaOH at low concentration.

Tab. 4. Specific enzyme activity at different enzyme doses.

dose of enzyme (% w/v)	0.25	0.5	2.5
specific activities (pkat/mg)	691.47	426.74	86.53

After 1 hour of thermal and thermochemical pre-treatment with alkalis and subsequent enzymatic hydrolysis, the investigated materials were used as substrates for biogas potential test. The effect of single and combined pre-treatment (with enzymatic hydrolysis) on biogas production was compared. Table 5 shows the specific biogas production (biogas production based on VS of substrates) of substrates pre-treated by the selected methods / specific biogas productions of substrates pre-treated by the selected methods with the addition of the enzymatic mixture. The table shows a summary of specific biogas productions from solid and liquid fractions of pre-treated materials.

A comparison of individual specific biogas productions shows that the addition of an enzymatic mixture increased the production of biogas from pre-treated substrates except for one case, maize waste pre-treated by 0.25 % NaOH. Addition of the enzymatic mixture to thermally pre-treated materials increased the biogas yield for rapeseed straw by 23 %, that of wheat straw by 50 % and that of maize waste by 42 % compared to the biogas yields from thermally pre-treated substrates without the addition of the enzymatic mixture. The specific biogas production of materials pre-treated with 0.1 % NaOH and enzymatic mixture increased by 48 % for rapeseed straw, 85 % for wheat straw and by 58 % for maize waste compared to specific biogas production of pre-treated materials without the addition of the enzymatic mixture.

Pre-treatment with 0.25 % NaOH together with the enzymatic mixture resulted in up to 38 % and 40 % increase in specific biogas production of rapeseed straw and wheat straw, but a slight decrease (5 %) was observed for maize waste. Application of the enzymatic mixture to materials pre-treated with 0.5 % NaOH also showed positive effect on biogas production; the specific biogas production of the studied materials (rapeseed straw, wheat straw and maize waste) increased by 4 %, 25 % and 62 %, respectively.

Compared to untreated substrates, the largest increase (by 302 %) in biogas production was measured in for wheat straw pre-treated with 0.5 % NaOH with the addition of an enzymatic mixture. The method using 0.5 % NaOH and the addition of an enzymatic mixture was proved to be a very

Tab. 5. Results of biogas potential tests.

	Specific biogas production (mL/g VS)				
	untreated	**water/+E**	**0.1 % NaOH/+E**	**0.25 % NaOH/+E**	**0.5 % NaOH/+E**
rapeseed straw	64.1	75.1/92.3	122.1/180.1	140.5/193.5	222.5/231.3
wheat straw	71.0	90.3/135.4	127.4/235.0	182.4/255.3	227.6/285.4
maize waste	109.3	108.7/154.3	211.2/334.1	245.1/233.9	257.0/415.1

effective pre-treatment method as a significant increase in biogas production also for other substrates (261 % for rapeseed straw and 280 % for maize waste) was observed.
The biogas potential test confirmed that this enzymatic mixture has positive effect on the action of anaerobic microorganisms and the decomposition of lignocellulosic biomass, which structure was already disturbed by previous pre-treatment.
The great potential of the combination of alkaline (5 % NaOH) and enzymatic pre-treatment of lignocellulosic biomass degradation and anaerobic digestion was also proved by Michalska et al. (2015). There was significant increase in biogas production when a combination of methods was used compared to the biomass pre-treated only with NaOH. As the cumulative biogas production for Miscanthus and Sida pre-treated both chemically and enzymatically was 421.5 Ndm^3/kg TS and 316.3 Ndm^3/kg TS and for biomass pre-treated only chemically it was 8.7 Ndm^3/kg TS and 57.4 Ndm^3/kg TS. The low biogas production from biomass pre-treated by 5 % NaOH is justified by the high concentration of phenolic compounds released as the results of lignin degradation.

Application of enzymatic mixture to maize silage

The enzymatic mixture was also applied to maize silage, which is the most used substrate at biogas plants. The effect of enzymatic mixture dosing to maize silage was assessed based on the biogas potential test and long-term operation of semi-continuous reactors.
Results of the biogas potential test after 16 days (Table 6) show that addition of the enzymatic mixture to the substrate increased the final biogas production. With the addition of 0.2 g of enzyme, the production of biogas increased by 32 % compared to that from maize silage without enzyme addition. At 0.5 g of used enzyme, the biogas production increased by only 13 %. Also, a lower dose of the enzymatic mixture proved to be more suitable in this experiment.
Addition of the enzymatic mixture to a substrate (maize silage) in long-term operation of laboratory models of semi-continuous reactors was further investigated to compare whether it affects biogas production on a long-term basis. Based on the results of the previous biogas potential test, the enzyme dose in long-term operation was in a lower ratio (0.04 g enzyme/g silage (FM)).
Results of long-term reactors' operation are shown in the course of daily biogas production from both reactors (Figure 2), where the start of enzymatic mixture dosing is also marked (from the 36th day) as it significantly affected the amount of daily biogas production. The increase in biogas production, by 25 % higher on average, lasted only for 14 days. After 50 days of operation, the biogas production values in both reactors returned to comparable values. Ultimately, the values of the total cumulative biogas productions for the whole monitored period did not differ significantly (Figure 3).
This can be explained by the microbial diversity probably occurring after the addition of the enzymatic mixture, which could support the growth of specific bacteria. Similar results are reported in Romano et al. (2009), where addition of the enzymatic mixture Novozyme 342 (with a high proportion of cellulases) with wheat grass directly into the anaerobic digestion process was studied. Their results show that the rate of biogas production was significantly affected but it decreased significantly after 10 days. Even the enzyme products showed positive effects on the solubilization of wheat grass when used alone, there were no significant improvements in the final biogas yield of the anaerobic digestion systems.
Similarly, methane content of biogas (Table 7) in the period before and after the start of the addition of the enzymatic mixture did not show significant differences between the reactors. Even in the reactor without the addition of enzymatic mixture showed higher methane content after 52 days.
Average values of the monitored parameters (Table 8) in sludge water from the reactors during operation did not differ significantly even when an enzymatic mixture was added to one of the reactors. Also, the values of VS in both reactors were about 70 %, which reveals that the enzymes did not cause higher decomposition of maize silage.
Despite the previous result of the biogas potential test, which showed increased biogas production, this fact was not proven during long-term reactors' operation.
For comparison, in Dubrovskis and Plume (2017), where the enzyme mixture of cellulase, b-gluconase

Tab. 6. Results of biogas potential test.

dose of maize silage (g FM)	–	**5**	**5**	**5**
dose of enzymatic mixture (g)	–	–	**0.2**	0.5
total biogas production (mL)	108	800	**1180**	920
specific biogas production (mL/g VS)	–	479	**707**	551

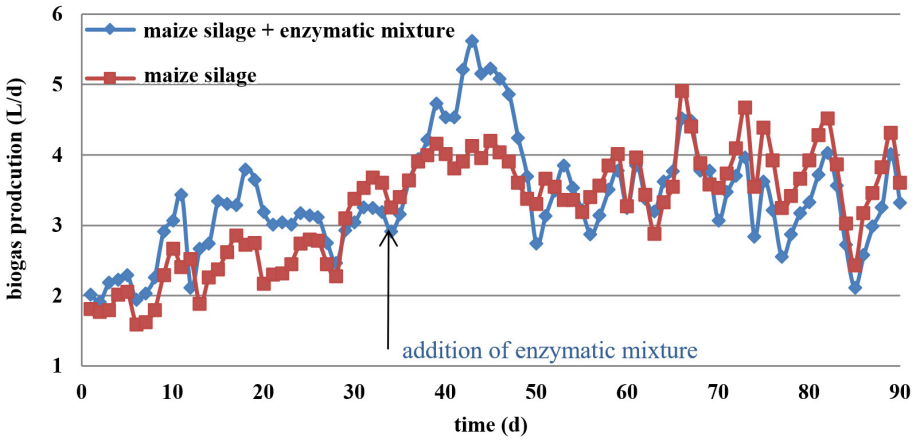

Fig. 2. Daily biogas production.

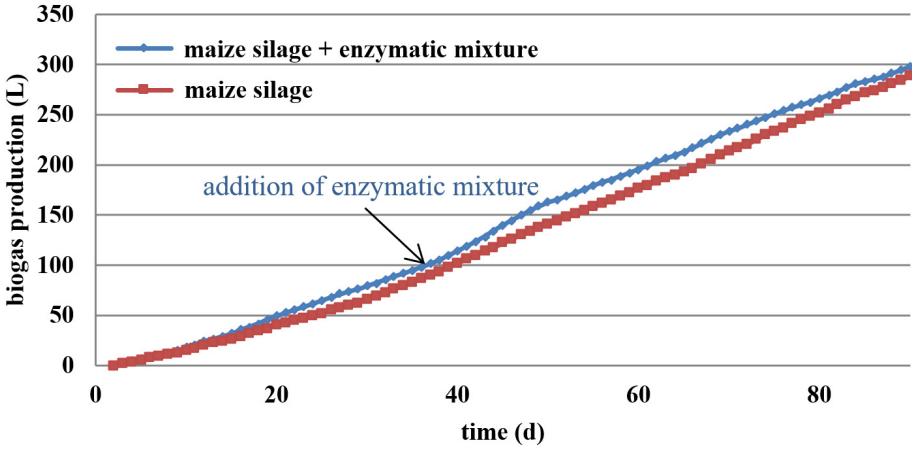

Fig. 3. Cumulative biogas production.

Tab. 7. Biogas composition on the 29th and 52nd days of long-term reactors' operation (R1 — maize silage with the addition of enzymes from 36th day, R2 — maize silage without the addition of enzymes).

	29th day		52nd day	
	R_1	R_2	R_1	R_2
CH_4 (%)	49.2	49.4	52.6	57.2
CO_2 (%)	49.4	48.3	46.6	42.2
O_2 (%)	0.4	0.5	0.2	0.3
H_2 (ppm)	29	31	109	112
H_2S (ppm)	76	231	276	104

Tab. 8. Average concentrations of monitored parameters in sludge water from reactors (R1 — maize silage with the addition of enzymes from 36th day, R2 — maize silage without the addition of enzymes).

days	pH		COD (mg/L)		VFA (mg/L)		N-NH_4 (mg/L)		P-PO_4 (mg/L)	
	R_1	R_2	R_1	R_2	R_1	R_2	R_1	R_2	R_1	R_2
1—36	7.2	7.3	12 379	10 675	6733	5386	1009	1041	57	56
37—50	7.3	7.4	15 802	15 127	5650	5358	921	945	16	14
51—90	7.4	7.3	17 410	12 808	2516	2517	905	903	52	48

and xilanase enzymes was used to improve the process of anaerobic digestion of maize silage, a slight increase in biogas production was observed. When maize silage and an enzymatic mixture, 0.03 g/g silage (FM), were added to a bioreactor with inoculum, the specific biogas production was 0.681 L/g VS while the specific biogas production from bioreactor without added enzymes was 0.632 L/g VS. Specific methane yield from the bioreactor with maize silage with enzyme mixtures was by 7.76 % higher compared to that obtained from the bioreactor with maize silage without the addition of enzymes. Also, the difference in biogas methane content was not significant, i.e. 53.6 % after the addition of the enzyme and 53.2 % without the enzyme addition.

Conclusion

Application of an easily available commercial enzymatic mixture under optimized conditions (50 °C, pH 7 and an enzyme dose of 0.25 % w/v) to already pre-treated lignocellulosic substrates has resulted in a significant increase in biogas production from lignocellulosic materials such as wheat straw, maize waste, and rapeseed straw. The highest increase in specific biogas production after enzymatic mixture addition (by 85 %) was observed for wheat straw pre-treated with 0.1 % NaOH. Also, for other materials and pre-treatment methods, the biogas potential test confirmed that this enzymatic mixture has positive effect on the decomposition of lignocellulosic biomass and thus biogas production. The addition of the enzymatic mixture to maize silage also showed positive effect on the biogas production during the biogas potential test. However, since this positive effect did not show during long-term reactor operation, it cannot be confirmed that the enzymatic mixture support biogas production on a long-term basis.

References

Angelidaki I, Alves M, Bolzonella D, Borzacconi L, Campos JL, Guwy AJ, Kalyuzhnyi S, Jenicek P, van Lier JB (2009) Water Sci. Technol. 59 (5): 927–934.

APHA/AWWA/WEF (2017) Standard Methods for the Examination of Water and Wastewater. American Public Health Association, USA. ISBN: 978-0-87553-287-5.

Dubrovskis V, Plume I (2017) Proceedings of 16. Conference Engineering for Rural Development 16: 443–448.

El-Mashad HM (2015) Biochem. Eng. J. 93: 119–127.

Kapp H (1984) Schlammfalung mit hohem Feststoffehalt. Munchen: Oldebourg.

Kaur K, Phutela UG (2016) Renew. Energy 92: 178–184.

Koupaie EH, Dahadha S, Bazyar Lakeh AA, Azizi A, Elbeshbishy E (2019) J. Environ. Manage. 233: 774–784.

Mandels M, Andreotti R, Roche C (1976) Biotechnol. Bioeng. Symp. 6: 21–23.

Menardo S, Airoldi G, Balsari P (2012) Bioresour. Technol. 104: 708–714.

Michalska K, Bizukojć M, Ledakowicz S (2015) Biomass Bioenergy 80: 213–221.

Pellera FM, Gidarakos E (2018) Waste Manage 71: 689–703.

Pagliaccia P, Gallipoli A, Gianico A, Gironi F, Montecchio D, Pastore C, di Bitonto L, Braguglia CM (2019) J. Environ. Manage. 236: 100–107.

Quiñones TS, Plöchl M, Budde J, Heiermann M (2009) Int. Wissenschaftstagung Biogas Sci. 2009: 137–149.

Romano RT, Zhang R, Teter S, McGarvey JA (2009) Bioresour. Technol. 100(20): 4564–4571.

Sawatdeenarunat C, Surendra KC, Takara D, Oechsner H, Khanal SK (2015) Bioresour. Technol. 178: 178–186.

Schroyen M, Vervaeren H, Vandepitte H, Van Hulle SWH, Raes K (2015) Bioresour. Technol. 192: 696–702.

Somogyi MJ (1952) J. Biol. Chem. 195: 19–23.

Thulluri C, Uma A, Konakalla R, Rani G, Reddy Shetty P, Pinnamaneni SR, Akula U (2014) Journal of Biochemical Technology 5: 775–781.

Thani N, Mustapa Kamal S, Taip F, Sulaiman A, Omar R (2019) Food Research 3(4): 313–316.

Wan C, Li Y (2012) Biotechnol. Adv. 30 (6): 1447–1457.

Xu W, Fu S, Yang Z, Lu J, Guo R (2018) Bioresour. Technol. 259: 18–23.

Zheng Y, Zhao J, Xu F, Li Y (2014) Prog. Energy Combust. Sci 42: 35–53.

Zheng K, Wu L, He Z, Yang B, Yang Y (2017) Measurement 112: 16–21.

Ziemiński K, Romanowska I, Kowalska M (2012) Waste Manage. 32(6): 1131–1137.

sciendo

Nanotextiles — materials suitable for respiratory tract protection but a source of nano- and microplastic particles in the environment

Petra Roupcová[b], Hana Kubátová[c], Kateřina Bátrlová[a], Karel Klouda[a, b]

[a]Occupational Safety Research Institute, v.v.i., Jeruzalémská 9, 110 00 Prague 1
[b]VSB – Technical University of Ostrava, FBI, Lumírova 13, 700 30 Ostrava
[c]The State Office for Nuclear Safety, Senovážné náměstí 9, Prague 1

Abstract: The paper deals with the formation of nanomaterials (nanoparticles and nanofibers) in the manufacture and use of respiratory protective equipment. It focuses mainly on processes leading to the release of nanoplastics into the workplace and the environment. Based on selected properties of materials used for the manufacture of protective equipment, their stability in the environment is revealed. The paper demonstrates the impact on the environment considering semichronic phytotoxicity of nanoplastics.

Keywords: nanofiber, electrospinning, nonwovens, nanoparticles, respirator

Introduction

Numerous studies (Waymana and Niemann, 2021; Gerritse et al., 2020; Brewer et al., 2021; Pirsaheb et al., 2020; Pivokonský et al., 2020; Novotná et al., 2019) have confirmed the occurrence of nano- and microplastics in the waters of the world's oceans and fresh waters, including drinking water. Similarly, the presence of nano- and microplastics has been confirmed in soil (Brewer et al., 2021; Wahl et al., 2021). Primary source of nanoplastics in nature is the production and processing of plastics while secondary source of nanoplastics is the fragmentation of plastic products (Barnes et al., 2009). Fragmentation of plastics is the result of a number of processes which depend on both the composition of plastics and environmental conditions. Fragmentation involves physical, physico-chemical, and biological processes (cracking, friction, photo oxidation, hydrolysis, biodegradation) (Gerritse et al., 2020; Barnes et al., 2009; Enfrin et al., 2020).

Nano- and microplastics released into the environment affect organisms present in the environment. The best studied problem (although still not sufficiently) is currently the effect of nano- and microplastics on aquatic organisms. The effect on living organisms depends on the concentration of plastic particles, their size, and shape, the material from which they originate, and the time of exposure (Kögel et al., 2020; Barboza et al., 2018). Toxic effects of nano- and micro-plastics are therefore influenced, for example, by flame retardants present in polymers, organic pollutants adsorbed on the plastic surface, pesticides, heavy metals (Brennecke et al., 2016), or antibiotics (Guo and Wang, 2019). Plastic particles affect the behavior and neurological functions of fish, intestinal permeability, metabolism, and diversity of their intestinal microbiomes (Barboza et al., 2018; Jacob et al., 2020). At the same time, they affect the immune system of fish (Barboza et al., 2019), their hormonal regulation and reproduction, they alter fat metabolism, and cause oxidative stress in cells (Kögel et al., 2020). The number of negative effects observed in fish increases as the size of the plastic particles decreases (Jacob et al., 2020; Lee et al., 2013).

Nano- and microplastics enter the soil in various ways. One of them is pollution from water and wastewater treatment plants (especially particles and fibers released during the laundering of clothes). Contamination from water treatment plants reaches higher levels in soils than in water (Wahl et al., 2021; Nizzetto et al., 2016). Nano- and microplastics in soils affect soil micro- and macroorganisms and their condition, the soil properties and thereby even the cycles of substances in the soil (Wahl et al., 2021; Maity and Pramanick, 2020).

The current pandemic of the COVID-19 respiratory disease has increased the demand for respiratory protective equipment, especially masks and respirators and those including nanotextiles made of plastic nanofibers are especially popular and widely used. Due to the number of nanotextile-based masks and respirators used daily, their production, use and improper and unregulated disposal contribute to and will continue to contribute to increasing environmental pollution by nanoplastics (Sullivan et al., 2021). Therefore, we decided to identify processes that can be considered as sources of nanoparticles in the life cycle of protective devices containing nanofibers, and to further investigate them.

The following were specified as processes that lead to the release of nanoparticles into the work and natural environment:

1. Production of nanofibers by electrostatic spinning (leakage into the working environment, exposure of employees),
2. Production of nanofiber respirators and nanofiber masks by processing textiles containing nanofibers (leakage into the working environment, exposure of employees),
3. Use of nanofiber respirators and nanofiber masks, especially the mechanical stress of nanofiber textiles that are part of them (leakage into the environment, exposure of people in the vicinity),
4. Improper disposal and removal of used nanofiber respirators and nanofiber masks (disposal into elements of the environment — water, soil); effect of pollutant particles adsorbed on nanotextiles or absorbed (intercalated) undesirable substances between layers of nonwoven fabric and nanotextile changing their toxicological properties may be present.

Assessment of protective equipment as a possible source of nanoplastic particles

Production of nanofibers by electrostatic spinning

Nanotextile-based protective devices usually consist of non-woven fabric onto which nanofibers formed by electrospinning have been applied. Nanoparticle concentration released into the working environment was measured at three workplaces where continuous production of nanofiber textiles takes place — SPUR a.s., NAFIGATE Corporation a.s., and Nano Medical s.r.o. At these companies, different technological arrangement is used for the production of nanotextiles. However, the space where the actual spinning of the input material takes place is always separated from the surrounding working environment. Air from the spinning chamber is removed and filtered through HEPA filters.

A testo DiSCmini 133 instrument was used for the measurement, enabling the measurement of nanoparticle concentrations in the range of 10—700 nm. At SPUR a.s., SpurTex material is produced on a production line for the preparation of nanofibers of their own design — SPIN Line. The measured nanoparticle concentrations in the working environment where an operator is present ranged from 30,000 to 40,000 $\# \cdot cm^{-3}$, and the mean diameter of the nanoparticles was about 40 nm.

At NAFIGATE Corporation, a.s. and Nano Medical s.r.o., nanotextiles are produced on lines manufactured by ELMARCO s.r.o. These electrospinning lines comprise two spinning segments with string electrodes. During our measurements, polyvinylidene difluoride (PVDF) was spun from a dimethylacetamide solution at both companies. The resulting PVDF nanotextile was immediately laminated between two layers of spunbond nonwoven fabric. The measured course of nanoparticle concentrations had a pulsating character at both workplaces. In the area for the line operator, values in the interval 4,000—7,000 $\# \cdot cm^{-3}$ with more pronounced peaks at 9,000 $\# \cdot cm^{-3}$ and 16,000 $\# \cdot cm^{-3}$ were measured at Nano Medical s.r.o. (Fig. 1). At NAFIGATE Corporation a.s., nanoparticle concentrations in the range of 2,000–8,000 $\# \cdot cm^{-3}$ with an average of 4,000 $\# \cdot cm^{-3}$ were measured, the mean diameter of the nanoparticles was about 30 nm. Fluctuations at low concentration were measured, increasing the average to 60; 100; 180 nm.

Processing of textiles made of nanofibers into a product

One processor of nanotextiles, PARDAM NANO-4FIBERS s.r.o., is a manufacturer of nanofiber respirators. At this company, measurements were performed during two different processing steps which take place in the same production space

Fig. 1. Large-capacity production line for continuous production of nanofiber textiles at Nano Medical s.r.o. Letter A indicates the location of the spinning units with containers of polymeric material.

Fig. 2. Automated extrusion line for nanotextile respirators.

Fig. 3. Automated line for nanofiber masks Nanovia Mask 99,97 production.

(production hall). The first place was the place designated for cutting nanotextiles from coil into strips which are then used in an automatic line for extruding respirators. The testo DiSCmini 133 instrument was used again for the measurement. Near the cutting machine, when cutting the PA-6 nylon nanotextile on a polypropylene (PP) substrate, nanoparticle concentrations of approx. 37,000 $\#\cdot cm^{-3}$ were measured (cutting process is not separated from the surrounding working environment in any way). The second place was the space around the automatic line for extruding respirators, see Fig. 2 (the space where the actual extrusion takes place is separated from the working environment in the hall). Nanoparticle concentration in the space where the line operator is present reached the values of 15,000–25,000 $\#\cdot cm^{-3}$.

The next measurement was done at the nanofiber mask manufacturer Nanovia Mask 99,97 (name omitted at the request of the manufacturer). A three-layer sandwich is used for the mask production, the middle layer of which has a nanofiber structure (PVDF). The production of nanofiber masks takes place in a hall (190 m^3) where the production line is located (Fig. 3). No part of the production line is separated from the working environment of the hall, and the hall is not equipped with exhaust ventilation. This fact is most likely the reason why higher nanoparticle concentrations were measured in the working environment of the hall ranging from 40 000–60 000 $\#\cdot cm^{-3}$.

Mechanical stress of nanofiber materials

Mechanical stress during the use of products that include nanotextiles was simulated by squeezing and kneading nanotextile samples. Pilot measurements were performed with about 2 m^2 of a three-layer sandwich with an inner layer formed

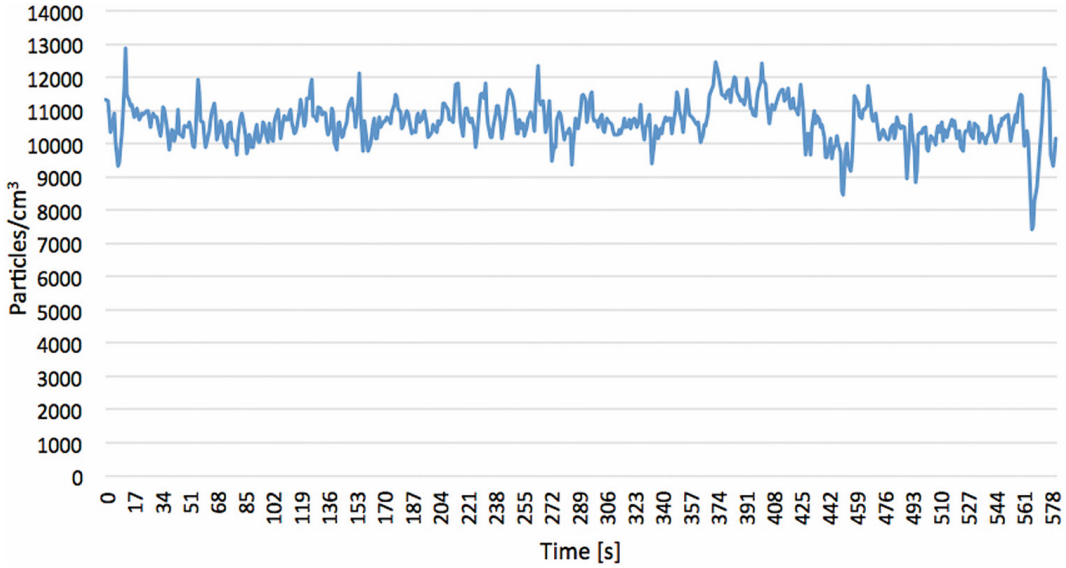

Fig. 4. Nanoparticle concentration measured during slight kneading of nanotextiles (PP + PVDF).

by PVDF nanofibers. A sample of the nanotextile was kneaded on a desk in the office for 10 minutes, with the testo DiSCmini 133 measuring instrument placed 0.5 m above the tabletop. The course of the nanoparticle concentration had a pulsating character in the range of 10,000—12,500 $\#\cdot cm^{-3}$ (Fig. 4) with a mean diameter of nanoparticles of 75—80 nm.

Testing of selected material properties for nanofiber masks and respirators production

Because various physical, physico-chemical, but also biological processes are involved in the fragmentation of plastics, including textile fibers used in the manufacture of respiratory protective devices (Gerritse et al., 2020; Barnes et al., 2009; Enfrin et al., 2020), several experiments during which the related release of nanoparticles into the environment was monitored were conducted. Materials that are either semi-finished products or are directly used to produce nanofiber masks and nanofiber respirators of the FFP-2 class were tested. These are layered fabrics composed of non-woven PP fabrics created by Spunbond (S) and Meltblown (M) technologies, on which PVDF nanofiber is applied by electrospinning. The nanotextile layer is then laminated with a non-woven PP fabric (S), creating a sandwich textile triple layer (PP fabric created by S and M technologies behaves as a single layer). Samples for testing were obtained from the manufacturer NAFIGATE Corporation a.s., and both the fabric with nanolayer laminated layer of PP (S) and the fabric with exposed nanolayer — without lamination with the last PP (S) layer, were tested.

Adhesion of nanofibers to carrier fabric

For adhesion testing, i.e., the cohesion of nanofibers with a carrier nonwoven fabric, a device allowing unfixed nanofibers blowing was built. The device contains two fans — one blows air into a slot nozzle located 5 mm above the tested surface. The second directional fan discharges air with loose nanofibers outside the device to the testo DiSCmini 133 measuring instrument, see Fig. 5. Data were obtained by moving the device over the tested fabric.

Measured values of nanoparticle concentrations released from both types of tested samples were surprising. While 8,000—10,000 $\#\cdot cm^{-3}$ with a stable mean particle diameter of about 54 nm is released from the laminated fabric, significantly fewer particles with the size in the range of 10—700 nm are released from the non-laminated sample (measuring instrument range). The obtained nanoparticle concentrations for the non-laminated sample reached values in the range of approx. 6000—7000 $\#\cdot cm^{-3}$.

This is probably due to the nanotextile layer serving also as a filter layer in this case. From the microscopic image of the exposed (non-laminated) nanofiber layer of PVDF (Fig. 6), significantly higher fiber density can be seen in this layer than in the top layer of the nonwoven PP fabric (Fig. 7).

Thermal stability and microscopic analysis of input materials

Using thermogravimetric analysis, a sample of the laminated material and a sample of the nanofiber layer itself formed of PVDF nanofibers withdrawn from the carrier nonwoven fabric, were analyzed. In the laminated product analysis (Fig. 8), endo effect

Fig. 5. Experimental equipment for blowing fibers (nanofibers).

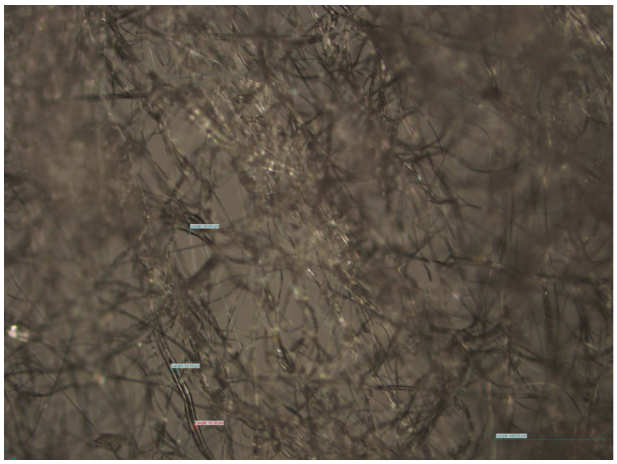

Fig. 6. Microscopic image of exposed (non-laminated) PVDF layer (magnification 20×).

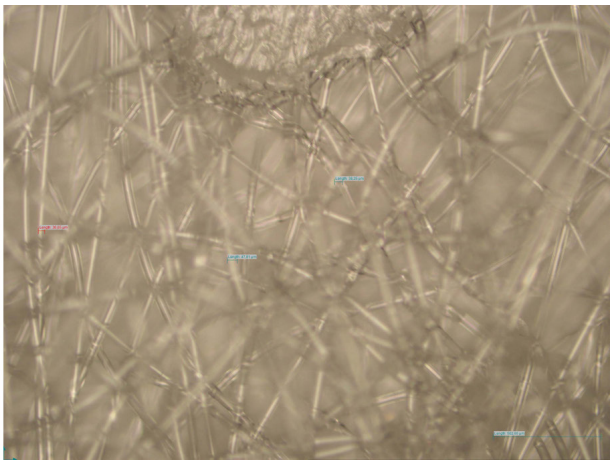

Fig. 7. Microscopic image of upper layer of PP unwoven textile (magnification 20×).

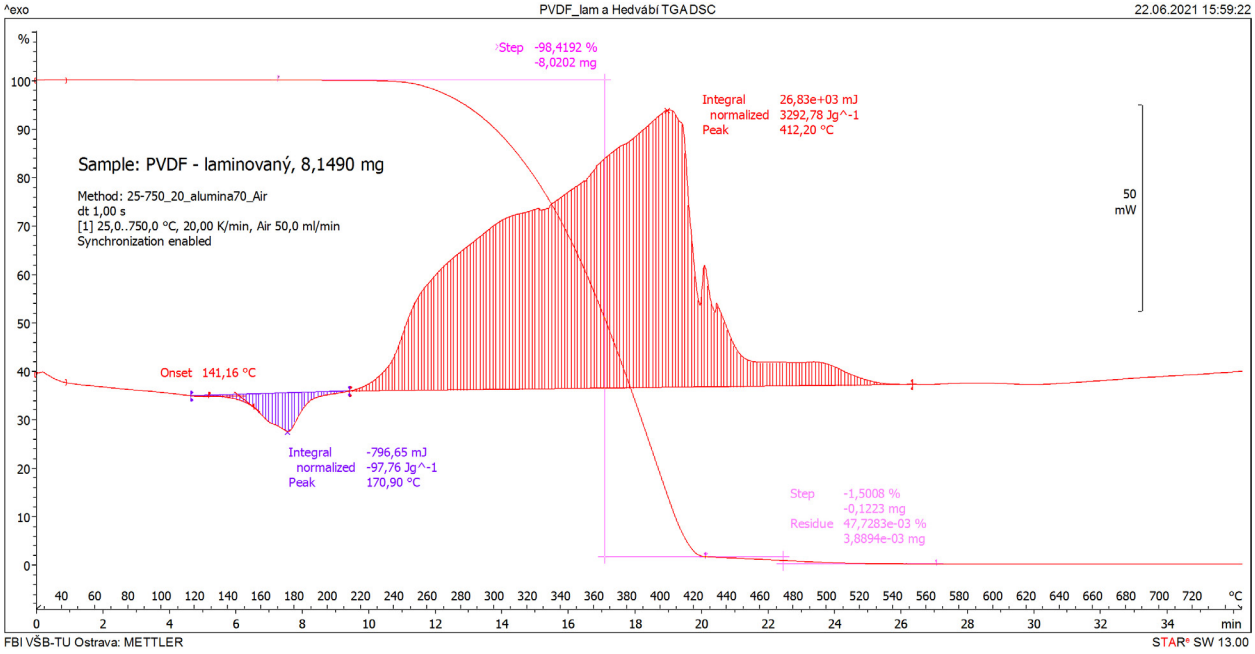

Fig. 8. Thermogravimetric analysis of laminated material.

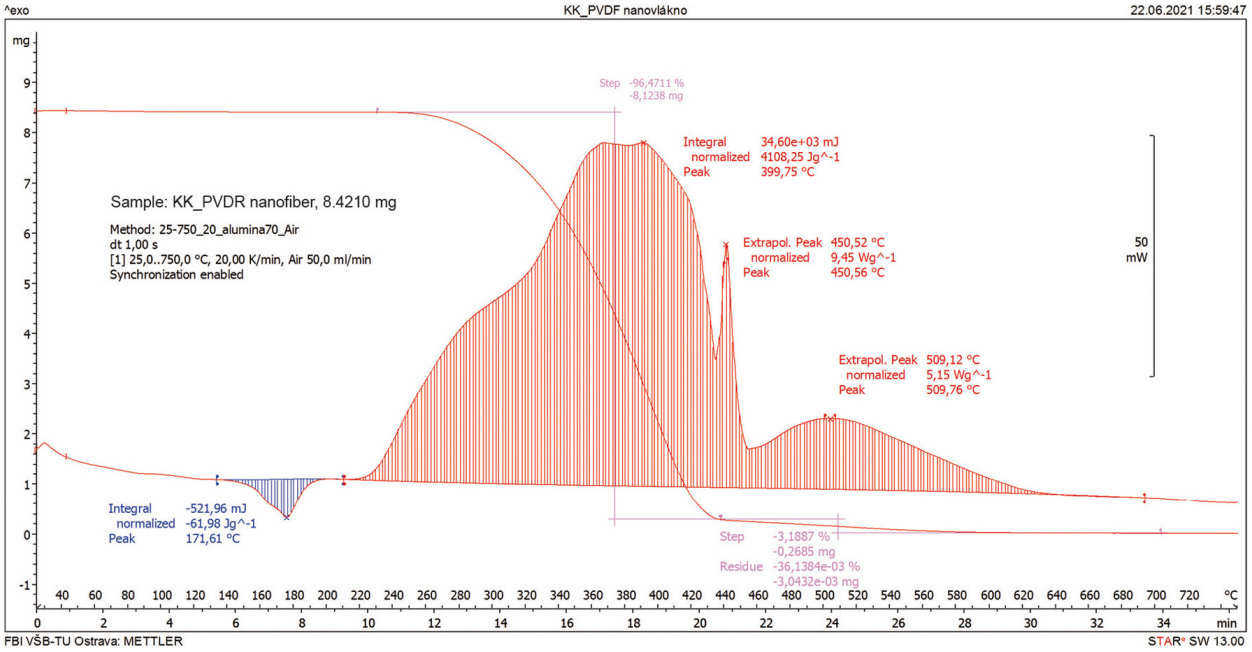

Fig. 9. Thermogravimetric analysis of nanofiber layers formed by PVDF nanofibers.

was recorded at 171 °C without weight loss. From the temperature of 215 °C to 425 °C, decomposition with exo effect with a maximum at 412 °C, essentially with complete weight loss, was observed. The weight loss (remaining from %) was terminated at 550 °C. In the analysis of the separate PVDF nanofiber layer (Fig. 9), endo effect was also recorded at 171.6 °C without weight loss. From 210 °C to 440 °C, exo effect was recorded with weight loss of 96 %. The residue shows exo effect with two peaks, at 450 °C and 509.7 °C. The decomposition of the PVDF nanotextile was completed at 640 °C.

From a comparison of the spectra in Figs. 8. and 9. it is evident that decomposition of the laminated product occurred at a temperature lower by 100 °C than of the separately analyzed nanofiber PVDF layer. This result can be explained by the very close direct contact of PP and PVDF polymers (lamination takes place at elevated temperature and pressure), where they interact at high temperatures which results in faster decomposition.

Static tensile test

Tensile strength test of textiles was performed on a SHIMADZU EZ-LX testing machine (Fig. 10); to achieve adequate measurement results, calibration of the instrument itself was performed one week before the actual measurement. This test was performed only with the sample of laminated material. All samples tested were 15 mm wide and 150 mm long and were prepared differently based on the source material, the weight of nanotextiles was 93.6 g/m^2. LAM 1 samples were cut with the longer side across the winding direction of the fabric during its production, LAM 2 samples were cut with the longer side in the winding direction.

Results of the strength test are summarized in the tensile diagram (Fig. 11). The curves obtained by testing individual samples differ not only in their course, but especially in the value of the maximum force [N] to reach the ultimate strength. For LAM 2 sample, the value of the maximum force was doubled (Fig. 11), but the relative elongation of the sample was greater in LAM 1 (Fig. 10a).

Semichronic toxicity test on seeds

According to the OECD methodology (OECD, 2006), white mustard (*Sinapis alba L.),* rapeseed (*Brassica napus*), fescue (*Festuca pratensis*) and lettuce (*Lactuca sativa*) seeds were used on non-laminated PVDF samples (seeds were placed on the exposed PVDF layer), laminated PP-PVDF, unworn Nanovia Mask 99,97, and worn Nanovia Mask. Germination and inhibition of root growth were determined in seeds placed on and off the test fabric (Figs. 12 and 13). Calculation of root growth inhibition when applying seeds to/off the tested nanotextile is based on the measurement of the root length (root elongation) after the end of the test and follows from the formula:

$$I = \frac{L_C - L_V}{L_C} \cdot 100 \qquad (1)$$

where I is the inhibition or stimulation of root growth (%), L_c is the average root length in the control sample (mm), and L_v is the average root length in the test sample (mm). The resulting

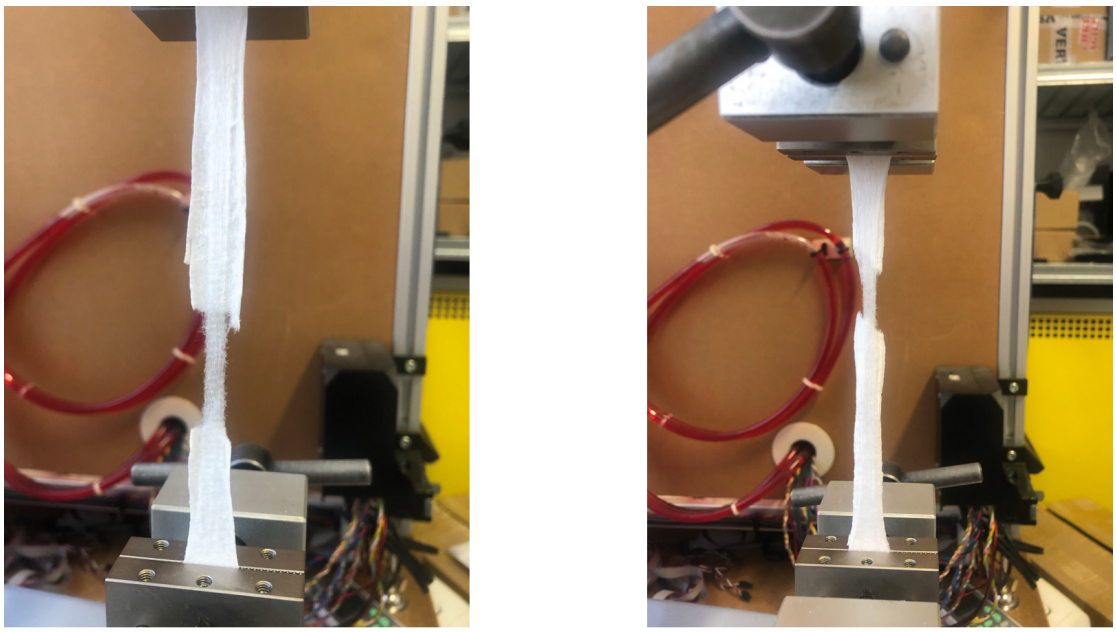

a) b)

Fig. 10. Tensile test a) LAM 1 sample across the wound fabric; b) LAM 2 sample in the winding direction.

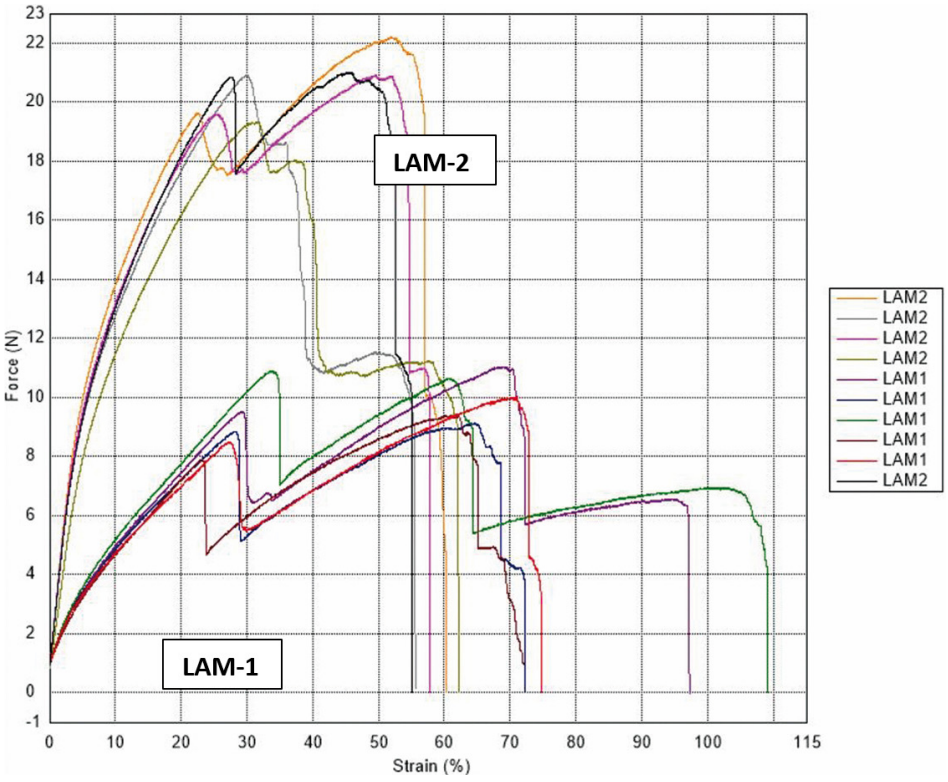

Fig. 11. Tensile diagram of laminated material (LAM 1 and LAM 2 sample).

value of $I > 0$ represents inhibition of root growth, while $I < 0$ shows stimulation of its growth.

Figs. 14 and 15 show charts comparing the inhibition on mustard and rapeseed in case of direct contact with the sample and off of it.

From Fig. 14 it can be seen that a significantly higher inhibition of root growth occurred in mustard and rape seeds in direct contact with the nanotextile. The average inhibition reaches values of more than 50 %. For lettuce, the highest inhibition was found for seeds placed on the unworn Nanovia Mask sample (85.5 %), for seeds placed off the fabric, the highest inhibition was found for the non-laminated PVDF sample (55.42 %). In meadow fescue, on the

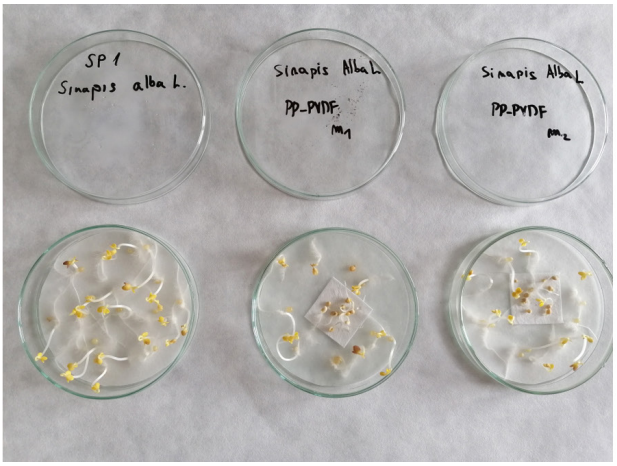

Fig. 12. Semichronic toxicity test on *Sinapis alba* L. (white mustard) after testing (72 hours), experimental temperature: 21 ° C. Left: control determination (control), 2× parallel samples: PP-PVDF lam. m_1 and m_2.

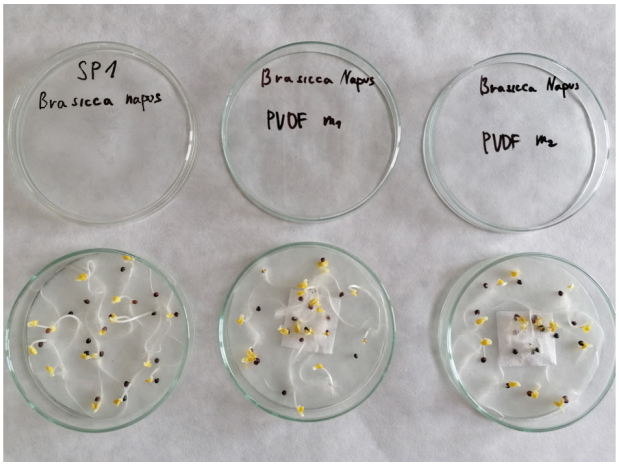

Fig. 13. Semichronic toxicity test on *Brassica napus* (rapeseed) after testing (72 hours), experiment temperature: 21 °C. Left: control set (control group), 2× parallel samples: Nonlam. PVDF m_1 and m_2.

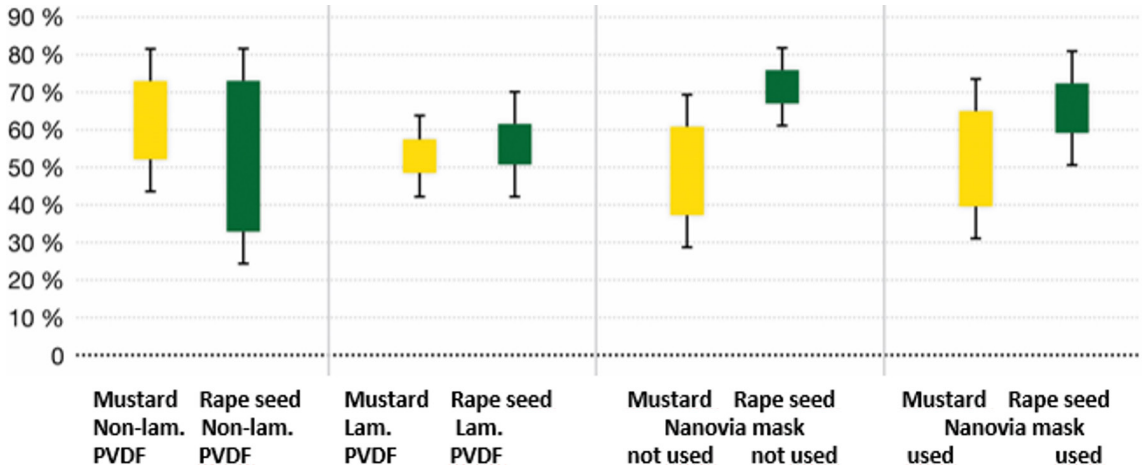

Fig. 14. Chart comparison of inhibition of mustard and rapeseed root growth in % (seeds on sample).

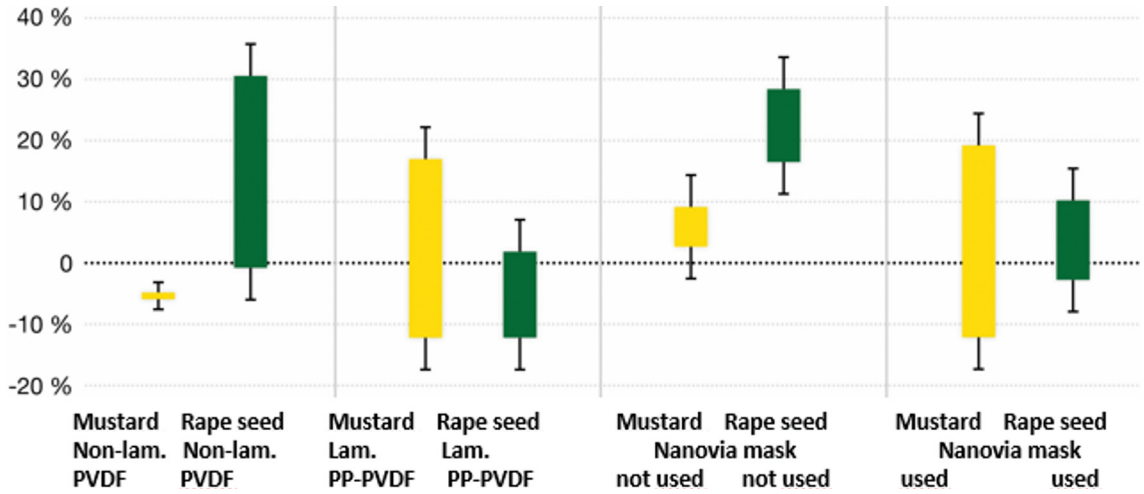

Fig. 15. Chart comparison of inhibition of mustard and rapeseed root growth in % (seeds off sample).

other hand, root growth was stimulated both in seeds in direct contact with the fabric and in seeds placed outside the fabric, e.g., in the non-worn Nanovia Mask veil, the *I* value was set at –131 %.
Obtained results of root growth inhibition correspond with studies focused on the effect of nano- and microplastics performed with terrestrial plants. An increase in total root length and a decrease in root average diameter have been reported in spring onion (*Allium fistulosum*) after exposure to microplasts (de Souza Machado et al., 2019). Bosker et al. state that the change in cress (*Lepidium sativum*) root growth depends on the exposure time and the size of the plastic particles. After 24 h exposure, a decrease in root growth when exposed to 50 nm particles and an increase when exposed 500 nm particles was observed. However, no significant difference in root growth was observed after 48 or 72 h of exposure (Bosker et al., 2019). In addition to root elongation, the presence of nano- and microplastics also affects the germination process itself. Delayed germination of *L. sativum* was observed upon exposure to various doses of plastic particles (Bosker et al., 2019; Pflugmacher et al., 2020). Blocking of pores 'in seed capsules' by particles is considered to be one of the possible mechanisms causing this delay (Bosker et al., 2019).

Conclusion

One of the consequences of the COVID-19 pandemic is an unprecedented increase in the production of respiratory protective devices which include nanotextiles. Because these protective devices are made of fibers and nanofibers of various plastics, they contribute to the increased occurrence of nano- and microplastics in the environment (Sullivan et al., 2021). Based on measurements performed both in the production of material for nanofiber masks and nanofiber respirators and in the production of our own protective equipment, we have shown that if the production line (or its corresponding part) is separated from the rest of the working environment and the air discharged from this separate space is HEPA filtered, the filters capture the nano- and microplastic particles formed. Thus, a greater danger to the environment actually arises from the use of protective equipment, and especially its mechanical stress (abrasion). A tensile test was used to demonstrate that the resistance of the input material for protective equipment production depends on the arrangement of the polymer chains in the production of nonwovens. This finding leads to the assumption that durability as well as effectiveness of protective equipment also depends on the method of processing the sandwich nanotextile used in their production. Based on the performed tests, it can be assumed that the filter layer in extruded nanofiber respirators is not homogeneous.
Due to the COVID-19 pandemic, the use of nanofiber respirators and nanofiber masks has become common not only in workplaces with high risk of infection transmission, but also in general public. While in hazardous workplaces (e.g., medical facilities), adequate disposal of discarded protective equipment is ensured, the method of discarding and liquidation of protective equipment used by the public depends on the information and discipline of its members. The fate of discarded protective equipment in the environment depends on many variables (temperature, humidity, pH, etc.) as well as on the intensity of their mechanical stress. The performed tests of semichronic toxicity on the seeds of selected plants confirmed the influence of the material from the protective agents on the root growth. Direct contact of the fabric with mustard and rapeseed seeds showed more than 50 % inhibition of root growth. In case of fescue seeds, on the other hand, its growth was stimulated.

Acknowledgements
The authors thank Ing. Bohdan Filipi, Ph.D. of the Faculty of Safety Engineering of VSB-TU Ostrava for spectrum measurements and David Chadima of Prusa Research a.s. for assistance with performing the tensile tests. The publication was written within the student grant competition "Release of Nano and Microplastics from Nanotextiles and Determination of Their Effect on the Environment" – project number SP2021/69.

References

Barboza LGA, Vieira LR, Branco V, Figueiredo N, Carvalho F, Carvalho C, Guilhermino L (2018) Microplastics cause neurotoxicity, oxidative damage and energy-related changes and interact with the bioaccumulation of mercury in the European seabass, Dicentrarchus labrax (Linnaeus, 1758). Aquatic Toxicology, 195, 49–57.

Barboza LGA, Lopes C, Oliveira P, Bessa F, Otero V, Henriques B, ... Guilhermino L (2019) Microplastic in wild fish from North East Atlantic Ocean and its potential for causing neurotoxic effects, lipid oxidative damage, and human health risks associated with ingestion exposure. Science of The Total Environment, 134625. doi: 10.1016/j.scitotenv.2019.134625.

Barnes DK, Galgani F, Thompson RC, Barlaz M (2009) Accumulation and fragmentation of plastic debris in global environments. Philosophical Transactions: Biological Sciences, 364, 1985–1998.

Bosker T, Bouwman LJ, Brun NR, Behrens P, Vijver MG (2019) Microplastics accumulate on pores in seed capsule and delay germination and root growth of the terrestrial vascular plant Lepidium

sativum. Chemosphere. 226, 774—781. doi: 10.1016/j.chemosphere.2019.03.163.

Brennecke D, Duarte B, Paiva F, Caçador I, Canning-Clode J (2016) Microplastics as vector for heavy metal contamination from the marine environment. Estuarine, Coastal and Shelf Science, 178, 189—195.

Brewer A, Dror I, Berkowitz B (2021) The Mobility of Plastic Nanoparticles in Aqueous and Soil Environments: A Critical Review. ACS ES&T Water, 1(1), 48—57. doi: 10.1021/acsestwater.0c00130.

Enfrin M, Lee J, Gibert Y, Basheer F, Kong L, Dumée LF (2019) Release of hazardous nanoplastic contaminants due to microplastics fragmentation under shear stress forces. Journal of Hazardous Materials, 384. doi: 10.1016/j.jhazmat.2019.121393.

Gerritse J, Leslie HA, de Tender CA, Devriese LI, Vethaak AD (2020) Fragmentation of plastic objects in a laboratory seawater microcosm. Scientific Repports, 10 (1). doi: 10.1038/s41598-020-67927-1.

Guo X, Wang J (2019) Sorption of antibiotics onto aged microplastics in freshwater and seawater. Marine Pollution Bulletin, 149, 110511. doi:10.1016/j.marpolbul.2019.1105.

Jacob H, Besson M, Swarzenski PW, Lecchini D, Metian M (2020) Effects of Virgin Micro- and Nanoplastics on Fish: Trends, Meta-Analysis, and Perspectives. Environmental Science & Technology, 54(8), 4733—4745. doi: 10.1021/acs.est.9b05995.

Kögel T, Bjorøy Ø, Toto B, BIenfait AM, Sanden M (2019) Micro- and nanoplastic toxicity on aquatic life: Determining factors. Science of Total Environment, 709. doi: 10.1016/j.scitotenv.2019.136050.

Lee K-W, Shim WJ, Kwon OY, Kang J-H (2013) Size-Dependent Effects of Micro Polystyrene Particles in the Marine Copepod Tigriopus japonicus. Environmental Science & Technology, 47(19), 11278—11283. doi: 10.1021/es401932b.

Maity S, Pramanick K (2020) Perspectives and challenges of micro/nanoplastics-induced toxicity with special reference to phytotoxicity. Global Change Biology, 26(6), 3241—3250. doi: 10.1111/gcb.15074.

Nizzetto L, Futter M, Langaas S (2016) Are Agricultural Soils Dumps for Microplastics of Urban Origin? Environmental Science & Technology, 50(20), 10777—10779. doi: 10.1021/acs.est.6b04140.

Novotna K, Cermakova L, Pivokonska L, Cajthaml T, Pivokonsky M (2019) Microplastics in drinking water treatment — Current knowledge and research needs. Science of The Total Environment, doi: 10.1016/j.scitotenv.2019.02.431.

OECD (2006) Test No. 208: Terrestrial Plant Test: Seedling Emergence and Seedling Growth Test. OECD Publishing, Paris.

Pirsaheb M, Hossini H, Makhdoumi P (2020) Review of microplastic occurrence and toxicological effects in marine environment: Experimental evidence of inflammation. Process Safety and Environmental Protection, doi: 10.1016/j.psep.2020.05.050.

Pivokonský M, Pivokonská L, Novotná K, Čermáková L, Klimtová M (2020) Occurrence and fate of microplastics at two different drinking water treatment plants within a river catchment. Science of The Total Environment, 140236. doi: 10.1016/j.scitotenv.2020.140236.

Pflugmacher S, Sulek A, Mader H, Heo J, Noh JH, Penttinen OP, Kim Y, Kim S, Esterhuizen M (2020) The Influence of New and Artificial Aged Microplastic and Leachates on the Germination of Lepidium sativum L. Plants, 9 (3). doi: 10.3390/plants9030339.

de Souza Machado AA, Lau ChW, Kloas W, Bergmann J, Bachelier JB, Faltin E, Becker R, Görlich AS, Rillig MC (2019) Microplastics Can Change Soil Properties and Affect Plant Performance, Environ. Sci. Technol. 53 (10), 6044—6052. doi: 10.1021/acs.est.9b01339.

Sullivan GL, Delgado-Gallardo J, Watson TM, Sarp S (2021) An investigation into the leaching of micro and nano particles and chemical pollutants from disposable face masks — linked to the COVID-19 pandemic. Water Research, 196. doi: 10.1016/j.watres.2021.117033.

Wahl A, Le Juge C, Davranche M, El Hadri H, Grassl B, Reynaud S, Gigault J (2021) Nanoplastic occurrence in a soil amended with plastic debris. Chemosphere, 262. doi: 10.1016/j.chemosphere.2020.127784.

Waymana C, Niemann H (2021) The fate of plastic in the ocean environment — a minireview. Environmental Science: Processes Impacts, 23(2), 198—212. doi: 10.1039/d0em00446d.